THE DEVELOPMENT OF ENERGY EFFICIENT WASTEWATER TREATMENT: ELECTROCHEMICAL OXIDATION AND PFACs LIQUID-LIQUID EXTRACTION

A Dissertation
Presented to
The Academic Faculty

by

Kaihang Zhang

In Partial Fulfillment
of the Requirements for the Degree
Doctor of Philosophy in the
School of Civil and Environmental Engineering

Georgia Institute of Technology
December 2022

THE DEVELOPMENT OF ENERGY EFFICIENT WASTEWATER TREATMENT: ELECTROCHEMICAL OXIDATION AND PFACs LIQUID-LIQUID EXTRACTION

Approved by:

Dr. John C Crittenden, Advisor
School of Civil and Environmental
Georgia Institute of Technology

Dr. Nian Liu
School of Chemical & Biomolecular
Engineering
Georgia Institute of Technology

Dr. Yongsheng Chen
School of Civil and Environmental
Georgia Institute of Technology

Dr. Xing Xie
School of Civil and Environmental
Georgia Institute of Technology

Dr. Ching-Hua Huang
School of Civil and Environmental
Georgia Institute of Technology

Date Approved: [August 17, 2022]

To my family, friends, and mentors

ACKNOWLEDGEMENTS

TBALE OF CONTENTS

LIST OF TABLES

LIST OF FIGURES

LIST OF SYMBOLS AND ABBREVIATIONS

AOP	Advanced oxidation process
BA	Benzoic acid
BDD	Boron doped diamond
CMOS	Complementary Metal Oxide Semiconductor
COD	Chemical oxygen demand
COSMO-RS	Conductor like Screening Model for Real Solvents
CTAB	Cetyltrimethylammonium ammonium bromide
DC	Direct current
DCBR	Differential column batch reactor
DFT	Density functional theory
DSAs	Dimensionally Stable Anodes
EAOPs	Electrochemical advanced oxidation processes
EDL	The electrical double layer
EE/O	Electrical energy requirement for one order magnitude degradation
EG	Ethylene glycol
EIS	Electrochemical Impedance Spectroscopy
FTIR	Fourier transform infrared spectroscopy
HPLC	high-performance liquid chromatography
Ils	Ionic liquids
LLE	Liquid-liquid extraction
LSV	Linear sweep voltammetry
MD	Molecular dynamics

NHE	Normal hydrogen electrode
NTAs	Nanotube arrays
OEP	oxygen evolution potential
PBE	Perdew-Burke-Ernzerhof
PEM	Proton exchange membrane
PFAS	Per-and polyfluoroalkyl substances
PFOA	Perfluorooctanoic acid
PFOS	Perfluorooctanesulfonic acid
PWM	Pulse-width modulation
REM	Reactive ceramic membrane
SCE	Standard calomel electrode
SEM	Scanning electron microscope
TTL	Transistor-Transistor Logic
VASP	Viação Aérea São Paulo S/A
XANES	X-ray absorption near-edge structure spectra
XPS	X-ray Photoelectron Spectroscopy

SUMMARY

Degradation of refractory pollutants and reduction of degradation costs are two essential directions in wastewater treatment. EAOPs is a technology that has been developed in recent years and can meet these two requirements well under most conditions. EAOPs generate hydroxyl radicals (HO·) at the anode that oxidize almost all organic contaminants to CO_2 and H_2O, and they also produce H^+ and electrons (from the organics in the WW) that migrate to the cathode. Electrochemical oxidation is regarded as extremely effective for chemical oxygen demand (COD) reduction, particularly for removing emerging pollutants resistant to traditional oxidation processes. For example, in recent years, perfluorinated chemicals have become a major environmental issue. The development of highly efficient and green PFAS wastewater treatment technology is necessary. Electrochemical degradation may destroy PFACs well if the proper anode material is developed.

Fluorinated compounds are widely applied in the semiconductor, polymer, and energy industries. Among them, polyfluoroalkyl Substances (PFAS) and their salts have been the primary concerns because they bioaccumulated in the food chain and are exceptionally resistant to typical degradation processes. The traditional activated sludge process is not effective enough in removing PFACs. The hole on the anode's surface and the hydroxyl radical produced by the anode are universal to all organic compounds; hence, they cannot selectively remove PFACSs. Therefore, liquid-liquid extraction of PFOA is studied by using ionic liquid (IL) and octanol as extractants.

The development of EAOPs focuses on advancing the understanding of the electrochemical oxidation systems and developing EAOPs as a more commercially applicable technology. The efforts include: First, developing a novel electrochemical system that can significantly lower the energy consumption by collecting the cathode hydrogen energy; second, investigating multiple layer flow through anode for the enhanced mass transfer process to increase the overall oxidation efficiency; and third, develop novel anode materials that consider both the oxygen evolution potential and high conductivity with high radical generation rate; To be specific, a novel EAOP-fuel cell energy recovery system is developed with the integration of anode chamber and cathode hydrogen separation chamber with proton exchange membranes. The mass transfer impact is quantitatively investigated regarding the hydrodynamic parameters. A mathematical model associated with electrochemical oxidation kinetics and mass transfer impact is established and validated with experimental data. Novel inactive flow through anode materials is fabricated. These anodes include porous TiO_2 NTAs with Mn_2O_3 anode. TiO_2-based SnO_2-Sb and Ti_4O_7 wire mesh anode.

The development of liquid-liquid extraction (LLE) of PFACs focuses on advancing the understanding of the LLE mechanisms and discovering the extractant for high PFOA and PFOS extraction efficiency. The efforts include: First, understanding the effect of standard variables on extraction efficiency: extraction time, pH, temperature, etc, and second, screening the ionic liquids (ILs) for PFACs extraction. To be specific, Quaternary ammonium surfactant hexadecyl trimethyl ammonium bromide (CTAB) shows the effect of PFOA extraction. Therefore, ILs containing the quaternary ammonium function group are studied for improved PFOA extraction efficiency. The extraction mechanism is

proposed based on the experiment results. It is also proved by MD (molecular dynamic) and density functional theory (DFT); 1763 ILs for PFACs extraction from water were systematically screened using the COSMOtherm to estimate the infinite dilution activity coefficient ($\ln\gamma^\infty$) of PFOA and PFOS in water and ILs.

CHAPTER 1. INTRODUCTION

The increase of water contamination by organic compounds resulting from numerous industrial, agricultural, and urban human activities is one of the most significant global issues at present. The large majority of these chemicals are persistent organic pollutants due to their resistance to standard treatments such as coagulation, biological oxidation, adsorption, ion exchange, and chemical oxidation. As a result, they have been discovered in rivers, lakes, seas, and even drinking water around the globe. This poses a significant environmental health risk because of their toxicity and possible hazardous health consequences on living creatures, including humans.[1-3]

In the past 70 years, biological Wastewater Treatment has been the mainstream of Industrial Wastewater Treatment. In the Oil Refining and petrochemical industry, a wide variety of hydrocarbon species and large quantities of free Oil significantly increase the organics loading. Due to a large number of resistant and inhibitory molecules present in the wastewater influent of these two industries, many consider that these two industrial wastewaters are the most challenging to treat in terms of dependable and constant biological treatment efficiency. Consequently, particularly in these two industries, Activated Sludge is the configuration of choice for Biological Treatment due to its adaptability for process management and capacity to implement more precise Bioreactor control in the face of influent concentration variability. During the past five years, a number of AOP technologies have been pilot-tested for refinery and petrochemical wastewater applications at the central WWTP and for Upstream Pretreatment, the majority of which featured Ozone as an AOP design

component. The expense of ozone was expensive because of the high temperature of these wastewater streams, which rendered the majority of these initiatives unsuccessful. Few successes were reported in streams that had either applied a cooling mechanism or allowed some time to pass prior to treatment, allowing ambient cooling to occur. In these applications, Fenton's Reagent has generated outstanding pollutant reduction results, but its Operating Cost (OPEX) has been unacceptably high compared to biological treatment.

EAOPs are new and environmental-friendly techniques that can oxidize toxic organic compounds by producing Hydroxyl radical (HO•). Hydroxyl radical is a very potent electrophile capable of oxidizing most electron-rich organic compounds into water, carbon dioxide, and mineral acids. The benefits of EAOPs are: 1) they can generate sufficient HO• concentration that effectively oxidizes organic compounds, 2) they have reasonably high energy efficiency, and 3) they do not need any additional chemicals. Common AOPs include O_3/H_2O_2, UV/H_2O_2, UV/TiO_2, Fenton, and photo-Fenton.[4, 5] However, most rely on adding chemical oxidants or UV light to activate them. This increases the cost dramatically and can consume large amounts of energy transfer. Compared to the above two methods, EAOPs have a few advantages, including 1. Low OPEX. The main OPEX expense for EAOPs is power. 2. Low maintenance cost. EAOP just necessitates the occasional cleaning of electrodes. 3. a small reservoir. EAOP has a substantially shorter hydraulic retention time (HRT) than biological treatment for practically complete oxidation of pollutants (and oxidizes high COD wastewaters). 4. High dependability. EAOP is extremely user-friendly since it contains just three process variables, which makes process control considerably simpler and results in significantly less downtime. 5. Excellent controllability the

2

stoichiometric connection between power consumption and pollutant removal in EAOP is almost linear. 6. Temperature tolerance. EAOP has a significantly wider temperature tolerance range. It can treat wastewaters up to 200 degrees Fahrenheit. 7. No residuals. EAOP treatment produces just effluent water, and there are no disposal or residual treatment needs.

The thesis's primary focus is on the improve the overall energy efficiency of the EAOPs system. Although the production of radicals and the high oxygen evolution potential is a fundamental aspect of EAOPs, the operation voltage of EAOPs is also essential considering the energy consumption to drive the same current density. Secondly, the mass transfer process is also crucial during the process of organic destruction. Therefore, flow through anode is fabricated and studied. However, given the pressure drop based on the flow rate, the cost of the anode fabrication, the effective surface area given the touristy of the anode, and the maintenance of the anode, multiple layer wire mesh anode is proposed for highly efficient mass transfer for industrial application. To be noticed, the cathode side is rarely discussed in the EAOP process. The proposed EAOP-fuel cell system is the work to fill in the blank of the cathode area.

Though EAOPs have excellent potential in the wastewater field. Its universal oxidation capability may lead to a low oxidation efficiency for specific compounds. Polyfluoroalkyl Substances (PFAS) and their salts have been the primary concern due to their bioaccumulation and resistance to normal degradation. It is challenging to break down PFOA since the carbon-fluorine bond energy (116 kcal/mol) is the strongest single bond in organic chemistry.[6] Due to the oleophobic nature of PFACs, the (K_{ow}) of PFOS was determined to be -0.18 (log (56 mg/L in n-octanol / 680 mg/L in water), which implies we will have a low

extraction efficiency for PFOA. Therefore, the extractant is required in the organic phase for liquid-liquid extraction. Ionic liquids (ILs) are used in our study. It is green solvents composed of organic cations and organic or inorganic anions [7-9]. The countless combinations of those cations and anions allow engineering of the ILs properties for LLE purposes [10].

In this dissertation, three levels have been studied for EAOPs, from large to small. 1) System level: energy recovery system and electric power mode; 2) Reactor level: flow-through wire mesh anode 3) Electrode level: electrode material modification. Besides, the degradation efficiency was also verified for persistent pollutants PFACs. For the difficult degradation of PFACs and the high energy consumption, we performed liquid-liquid extraction methods to remove the PFACs from water. To be specific, the contents are introduced as follows. Chapter 2 proposes a novel EAOP-fuel cell energy recovery system, and the system performance in varied conditions is summarized. Four widely known EAOP anodes are studied with the system for practical purposes. In Chapter 3, flow through multiple layer wire mesh anode is used in the novel EAOP-fuel cell energy recovery system. The PFOA as a persistent pollutant is oxidized by the Ti_4O_7 wire mesh anode and TiO_2 NTAs/SnO_2-Sb_2O_3 electrode. This study offers some important insights into improving the mass transfer by the design of electrode configuration. In Chapter 4, a novel anode material Mn_2O_3-TiO_2 NTAs is developed. The anode is tested by both electrochemical oxidation experiments and advanced characterization methods. In Chapter 5, pulse potential EAOPs are studied for optimal power efficiency. The work shows that in pulse potential mode, the off-voltage needs to be controlled for improved performance, which is rarely discussed in

previous research. Chapter 6 shows the availability of liquid-liquid extraction methods for

PFOA removal from the aqueous phase. Chapter 7 uses the COSMO-RS to screen ILs for

PFOA and PFOS extraction. Chapter 8 summarizes findings in the dissertation and

recommends future research direction

CHAPTER 2. EAOP-FUEL CELL ENERGY RECOVERY SYSTEM FOR HIGHLY EFFICIENT WASTEWATER TREATMENT

2.1 Abstract

Electrochemical oxidation uses anodic oxidation to create the hydroxyl radical for organic removal. The counterpart cathode generates hydrogen gas. For most EAOPs reactors, either it is an open vessel, or the hydrogen and oxygen are not separated, which does support the hydrogen collection. Our EAOP-fuel cell energy recovery system consists of the PEM reactor with a separate anode and cathode chamber, and the cathode chamber is connected to the hydrogen fuel cell. The hydrogen fuel cell could run in both the hydrogen-air and hydrogen-oxygen mode. To verify the system's availability under different conditions, oxidation efficiency and system energy recovery ratio were calculated for different electrode materials, salt concentrations, organic centration, etc. Four representative anodes include BDD, Ti/SnO$_2$-Sb, PbO$_2$, and TiO$_2$ NTAs/ SnO$_2$-Sb tested at 3, 4, and 5 V to find the optimal system operating condition. Compared with the theoretical energy recovery ratio of 35% in the hydrogen-oxygen mode of the EAOP-fuel cell energy recovery system, our experiments show 22% energy saving in the hydrogen-oxygen mode at 3 V with BDD as an anode. These results show that our system can significantly reduce the energy consumption of the EAOP system in future use.

2.2 Introduction

In the electrochemical advanced oxidation process (EAOPs), the hydroxyl radicals (HO·) are generated to oxidize organic contaminants to CO_2 and H_2O.[2] Based on Equation

25, the redox potential of hydroxyl radical is 2.8 V vs. NHE, which is a strong oxidant for organic oxidation.

$$OH^\cdot + e^- + H^+ = H_2O \quad 2.73 \; vs \; NHE \tag{1}$$
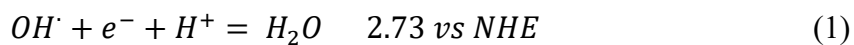
EAOP requires a high overpotential of oxygen to generate hydroxyl radicals. In cathode, hydrogen as a clean and sustainable fuel is produced based on the redox potential, but it is rarely discussed in the application of EAOPs. The role of fuel cells has long been underestimated in the EAOP field for three main reasons: i) The difficulty in designing reactors for hydrogen collection, and ii) The energy recovery ratio of fuel cells is not properly perceived. iii) some other cathode reduction processes: like oxygen to peroxide, the hydrated electron is compatible with the EAOPs. H-cell with separate anode and cathode chambers is widely used to collect hydrogen. However, the distance between the positive and negative electrodes is large, and the operating efficiency is low given the high electrolyte resistance. Besides, the electrolyte is needed in the cathode chamber. In long-term operation, the high pH base solution in the cathode chamber must be neutralized by the acid solution. In our study, the EAOP reactor (Figure 1) consists of two half cells separated by the PEM membrane, which can keep high electric conductivity for the electrolysis and successfully separates and collects the hydrogen gas. The reactor allows water to pass through the anode cells. Hydrogen gas is produced by the proton crossing the membrane on the cathode side. The gas diffusion layer (GDL) on each side helps in efficient current distribution and prevents the water and gas from being transported through the PEM membrane. In terms of the energy recovery ratio, it is largely controlled by

Outlet + O₂ "Outlet + O$_2$", "inlet", "H$_2$"

1 2 3 4 5 6 5 4 7 2 1
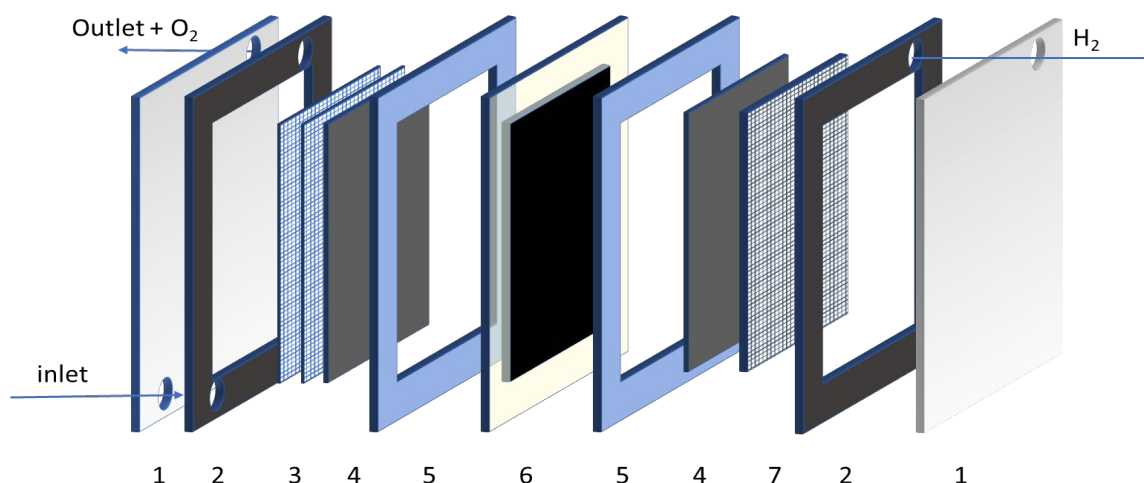
Figure 1 – The sketch of the EAOP reactor for hydrogen seperation 1. Outer protective case 2. Waterproof gasket 3. flow through or flow-by anode 4. Gas diffusion layer (GDL) 5. Plastic frame 6. PEM membrane 7. hydrogen generation cathode (stainless steel)

the operation voltage of the EAOPs system. The value of energy that can be recovered ideally at 5V is only 8%. But in 3V, ideally, we can recover about 35% of the energy, which will be very substantial. The detailed calculation is talked about later. Converting the oxygen to active species (Oxygen reduction process) is also one solution to improve the EAOP's efficiency. The possible cathode reduction reaction (Table 1) is listed below. So far, the hydrated electron is recognized as the strongest reductant, which half redox potential around 2.3 V vs. NHE. [11] The detection of the hydrated electron is reported in the (Advanced oxidation process) AOP process, and also the photoemission from the solids.[12, 13] But its selectivity and production efficiency are still limited, and its application in wastewater treatment is still in the early stage. Based on the standard redox potential in table 1, oxygen reduction is one promising direction. [14, 15]. the oxygen reduction to hydrogen peroxide is 0.695 V, but it is a two-electron transfer step; catalytic is required for a fast reaction. For wastewater treatment applications, the mass transfer of the oxygen to the cathode surface is a limiting process. In comparison, hydrogen

gas generation is the easiest and most controllable reaction. The cost of the cathode of hydrogen generation is much cheaper and has a much longer service life without worry about the position of the catalyst.

Table 1 – The standard redox potentials for the cathodic reaction [16]

$O_2 + 2H^+ + 2e^- \rightarrow H_2O_2$	$E_0 = 0.695\ V\ vs\ NHE$
$H_2O_2 + e^- + H^+ \rightarrow H_2O + OH\cdot$	$E_0 = 0.395\ V\ vs\ NHE$
$e^- + H^+ \rightarrow \frac{1}{2}H_2$	$E_0 = 0\ V\ vs\ NHE$
$H_2O + e^- \rightarrow e_{aq}^-$	$E_0 = -2.3\ V\ vs\ NHE$

This study proposes and tests the EAOP-fuel cell energy recovery system for improving energy efficiency. Four electrodes widely used in the EAOP field are tested for the system. Previously proposed electrode designs emphasized boosting the rate of hydroxyl radical generation. This often necessitates the use of electrodes with wider bandgaps. The wide bandgap semiconductor gets higher oxygen evolution potential (OER), reducing conductivity.

2.3   Experiment

2.3.1   Electrode and chemicals

BDD and PbO_2 electrode is purchased from Hunan Xinfeng Technology Co. Ltd. The $Ti/SnO_2/Sb_2O_3$ (DSA) is purchased from the Chentai electrode Co. Ltd. The TiO_2 NTA with SnO_2/Sb_2O_3 are fabricated based on the previously published paper.[17]

The titanium mesh (100 mesh) was purchased from Northwest Institute for Non-ferrous Metals Research (Xi'an, China). Benzoic acid (BA, 95%) was purchased from Aladdin Biochemical Co., Ltd. (Shanghai, China). Ethylene glycol (EG), manganese (III) acetylacetonate, isopropyl alcohol, and ammonium fluoride (NH_4F) were obtained from Macklin Biochemical Co., Ltd. (Shanghai, China). All solutions were prepared with deionized water (Milli Q purification system, 18.2 MΩ cm).

2.3.3 *Electrochemical measurements*

The Linear sweep voltammetry (LSV) was carried out on the CH I 660D electrochemical workstation using a standard three-electrode configuration with a saturated calomel electrode (SCE) as the reference electrode and platinum sheet as the counter electrode. The anodic scan rate of the electrode was 10 mv/s. Electrochemical Impedance Spectroscopy （EIS） was carried out on an electrochemical workstation (PARSTAT 3000A-DX). The frequency range is 10 kHz to 1 Hz with 10 mV amplitude voltage at open circuit potential.

2.3.4 *Experimental system*

The EAOP-fuel cell energy recovery system is shown in Figure 2. The reservoir and EAOP reactor are composed of a DCBR (Differential column batch reactor) system. The produced H_2 is supplied to the anode of the fuel cell. Air or pure oxygen is supplied to the cathode chamber, and the deionized water will flow from the lower end. In the future, we will
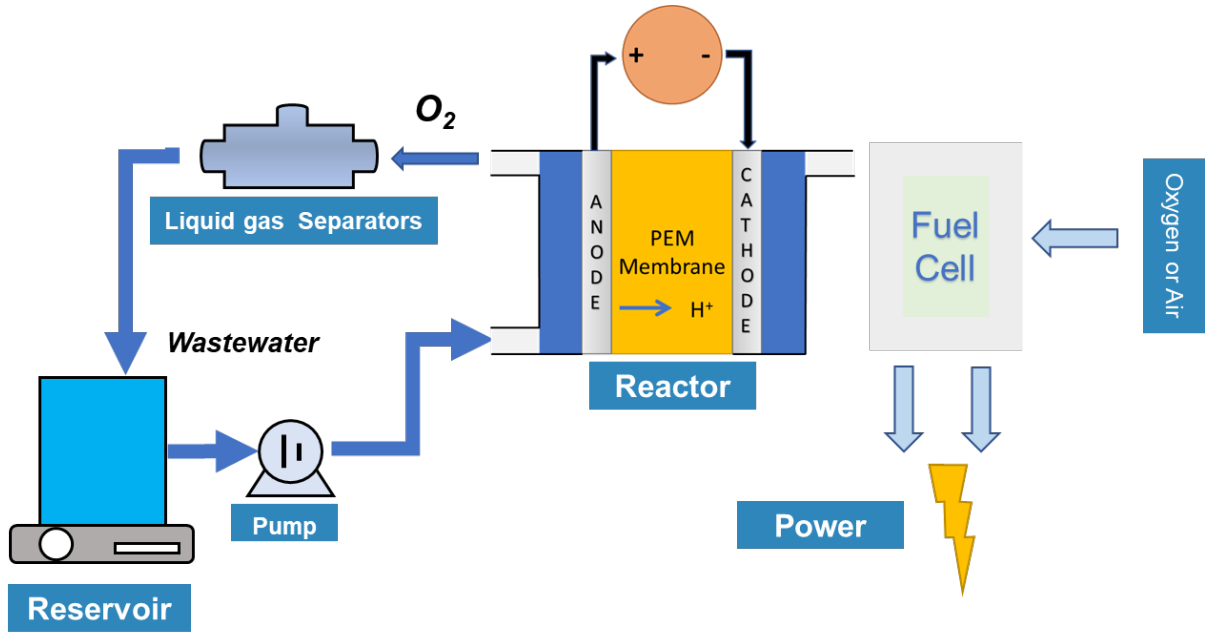
Figure 2 – The sketch of the EAOP - fuel cell energy recovery system

try to recover oxygen from water to reduce the dependence on pure oxygen and improve the efficiency of fuel cells with air input.

2.3.5   *Energy recovery ratio calculation*

The energy efficiency of the EAOPs is calculated by electrical efficiency per log order reduction (EE/O) based on Equation 2. The energy recovery ratio (η_{sys}) of the EAOP-fuel cell system (Equation 3) is governed by the efficiency of the cathodic hydrogen production process by the EAOP reactor and the electric power generation efficiency of hydrogen fuel cells. This two-step energy conversion process begins with DC power driving the EAOP reactor to generate hydrogen, which is then transformed into electricity by the fuel cell. The primary chemical equation of the process, Gibbs equation, and thermodynamic data are listed as Equations 4, 5, and Table 2. [18]. 1.23 V is the reversible cell voltage for decomposing one molar of water into hydrogen and oxygen for the hydrogen production step. [19] Therefore,

11

η_{H2} is reversible cell voltage divided by the real cell potential (Equation 6). For hydrogen fuel cells, the useful energy output is the electrical energy produced, and the energy input is the enthalpy of hydrogen, as shown in Figure 3.[20] Therefore, the energy efficiency of the fuel cell is calculated as Equation 7. Assuming that all the Gibbs free energy can be converted into electrical energy (the reaction is reversible), the maximum theoretical efficiency of a fuel cell is 83%.

$$EE/O = \frac{U \cdot I \cdot t}{V \cdot log(\frac{C_o}{C_i})} \tag{2}$$

$$\eta_{sys} = \eta_{H2} \cdot \eta_{fuel} \tag{3}$$

$$H_2(g) + \frac{1}{2}O_2(g) \rightarrow H_2O(l) \tag{4}$$
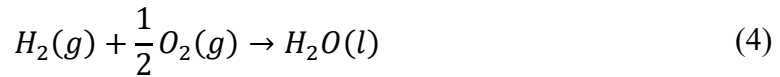
$$\underbrace{\Delta G}_{elec.} = nFE = \Delta H - \underbrace{T\Delta S}_{heat} \tag{5}$$

U is the voltage (V), I is the applied current (mA), t is the electrolysis time (h), and V is the volume (cm^3). EE/O denotes the energy required for 90% compound oxidation, and if you double or triple the power of BA destruction will be 99% and 99.9%, respectively.

Table 2 – Thermodynamic properties of water electrolysis in 298 K.

Quantity	H$_2$O	H$_2$	0.5 O$_2$	Change
Enthalpy	-285.83 kJ	0	0	ΔH = 285.83 kJ
Entropy	69.91 J/K	130.68 J/K	0.5 x 205.14 J/K	$T\Delta S$ = 48.7 kJ

$$\eta_{H2} = \frac{1.23 \ V}{U_{cell}} \tag{6}$$

$$\eta_{max} = \frac{\Delta G}{\Delta H} = 83\% \tag{7}$$

By substituting Equations 6 and 7 into Equation 3, the system's energy efficiency is determined as Equation 8. As a result, for the maximum energy recovery efficiency of an EAOP-fuel cell system, the operating voltage should be as low as feasible.

ΔH → □ → ΔG

Q = TΔS   ΔG < ΔH
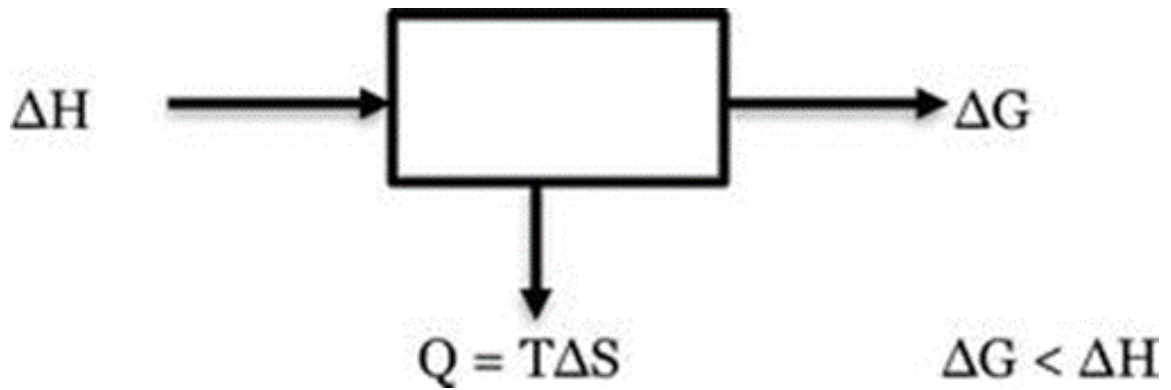
Figure 3 – Energy inputs and outputs for a fuel cell as an energy conversion device

$$\eta_{sys} = \frac{1.253 \ V}{U_{cell}} \cdot 83\% \tag{8}$$

2.4   Results and discussion

2.4.1   *The Introduction of four electrodes and their electrochemical property*

We tested four commonly studied electrodes for EAOPs. They are PbO_2, TiO_2 NTAs/SnO_2-Sb_2O_3, and Ti/SnO_2-Sb. These electrodes exhibit significantly different OER (oxygen evolution potential) in linear sweep voltammograms (LSV) (Figure 4). The onset potential of PbO_2, Ti/SnO_2-Sb, BDD, and TiO_2 NTAs/SnO_2-Sb_2O_3 are 1.5 V, 1.8 V, 2.2 V, and 3.1 V, respectively. Above the onset potential, the anodic current rises steeply due to O_2 evolution. Therefore, the higher the overpotential, the higher the hydroxyl radical generation efficiency of the electrode. The oxidation rate is controlled by both mass transfer and hydroxyl radical generation rate of the anode. In theory, 2.8 V is required for hydroxyl radical generation. However, considering extra voltage consumption, including anodic activation energy loss, ohmic loss of electrolyte, and cathodic activation energy loss, for the EAOP-fuel cell system, 3V is applied as the lowest operation voltage.
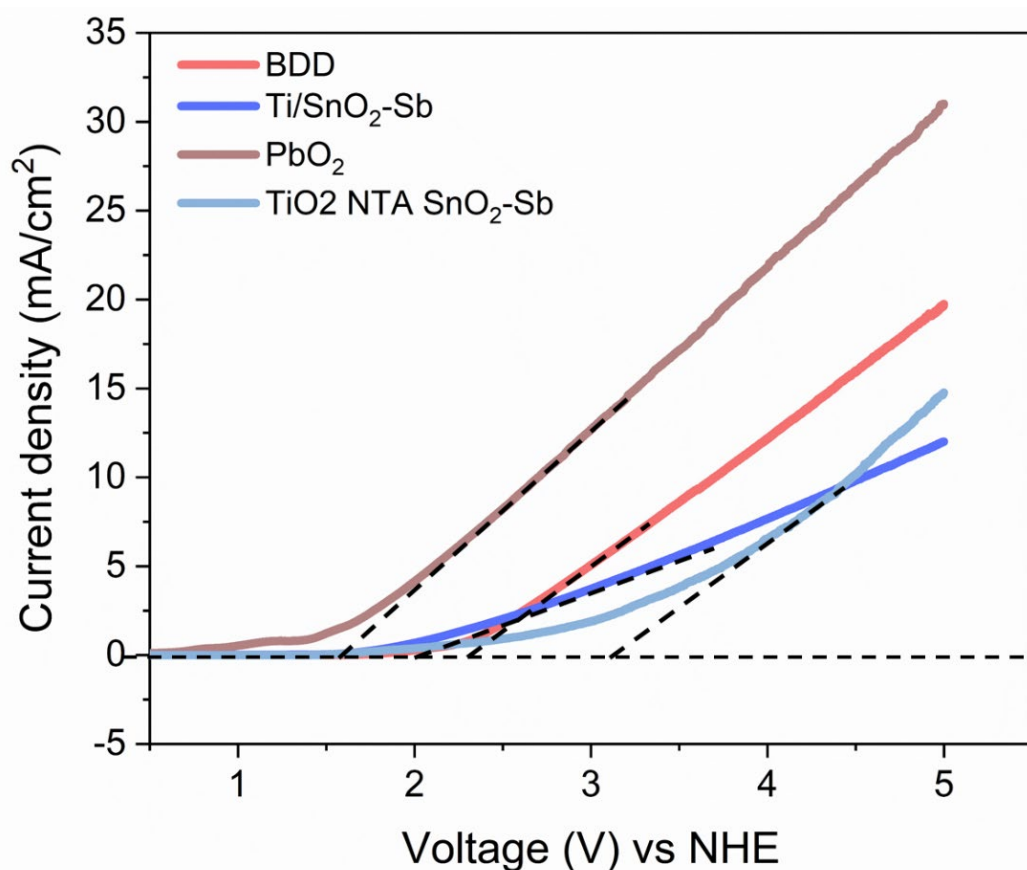
Figure 4 – The liner scan voltage (LSV) of the BDD, Ti/SnO2-Sb, PbO$_2$ and TiO$_2$ NTA SnO$_2$-Sb with 1 cm electrode spacing in 0.1 M Na₂SO₄. Cathode: Pt Reference Electrode； Ag/AgCl/ Ag/AgCl/saturated KCl

<u>2.4.1.1 Boron doped diamond (BDD)</u>

BDD is the most promising and widely studied electrode EAOPs for its extreme stability and high hydroxyl radical generation rate.[2] It has a wide bandgap (Eg = 5.5 eV), so its anodic oxidation potential is high, and due to its behavior as a non-active electrode, it promises high quantities of hydroxyl radicals on its surface. [21] The stability of the BDD anode is contributed to the C atoms being in sp3 hybridization. [22] The diamond is an insulator transferred to a semiconductor by adding the boron as a dopant with an activation energy of around 0.37 eV. The boron atoms substitute for carbon atoms in the diamond lattice, giving a

15

p-type semiconductor, where the dopant consumes an extra electron for chemical bonding, thus creating excess holes in the semiconductor.[23] It is worth mentioning that the level of boron doping, morphology, crystallographic orientation, surface termination, and sp^2 carbon impurities modify the electrochemical response and corrosion resistance of BDD electrodes.[24]

2.4.1.2 Lead Oxide (PbO$_2$)

PbO_2 electrode is famous for its low price and facility to obtain. The leakage of Pb^{2+} is one of the main concerns of the lead oxide electrodes.[25] The preparation of a stable lead dioxide layer by electrodeposition on an inert substrate has mitigated this drawback; Since then, lead dioxide anodes have been widely applied in wastewater treatment[26]. Though PbO_2 shows good electrocatalytic activity to produce the hydroxyl radical, the narrow bandgap of the lead oxide (Eg = 1 eV) affects its radical generation efficiency compared with BDD and Ti/SnO_2 electrodes. [27, 28]

2.4.1.3 Ti/SnO$_2$-Sb (ATO)

Antimony-doped tin oxide (ATO) coated on titanium is one of the most intensively studied Dimensionally Stable Anodes (DSAs) for wastewater treatment. [29] This anode material is an inactive DSA-type of electrode material, so the oxygen evolution reaction can be suppressed to allow the degradation of organic compounds by hydroxyl radicals. ATO is more efficient in the oxidation of organics than other DSAs with noble metals. Compared with traditional DSAs, such as RuO_2 (bandgap = 1.2 V) and IrO_2 (metal), the SnO2's bandgap around 3.6 eV, which promises a higher oxygen overpotential reduces the energy consumption

caused by oxygen evolution and also favors a greater current efficiency.[30-32] During the process of electrocatalysis, a large number of hydroxyl radicals can be generated, which significantly enhances the electrocatalytic efficiency of the Ti/SnO_2-Sb electrode. Besides, the doping of Bi, Sb, and other elements can greatly improve the conductivity and electrocatalytic ability of SnO_2 electrodes. There are several advantages of ATO. ATO can be easily and economically coated on a Ti substrate, making it into large areas for industrial applications. Therefore, this material has received tremendous research interest. SnO2 confers a low resistivity and good stability to electrodes, thus representing an excellent alternative for the removal of organic compounds in wastewater

2.4.1.4 TiO_2 NTAs/SnO_2-Sb_2O_3

Growing TiO_2 nanotubes from a Ti substrate has become a mature technique, and the TiO_2 nanotube anode favors hydroxyl radical production because it has a relatively large band gap ($\Delta E = 3.2$ eV). [33] The titanium dioxide nanoarray can provide enough specific surface area, enabling the SnO_2 layer to adhere to it better and prolong the actual lifetime of the electrode. The SnO_2 layer with good conductivity can significantly improve the whole electrode's conductivity and prolong the titanium dioxide nanotubes' lifetime. Although it has not been studied yet, the oxygen defects inside the titanium dioxide nanotubes will gradually decrease with the anodic reaction, leading to the loss of electrochemical activity of titanium dioxide nanotubes. Also, the nanotube structure can lower the exciton recombination rate, increasing the reaction rate of valence band holes with water. Consequently, we used TiO_2

nanotubes formed on a titanium mesh as the base material, and then it was coated with a $SnO_2-Sb_2O_3$ layer.

2.4.2   The BA oxidation with 4 anodes
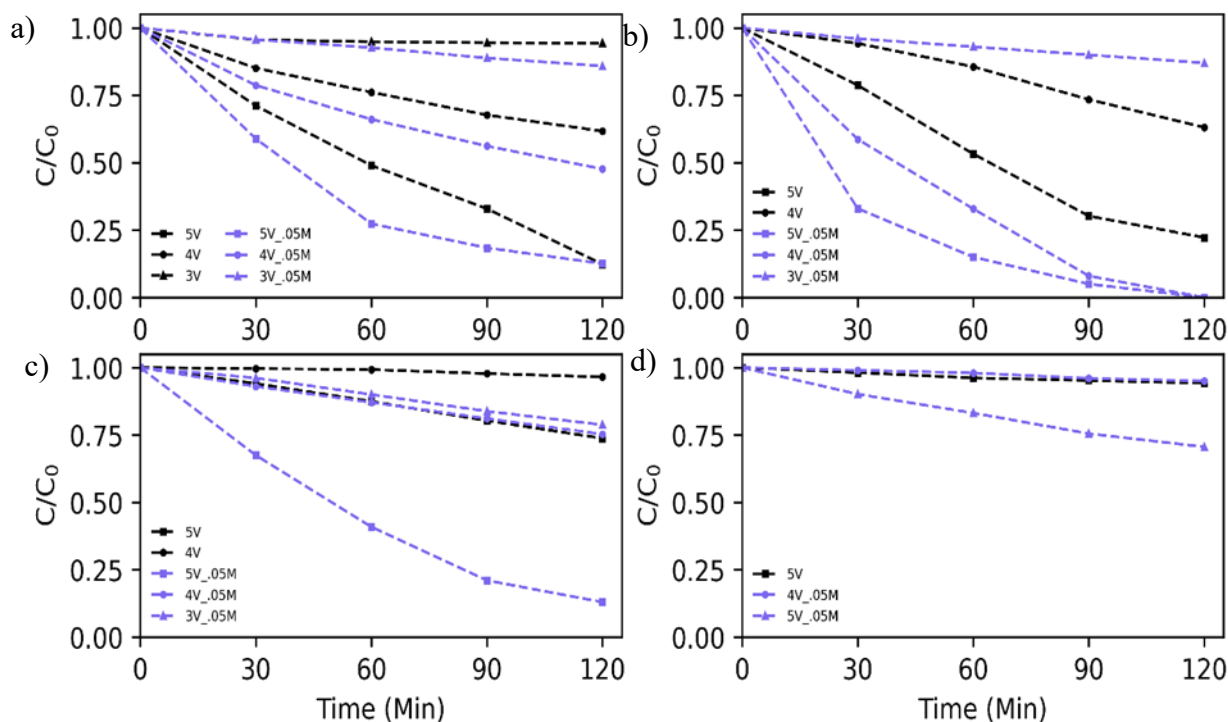
Figure 5 – Electrochemical oxidation of 20 ppm BA with different electrodes at various potentials. (a) BDD (b) PbO_2 (c) TiO_2 NTAs/SnO_2-Sb_2O_3 (d) Ti/SnO_2-Sb. The supporting electrolyte is 0 and 0.05 M Na_2SO_4 with a 20 ml/min flow rate.

The 20 ppm BA degradation experiments by BDD, PbO_2, Ti/SnO_2-Sb, and TiO_2 NTAs/SnO_2-Sb_2O_3 were tested under 3V,4V and 5V conditions for both 0 M and 0.05 M Na_2SO_4 solution. For the 0 M condition, the proton exchange membrane conducts the H^+ from anodes to the cathode while insulating the direct electrodes electrically. For 0.05 M Na_2SO_4
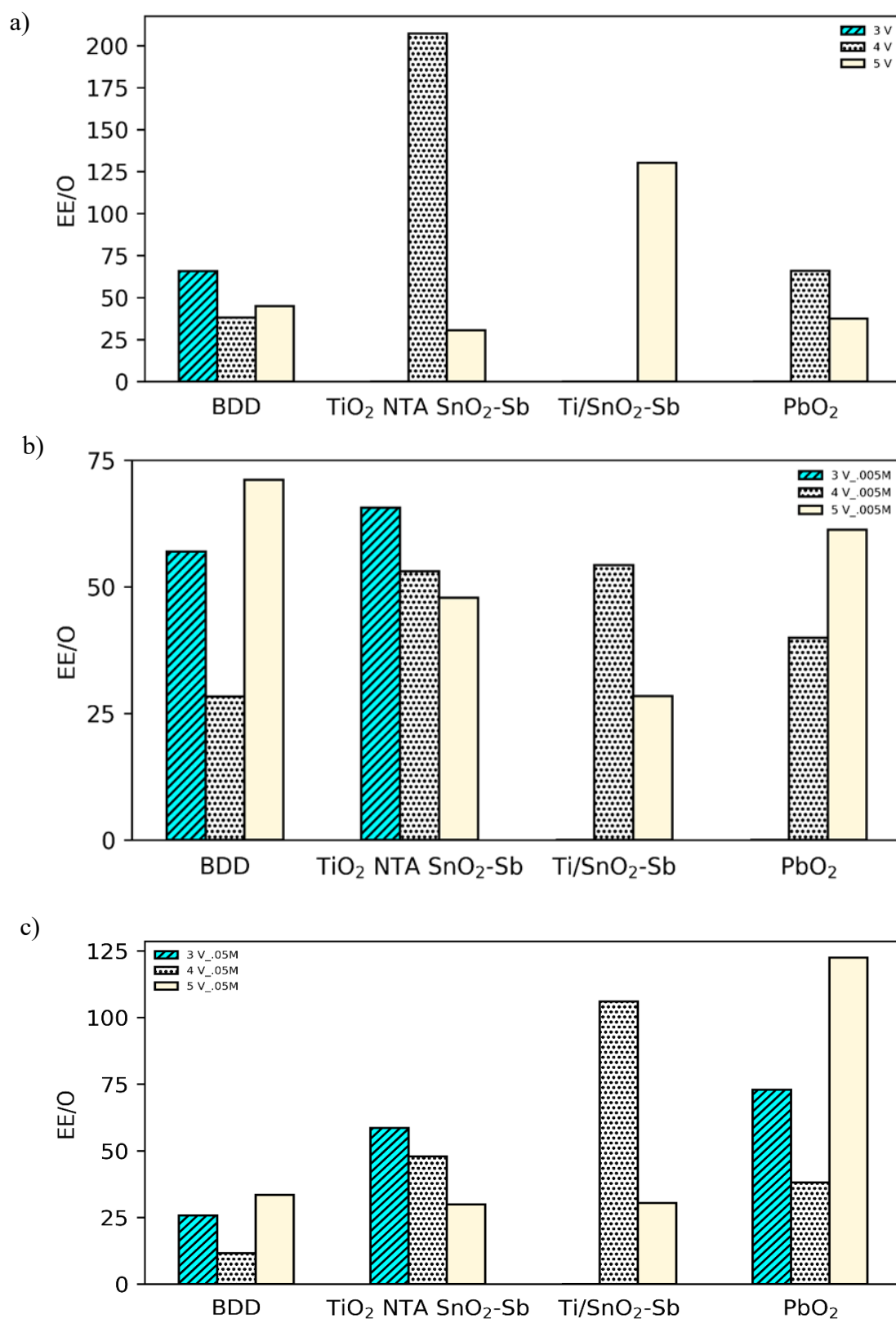
Figure 6 – The EE/O of 20 ppm BA oxidation by the BDD, TiO$_2$ NTAs/SnO$_2$-Sb$_2$O$_3$, Ti/SnO$_2$-Sb and PbO$_2$ with a) 0, b) 0.005 and c) 0.05 M Na$_2$SO$_4$.

solution, both the Na^+ and H^+ can transfer from anode to cathode. 0 M and 0.05 M solution is used to compare two distinctive wastewater sources, which help understand the EAOP-fuel cell energy recovery system's versatility in different electrolyte resistance (ohmic loss). Figure 5 tells the minimum voltage required for electrodes' effective oxidation. For the BDD electrode, 3V is the minimum voltage in both 0 and 0.05 M conditions, while for the PbO_2 and TiO_2 NTAs/SnO_2-Sb_2O_3 electrodes, 4V is the minimum voltage in non-electrolyte conditions. For Ti/SnO_2-Sb electrode, 4V is the minimum voltage for electrooxidation. The mass transfer limitation on the oxidation is evident with high applied voltage. The reaction rate of both BDD and PbO_2 in the 5 V condition gets smaller after a 1-hour oxidation reaction. This is also reflected in their EE/O value shown in Figure 6. Figure 6 shows the EE/O of the four electrodes in 0 and 0.005 and 0.05 M conditions.

The PbO_2's EE/O in 5V increases with increasing salt concentration, which indicates the increased current density contributes to the electrolysis of water instead of organic oxidation. Under various electrolyte concentrations, the optimal operating voltage for BDD is 4V. For PbO_2, 4V is also the optimal operating voltage with electrolyte. In non-electrolyte conditions, 5V is the optimal operation voltage for PbO_2. In contrast to BDD and PbO_2, the optimal operating voltage of both TiO_2 NTAs/SnO_2-Sb_2O_3 and Ti/SnO_2-Sb is 5V. One reason their optimal operation voltage is high is its high OEP and low electrode conductivity. In other words, hydroxyl radical generation is the limiting step for both of them instead of mass transfer limitation. Due to the high operation voltage's low theoretical energy recovery ratio, TiO_2 NTAs/SnO_2-Sb_2O_3 and Ti/SnO_2-Sb are not considered for the EAOP-fuel cell energy recovery system.

20

2.4.3 *The CE and the limiting current efficiency of EAOP-fuel cell energy recovery system*

Different initial BA oxidation performance was then evaluated using BDD as the anode. Table. 3 shows the COD removal percentage, current efficiency, and the EE/O of 20, 100, 200, and 500 ppm BA. What is striking in this table is the lowest EE/O in 3V for different initial BA concentrations that could help reach high energy savings of the EAOP-fuel cell energy recovery system. The current efficiency (CE) is calculated based on the COD removal percentage using Equation 9. In the 0.05 M Na_2SO_4 electrolyte condition, the current density remains almost constant with different initial BA concentrations. Therefore, the BA concentration effects on the current density are excluded. The CE is examined based on the applied voltage in the same current density condition. The CE increases as the initial BA rises from 20 to 500 ppm. At 500 ppm, the CE reaches 100% under 3 and 4 V conditions. The 100% CE refers to the that every electron comes from organic oxidation. It is believed to be in the best operating condition. However, with the increased CE, the EE/O did not decrease. Though the absolute COD reduction value is increasing, the COD removal percentage declines with the high CE, indicating that the current density is the limiting factor in a high COD situation instead of mass transfer limitation. Therefore, EE/O is increased due to an increment in initial concentration.

$$CE = \frac{FV(COD_0 - COD_t)}{8It} \qquad (9)$$

F is the Faraday constant; COD_0 and COD_t are the initial and final COD values after oxidation.

I is the current, and t is the time.

Table 3 – The Current efficiency of BA oxidation using the BDD electrode. The supporting electrolyte is 0.05 M. The initial BA concentration is 20,100, 200, and 500 ppm, respectively

Initial BA	Potential	Current Density	COD Removal	Current Efficiency	EE/O
ppm		mA/cm²	%	%	
20	5	21	81	3	33
20	4	4	67	11	11
20	3	2	20	5	25
100	5	22	66	9	57
100	4	4	37	28	45
100	3	2	20	25	30
200	5	22	67	23	56
200	4	4	36	73	43
200	3	2	16	68	32
500	5	23	56	38	76
500	4	4	28	100	64
500	3	2	13	100	36

Limiting current density (I_{lim}, A/m^2) (Equation 10) is a good indicator of the impact of mass transfer on the oxidation process. When the applied current density (I_{appl}, A/m^2) is higher than the limiting current density, the electrochemical oxidation is under mass transfer limitation, resulting in low current efficiency. The limiting current density is proportional to the COD value. It can be used to demonstrate more rigorously our previous statement that mass transport is not a limiting factor in the case of high COD under 3 and 4V. The mass transfer coefficient k_f is calculated by Equations 11, 12, and 13. The plot of the current efficiency and the ratio between the applied current density I_{appl} and I_{lim} demonstrates that the current efficiency could increase with the decreased ratio between I_{appl} and I_{lim}. Moreover, in theory, 100 % current efficiency could be obtained when the I_{appl} is equal to or smaller than the I_{lim}. In the experiment, when I_{appl}/ I_{lim} equals 1, the current efficiency of 3 V, 4 V, and 5 V condition are 0.098, 0.2805, and 0.3642, respectively. When the current density is sufficiently less than the limiting current density, 100 % CE is achieved. The CE under I_{appl}/ I_{lim} equals 1 condition is a characteristic number that can be used to characterize the ease of mass transfer. With increased applied potential, the characteristic number also increases. A larger value means that 100% CE can be achieved at a relatively larger current density. Therefore, the voltage may have been a positive factor in the characteristic number. Because the BA as a weak acid partially dissociates into its ions in an aqueous solution, the potential field will expedite the mass transfer of the BA anion to the anode surface. The relationship between the character number and voltage reported here appears to match the observed EE/O, that for BDD and PbO$_2$ electrode the 4 V is the optimal operating condition for the initial 20 ppm BA condition. In that conditions, the mass transfer has a more significant impact on the 3 V condition than the 4 V.

23

$$I_{lim} = 4Fk_fCOD \tag{10}$$

$$Sc = \frac{\mu}{\rho \cdot D_l} \tag{11}$$

$$Sh = \frac{k_f \cdot d}{D_l} = 3.3 \cdot \left(\frac{d}{l} \cdot Re \cdot Sc\right)^{\frac{1}{3}} \tag{12}$$

$$Re = \frac{\rho \cdot u \cdot d}{\mu} \tag{13}$$

4 is the number of moles of transferred electrons when one mole COD is oxidized; F is Faraday's constant (96485 C/mol).
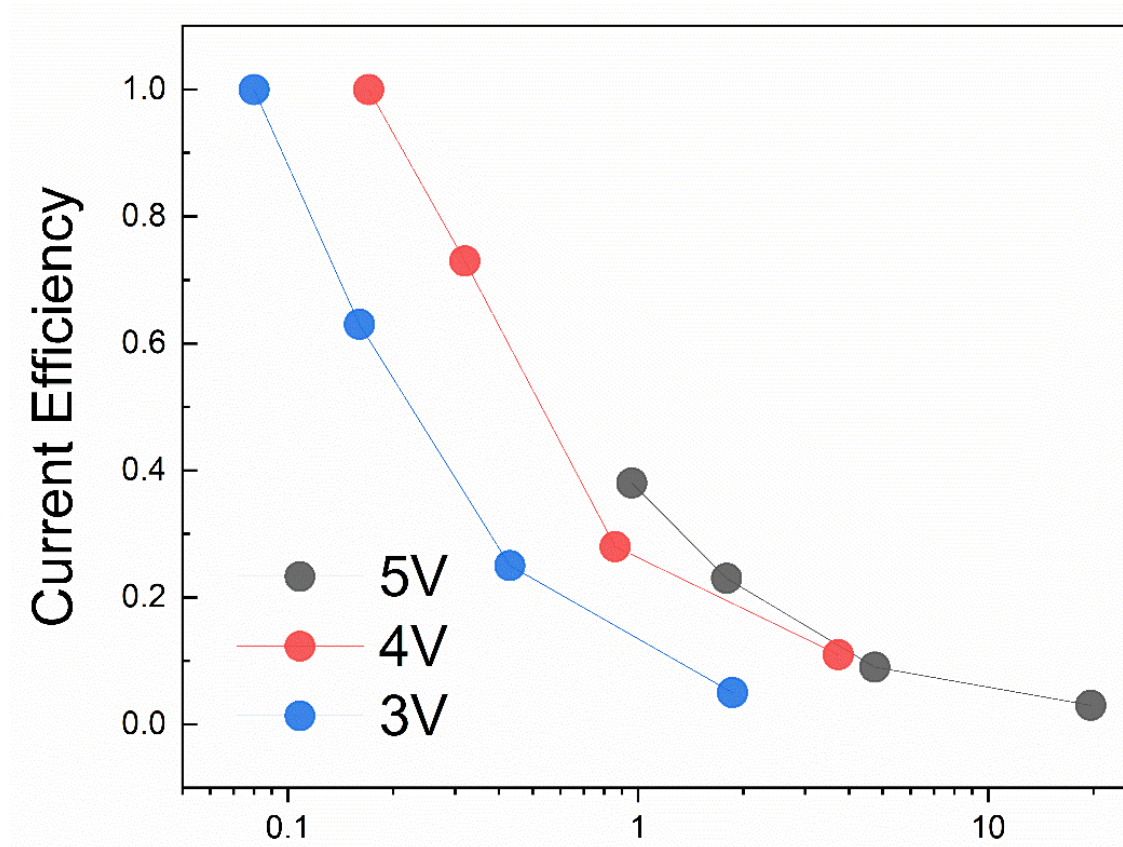
Figure 7 – The current efficiency vs the I_a/I_{lim} for EAOP fuel cell system with BDD anode under 3V, 4V and 5V.

2.4.4   The energy recovery of the EAOP-fuel cell energy recovery system

Figure 8 shows the fuel cell polarization curve of the hydrogen produced by the 3, 4,

and 5 V EAOP reactor at 20° C. The polarization behavior was examined for H$_2$/air and H$_2$/O$_2$

modes. The peak power density for H$_2$/O$_2$ was 69 mW/cm^2, and for H$_2$/air was 34
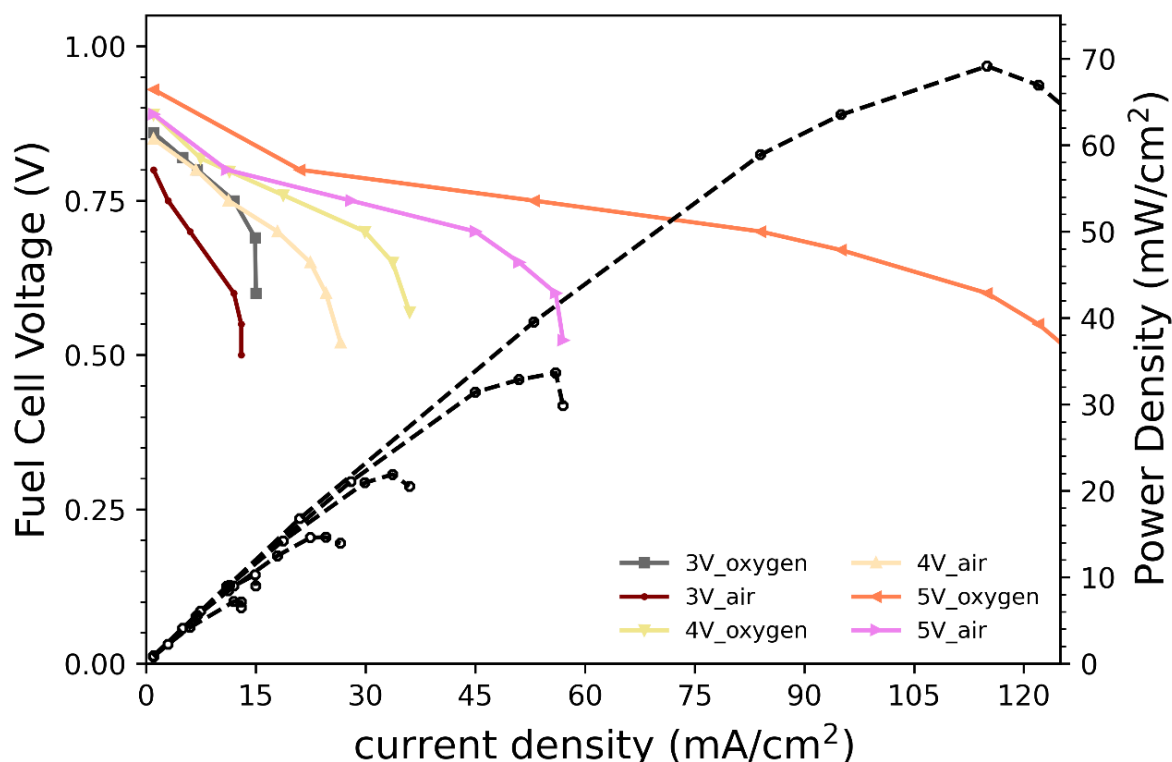
Figure 8 –The energy recovery ratio of the EAOP-fuel cell system in 3, 4, and 5 V with H$_2$-air or H$_2$-oxygen mode

mW/cm^2. The ideal fuel cell voltage is 1.2 V. In our experiment, the fuel cell output voltage

is around 0.8 to 0.9 V, which is a typical value for most experimental fuel cells. Due to ohmic

losses, the cell potential drops linearly with current density for moderate current densities.

The voltage drop due to ohmic losses is evident in the 4 and 5V modes, especially in the H$_2$-

oxygen mode. The hydrogen flow is small in 3V conditions, given the low current density for

hydrogen production. Therefore, there is no obvious ohmic losses plateau. Instead, similar to

the electrochemical oxidation process, mass transfer is the limiting factor when the supplied

hydrogen is not enough for the fuel cell. Due to the mass transfer limitation, the IV

polarization curve drops quickly to 3 V in both H2-air and H2-oxygen mode. The power

density of the fuel cell is calculated based on the polarization curve. Moreover, the energy

recovery ratio of the EAOP-fuel cell system is shown in Figure 9. Compared to the

theoretical number,
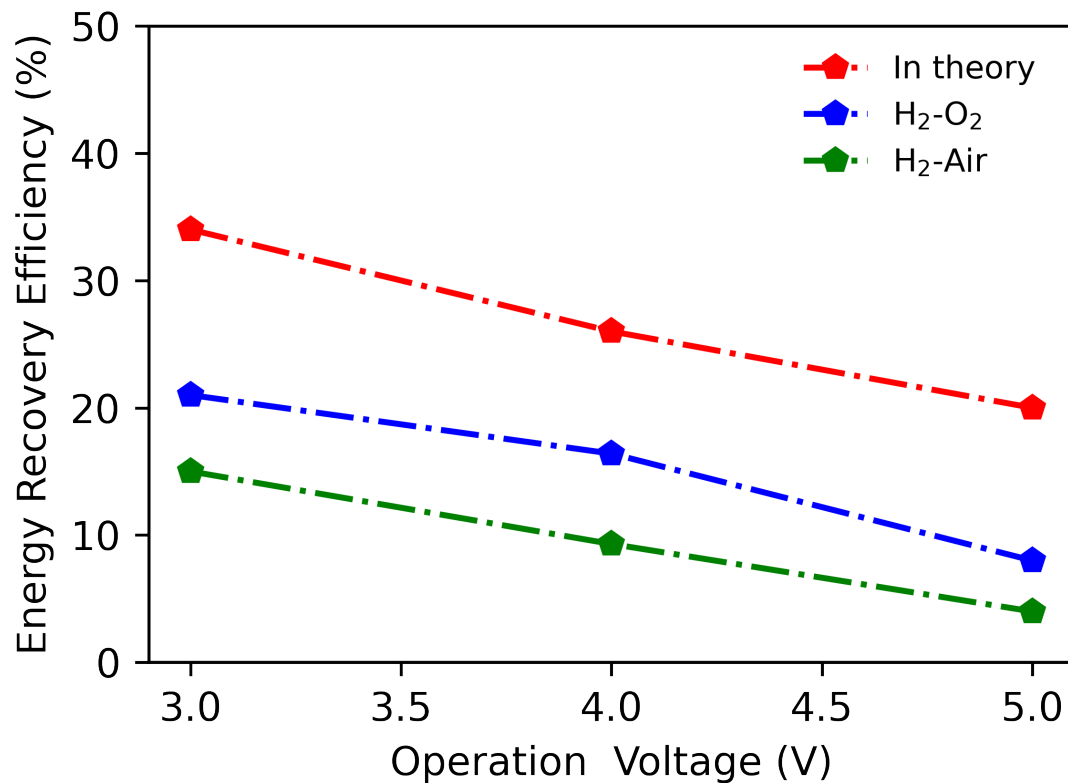
Figure 9 – The polarization curve and power density curve for the fuel cell in both H₂ oxygen mode and H₂ air mode.

 the experimental energy recovery ratio still has space to improve by 10 % to 15 %. The

highest energy recovery efficiency is 21 % and 15 %, respectively, for 3V H_2 -oxygen and

H_2-air mode. 5 V is not an optimal operating voltage for the EAOP-fuel cell energy recovery

systems. Compared to the other two voltage, the experimental energy recovery ratio

compared to the theoretical value at 5V is also the lowest. A likely explanation is that a high

percentage of hydrogen leakage results from poor sealing of the system since it is a primitive model system. The EAOP-fuel cell produces hydrogen substantially faster than the other two conditions, generating gas pressure. This issue can be resolved with more advanced engineering equipment. However, this result is sufficient to indicate that 5V is not an optimal working state. 3v is the optimal operating voltage. However, his average current density is low. I believe this system can initially be implemented in environments with warmer wastewater temperatures to overcome this issue. The electrochemical reaction rate will be significantly faster at a higher water temperature. Hence the current density at the same voltage condition can be significantly enhanced.

2.5   Conclusions

The functioning of the EAOP-fuel cell energy recovery system under diverse operating conditions demonstrates that this system can cut energy consumption successfully at low operating voltages. In order to satisfy this criterion, electrodes should be highly conductive and electrochemically active in low operation voltage. PbO_2 and BDD are the two most suited among the four widely used anodes. The other two are also highly efficient EAOP anodes but should be operated in high voltage conditions. In the future, electrode development should focus on adapting to the EAOP-fuel cell energy recovery system. Compared to an excessive focus on OEP and hydroxyl radical generation percentage, the electrode which could oxidize pollutants by both direct and indirect oxidation is expected. The EAOP-fuel cell system can operate below 3V to achieve higher energy recovery efficiency for pollutants that could be easily oxidized, like dyes and Biomass. Mass transfer results show that 100 % CE is available

27

when the applied current density is much smaller than the limiting current density. However, to be noticed, high CE cannot promise low energy consumption. The energy efficiency is controlled by both the operating voltage and current efficiency. For EAOP-fuel cell efficiency, the fuel cell energy recovery ratio is added.

Considerably more work will be done to improve the EAOP-fuel cell energy recovery system. For instance, a cutting-edge air-breathing fuel cell can effectively increase the fuel cell's H_2-air mode efficiency. In the future, the EAOP-fuel cell energy recovery system can be integrated with solar power and other forms of renewable energy. Eventually, it may be conceivable to develop a wastewater treatment system to balance its energy consumption.

CHAPTER 3. ELECTROCHEMICAL DEGRADATION OF PFOA ON FLOW THROUGH EAOP-FUEL CELL ENERGY RECOVERY SYSTEM

3.1 Introduction

Recent research has revealed that improving mass transport positively impacts the efficiency of EAOPs. The EAOPs oxide the organic by direct and indirect oxidation (hydroxyl radical generation) on the anode surface. Consequently, two strategies are improving the surface area of the anode and increasing the mass transfer efficiency in the boundary layer. The flow through electrodes with micro pores can improve the above two aspects and is widely studied in the EAOP fields. In the report, the flow through anodes is 10 times more energy efficient than the traditional parallel flow-by anodes.[34] Two widely studied flow through EAOPs anode structure is shown in Figure 10. Figure 10. (a) shows the reactive ceramic membrane (REM) with cross-flow filtration mode. Figure 10. (b) shows the flow-through plate electrodes. The average pore size of REM ranges from 1-5 um, which provides a high surface area for electro-oxidation with high surface roughness.[35] The pore size is much smaller than the stagnant boundary of 100 um, resulting in enhanced mass transfer.[36] The average pore size ranges from 10 to 100 um for flow-through plate electrodes.[37] Compared to REM, the flow-through plate electrodes are easier to scale up. However, the void ratio and average pore size are restricted by mechanical strength, considering the pressure head of the water flow. However, both electrodes encounter two obvious problems for industrial application.

1) Electrode fouling and clogging. In long-term operation, there will be residues leaving inside

the electrodes. This will increase the operating pressure and cost of the operation and reduce the oxidation efficiency of the reactor. Considering the thickness of the reactor and the high specific surface area, it will be difficult to clean the anodes.

2) Improve the effective surface area. The surface area obtained by mercury intrusion experiments is much higher than the electrochemical active surface area. It is understood that the current density is not uniformly distributed through the electrode. However, if the current is overly localized in particular regions, it will lead to low oxidation efficiency. In addition, it will cause extra energy consumption, such as high-pressure pumping.
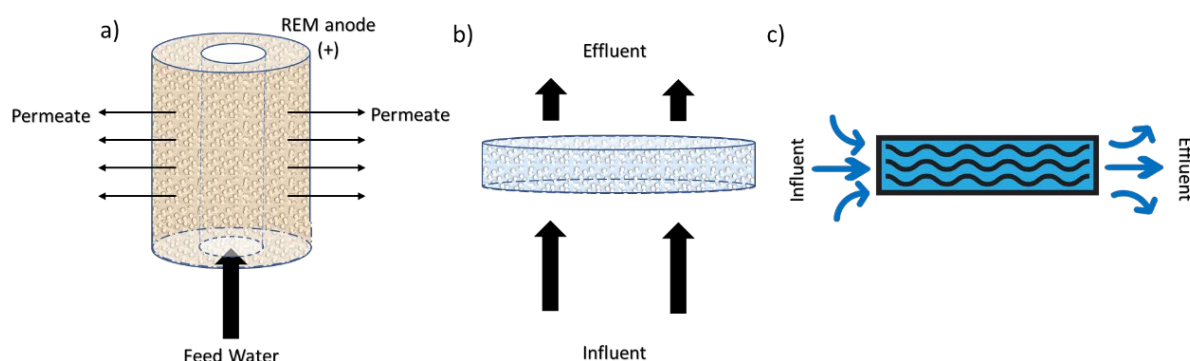
Figure 10 – a) the reactive ceramic membrane (REM) with cross-flow filtration mode. b) the flow-through plate electrodes. c) the flow through multilayer parallel electrodes

We proposed a flow through multilayer parallel electrodes in this study to solve the above problems. The electrode is composed of layers of wire mesh. The high mesh count (200 or above) is widely used for water oil filtration because it is easy to be operated and maintained for industry applications. [38] The study of wire mesh anode for EAOPs is still in the early stage, and most focus on single-pass layer flow-through systems. [39-41] Compared with metal water oil filtration, wire mesh electrodes' design and manufacturing requirements for EAOPs are more demanding. The active electrode material is coated on the base wire mesh. The

deformation of the anode and the high flow rate of water could cause the active layer to pile off. Oxygen production accelerates the process's deterioration due to the gas pressure. Electrode shortcoming is another crucial issue to be concerned about. With a smaller electrode distance, the ohmic loss could be reduced, but given the deformation, a wider electrode distance is required for the wire mesh electrode. The above issues are solved by using the multiple layers wire mesh setup. The water flows transported through the electrodes by cross-flow pattern to avoid a direct impact on the electrode coating. The multiple-layer stack wire mesh shows more excellent mechanical stability in terms of deformation. In addition, the new design offers the following benefits: the electrode distance between the stacked wire meshes could shrink down to boundary layer thickness (100 um) to enhance the mass transfer. In addition, the electrode's effective surface area is also increased compared to the flat electrode. For industrial application, the flow through multilayer parallel electrodes have two advantages compared to porous metal foam electrode: 1) simplicity of maintenance. The electrode may be readily removed and cleaned if it is fouling or clogged. 2) It can be paired with our EAOP energy recovery system to reduce operating costs. The design of an EAOP system with a hydrogen fuel cell energy recovery system is proposed in our previous paper. However, it is incompatible with the REM or the flow-through plate electrode. Because the hydrogen and oxygen chambers are intermingled, it is difficult to separate and collect the hydrogen for energy recovery. The energy recovery system is important for the flow through the EAOPs system. Because when the current efficiency hits 100 percent of the theoretical maximum, lowering the operating voltage is the only feasible option. Recovering energy from hydrogen is an indirect method of lowering the operating voltage. In terms of PFOA/PFOS oxidation, several studies have reported a high

defloration rate and TOC removal efficiency close to theatrical efficiency.[42, 43] Therefore, there will be less room for additional efficiency improvement through electrode material enhancement. The flow through multilayer parallel electrodes shows a good capability of the EAOP energy recovery system.

EAOPs proved to be an effective method for PFACs treatment. Poly- and perfluoroalkyl substances (PFASs) pose a serious human health risk due to their biochanin enrichment. [44, 45] They have been globally detected in groundwaters, landfill leachates, wastewater treatment plants, and drinking water.[46] Perfluorooctanoic acid (PFOA) has received the greatest attention because of its abundance, bioaccumulation, and persistence. It is challenging to break down PFOA since the carbon-fluorine bond energy (116 kcal/mol) is the strongest single bond in organic chemistry.[6] The hydroxyl radicals were not adequate for PFOA removal, and the direct oxidation at the anode surface initiates the PFOA oxidation.[47, 48] BDD (boron-doped diamond) is the gold standard electrode of EAOPs anode, and its oxidation capability of PFOA is reported in the literature.[42, 49] The TiO_2 NTAs plate anode also shows great removal and defluorination rate for PFOA oxidation due to the wide bandgap of TiO_2 NTAs (~ 3.2 eV).[43] In our previous study, the TiO_2 NTAs are covered by SnO_2 -Sb_2O_3 DSA (Dimensionally stable anode) layer for higher electroactivity and oxidation efficiency for organic removal. Based on our knowledge, there is no study on PFOA oxidation by the TiO_2 NTAs SnO_2-Sb_2O_3 electrode.[17] The Ti_4O_7 was a recently emerged material for PFOA oxidation because of its good oxidation capability and unique electrochemical properties. Ti_4O_7 are composed of two-dimensional chains of titania octahedral, with an oxygen atom missing from every 7th layer to compensate for the decrease in stoichiometry.[50, 51]This structure confers to Ti_4O_7 an

electrical conductivity comparable to that of metals and corrosion resistance comparable to that of ceramics.[52] The Ti_4O_7 powder could be sintered to foam porous REM electrodes. The flow through REM Ti_4O_7 ceramic anodes achieved 99.9% removal of PFOA in 2 h, and the electrical efficiency per log order reduction (EE/O) values of the Ti_4O_7 are much lower than the flow by BDD electrode in the same experimental setup. [53] It is concluded that mass transfer is the critical factor for EAOPs efficiency. For BDD, it is hard to improve the mass transfer by improving the electrode surface area per volume or increasing the porosity of the electrode because its morphology is restricted to the flat plate due to the fabrication method. Mostly, the boron-doped diamond is coated on Ti or Silica substrate by CVD (chemical vapor deposition) methods.[54] As previously stated, the flow through multilayer parallel electrodes is an ideal setup for improved mass transfer and energy recovery purposes. TiO_2 NTAs/ SnO_2 -Sb_2O_3 could be used to assemble flow through multiple layer wire mesh anode because the anodization methods of the Ti wire mesh to TiO_2 Nanotube arrays have been widely studied.[55-57] Ti_4O_7 wire mesh could also be made by sputtering the Ti_4O_7 power on the Ti wire mesh.

This study investigated the oxidation of PFOA using a flow-through multiplayer parallel wire mesh anode. The electrochemical oxidation of the PFOA was investigated in a flow-through operation mode as a function of anode material and applied potential. The defluorination and energy consumption are compared to flat plate BDD electrodes. In addition, the layer of the electrodes and the energy recovery ratio of the system is also investigated.

3.2   Synthesis methods

3.2.1 Preparation of Ti_4O_7 wire mesh anode

Ti_4O_7 wire mesh anodes were prepared by a high-temperature sputtering method. Ti_4O_7 powders were purchased from Shanghai Epoch Material Co., Ltd. Ti_4O_7 powders were mixed with 1% polyacrylamide/polyvinyl alcohol 90%, 10%, and water to form a slurry, and the slurry was spray-dried to the titanium wire mesh. Then the Ti_4O_7 wire mesh anodes were dried and sintered at 900 °C in a vacuum chamber for 24 h. The XPS spectrum of the Ti_4O_7 wire mesh was shown in Appendix.

3.2.2 Preparation of TiO_2 NTAs/SnO_2 Sb_2O_3 wire mesh

The first step is fabricating the TiO_2 nanotube substrate by electrochemical anodization of porous Ti at 60 V in EG electrolyte with 0.25 wt % NH_4F and 2 wt % H_2O for 0.5 h. Then, the oxidized substrate was cleaned using deionized water and ultrasound (25 w/L w power, 40 kHz) for 10 minutes. Then the oxidized substrate was anodized in the exact EG solutions for another 4 hours at 60 V. The XRD structure of TiO_2 nanotube arrays is shown in Appendix. The sol-gel coting step of the TiO_2 NTAs substrate is in the previous paper.[34]

3.2.3 Reactor setup and modeling

The flow-through reactor had a reservoir and a differential column batch reactor (DCBR) system. A simplified kinetic model is used to compare the reaction rate of different electrodes, as shown in Equations 14 and 15. Since PFOA destruction follows a pseudo-first-order reaction, electrical efficiency per log order reduction (EE/O) is used to determine the efficiency of the various anodes and is calculated using Equation 2.

$$(V + V_r)\frac{dc}{dt} = -k_{obs} \cdot C \cdot V \tag{14}$$

$$C_t = C_0 \cdot e^{-\frac{k_{obs} \cdot V \cdot t}{V + V_r}} \tag{15}$$

The mass transfer coefficient (k_f) of both flat plate and multiple layer wire mesh electrodes is calculated based on Equations 12 and 16, respectively. The PFOA diffusion coefficient D_f is 4.37 x 10^{-6} cm^2s^{-1}, according to experimental findings.[58] Gnielinski equation (Equation 16) is used for porous structure electrodes. The characteristic d of the porous electrode is determined by the thickness of the wire mesh (wire diameter), which is confirmed

Table 4 – mass transfer coefficient as a function of Reynolds and Schmidt number for mass transfer coefficient of multiple layer wire mesh electrodes based on Gnielinski equation.

Correlation Multiple layer wire mesh electrodes		Range of validity
$k_f = \dfrac{[1 + 1.5 \times (1 - \varepsilon)]D_f}{d}(2 + 0.644 \times Re^{1/2} \cdot Sc^{1/3})$	(16)	$Pe = Re \cdot Sc > 500$
		$0.7 < Sc < 10^4$ $Re < 2 \times 10^4$ $0.26 < \varepsilon < 0.935$
$Re = \dfrac{\rho \cdot u \cdot d \cdot \phi}{\varepsilon \cdot \mu_f}$	(17)	
$Sc = \dfrac{\mu}{\rho_f \cdot D_f}$	(18)	

k_f = fluid-phase mass transfer coefficient, m/s.

D_f = fluid-phase diffusion coefficient, m^2/s.

ε = void fraction, dimensionless.

d = characteristic length, m.

ρ_f = fluid-phase density, kg/m^3.

ϕ = sphercity.

v_s = superficial liquid velocity, m/s.

μ_f = fluid-phase viscosity, kg/m·s.

Re = Reynolds number, dimensionless.

Sc = Schmidt number, dimensionless.

d is the height of the flow channel (m)

3.3   Results and discussion

3.3.1   Characterization of Ti_4O_7 wire mesh and TiO_2 NTAs SnO_2 Sb_2O_3 wire mesh electrodes

The characterization of electrodes demonstrated the successful fabrication of wire mesh anode, and the surface area of electrodes is also compared. The SEM images of the Ti_4O_7 wire mesh are shown in Figure 11. a-c. The SEM of the TiO_2 NTAs and TiO_2 NTAs/SnO_2-Sb_2O_3 are listed in Figure 11. d-n and g, respectively. The TiO_2 NTAs are uniformly grown on the Ti wire mesh. Then, a thin layer of SnO_2-Sb_2O_3 covered the surface of the electrodes. Wire mesh electrode surface area is calculated based on the characterization results. The surface area of Ti_4O_7 mesh and TiO_2 NTAs/SnO_2-Sb_2O_3 are 8.3 and 2.75 times larger than the surface area of the flat plate electrode. Details on the derivation are shown in TEXT A.S1. The 100 wire count mesh size parameter listed in the Appendix is also used for calculation.
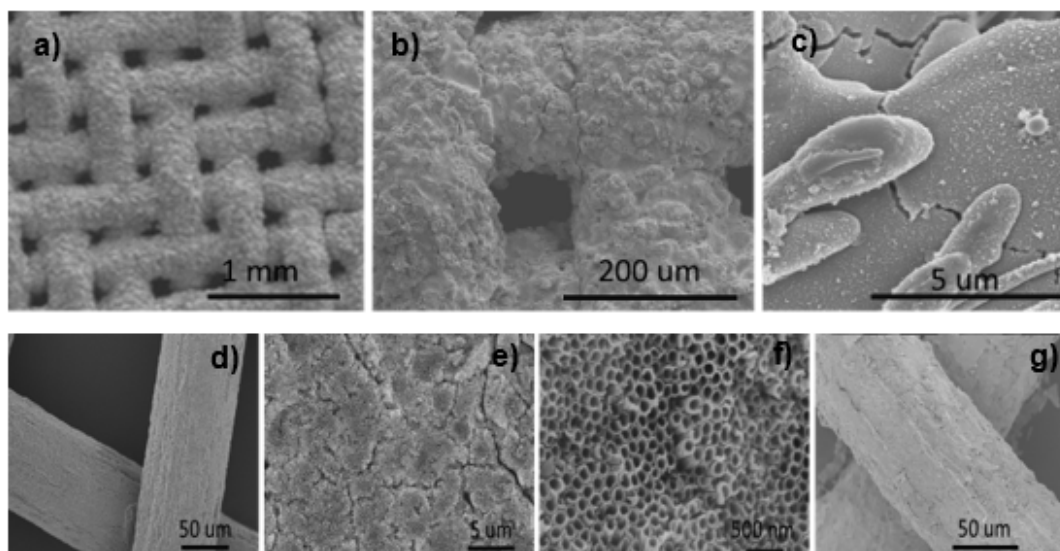
Figure 11 – The SEM images of Ti4O7 wire mesh (a-c); TiO2 NTAs before sol gel (d-f) and TiO2 NTAs SnO2 Sb2O3 (g)

3.3.2   Electrochemical properties

The LSV (Linear sweep voltammetry) of BDD, single layer Ti_4O_7, and TiO_2 NTAs/SnO_2-Sb_2O_3 was shown in Figure 12. Ti_4O_7 has much lower OEP (~ 1.5 eV/NHE) than the TiO_2 NTAs/SnO_2-Sb_2O_3 and BDD electrodes. The OCP is 2.5 V and 2.3 V vs. NHE for BDD and TiO_2 NTAs/SnO_2-Sb_2O_3 electrodes. These results further support the idea that direct oxidation is the main oxidation pathway of the Ti_4O_7. [61] Because the redox potential of hydroxyl radical is 2.7 V/ NHE, which is much beyond the OCP of the Ti_4O_7. The OEP of BDD and the TiO_2 NTAs/SnO_2-Sb_2O_3 proved their capability for hydroxyl radical generation.
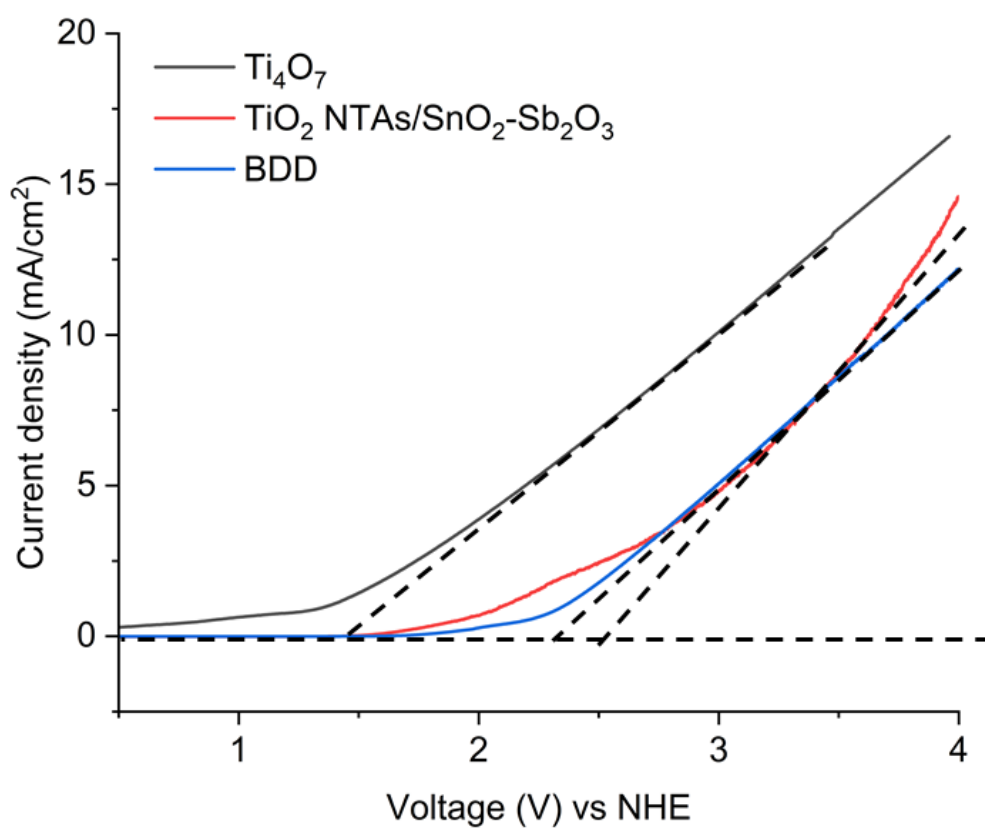
Figure 12 – The LSV of the BDD, TiO₂ NTAs/SnO2-Sb₂O₃, and Ti₄O₇. 0.1 M Na₂SO₄, 1 cm electrode spacing. Reference electrode: saturated calomel electrode.

a)
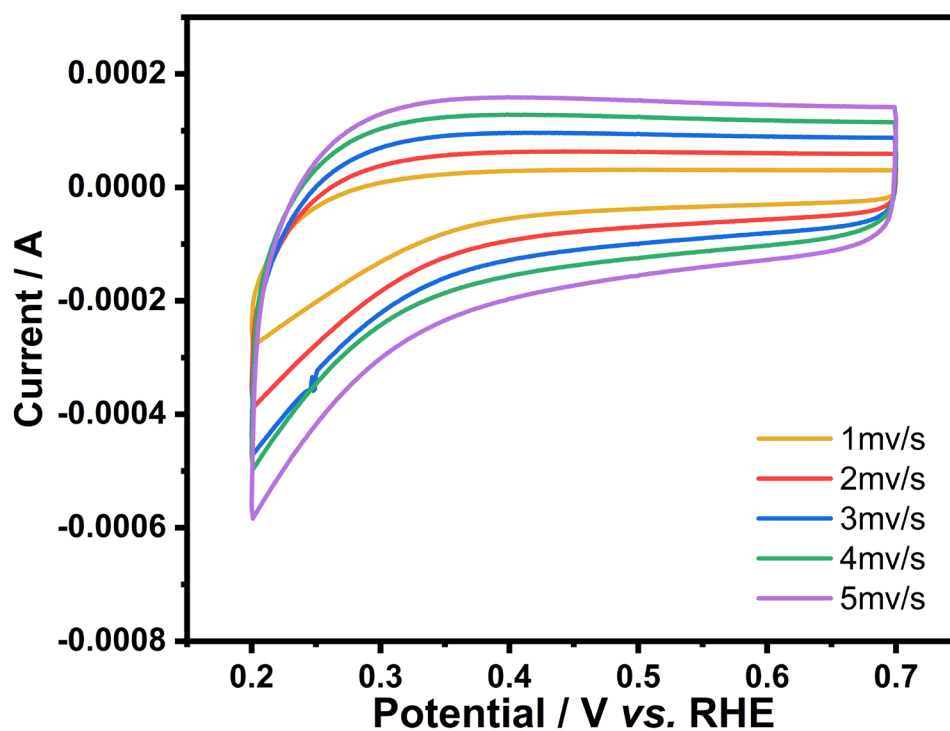
b)
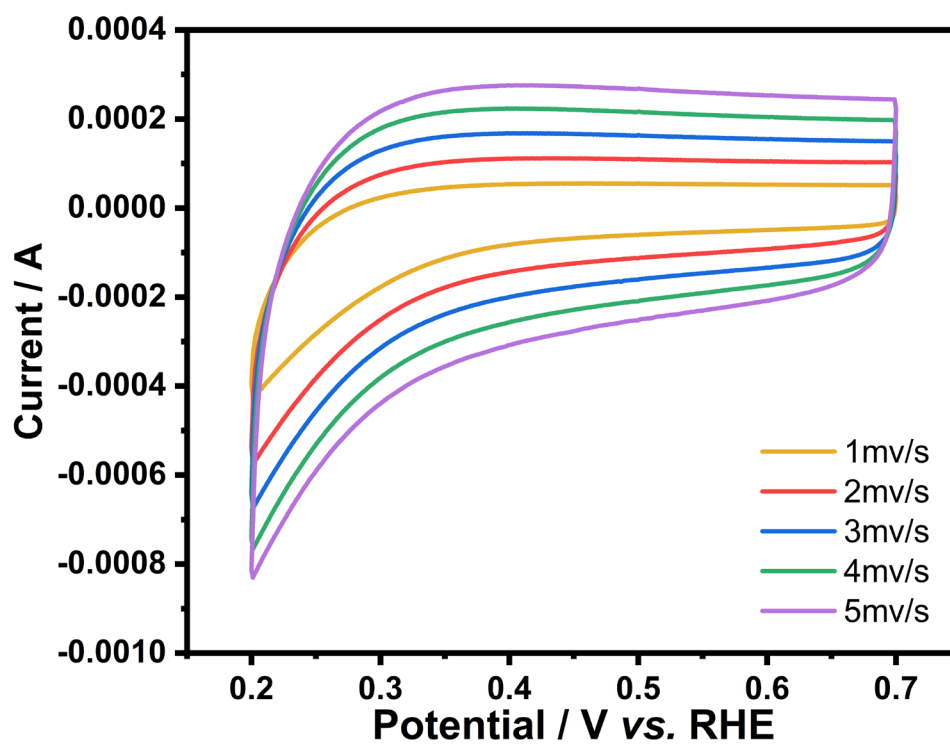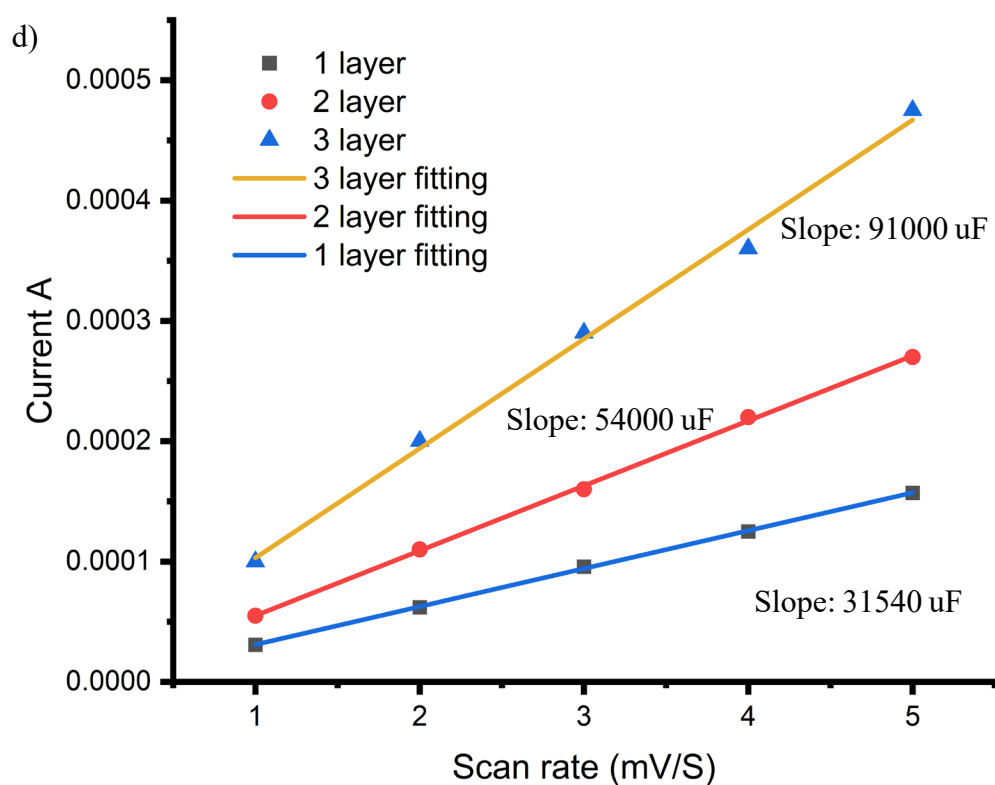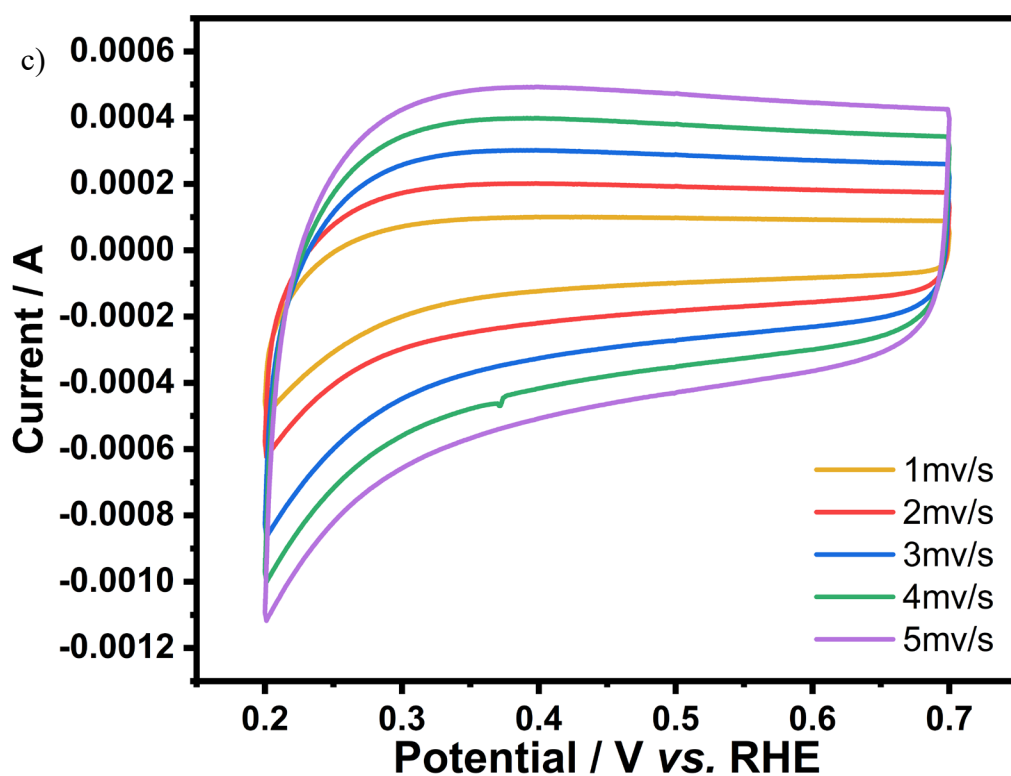
Figure 13 - Effective electrochemical active surface area tests of Ti₄O₇ wire mesh electrode (a) 1 layer, (b) 2 layer, and (c) 3 layer (d) electrochemical double-layer capacity of Ti₄O₇ wire mesh electrode.

The electrochemical active surface area (ECSA) of different layers of Ti_4O_7 wire mesh was also examined by Cyclic Voltammetry methods, as shown in Figure 13.d. The discharge capacity (60 μF cm^{-2}) is the standard value of metal oxide.[62] The ECSA of 1, 2, and 3 layers of Ti_4O_7 wire mesh are 525, 900, and 1510 cm^2, respectively. This indicates that increasing the number of layers can effectively increase the effective electrode area.

3.3.3 PFOA oxidation by Ti_4O_7, BDD, and TiO_2 NTAs/SnO_2-Sb_2O_3

The electrode performance is evaluated through three aspects: PFOA degradation efficiency, defluorination, and TOC removal ratio. The EE/O is calculated to evaluate degradation efficiency with the different electrodes and applied voltage. Figure 14 demonstrates that at 3V, the three-layer Ti_4O_7 electrode has the lowest EE/O. The eight-hour oxidation experiment is conducted for the 3V condition, and the concentration profile is shown in Appendix. For flat plate BDD, its lowest EE/O is obtained at 3V condition. At the same condition, the three-layer TiO_2 NTAs/SnO_2-Sb_2O_3 anode did not show the oxidation capability of PFOA. This is inconsistent with the 3V BA oxidation 3V results discussed in Chapter 2. For TiO_2 NTAs/SnO_2-Sb_2O_3 anode, 3V cannot excite surface hole and hydroxyl radical generation. In general, the increasing voltage will result in increased energy consumption. However, the EE/O increase rate of BDD is much larger than that of Ti_4O_7 wire mesh electrodes. However, for electrode BDD, the rate of increase in EE/O with increasing voltage is significantly greater than for electrode Ti_4O_7. The mass transfer limitation may cause high energy consumption of BDD.

Defluorination and TOC removal ratio is shown in Figure **14**. Defloration is defined as the free florid in the solution divided by the florid concentration in the initial PFOA concentration. Free fluoride is produced with the C–F bond broken. TOC and PFOA removal ratio comparison revealed that TOC removal, defluorination, and PFOA removal were closely synchronized. The corresponding current density of the three-layer Ti_4O_7, three-layer TiO_2 NTAs/SnO_2-Sb_2O_3, and BDD are 3.1 mA/cm^2, 20.7 mA/cm^2, and 24 mA/cm^2, respectively under 5 V condition. Given the difference in the current density, the comparison with the TOC /PFOA removal percentage is more straightforward. The TOC/PFOA ratio is 90%, 80%, and 95% for Ti_4O_7, BDD, and TiO_2 NTAs/SnO_2-Sb_2O_3. It indicates that TiO_2 NTAs/SnO_2-Sb_2O_3 has the highest mineralization efficiency. The mineralization ratio of the Ti_4O_7 and BDD are consistent with the reported value.[49, 53] The defluorination percentage/ TOC removal percentage are also compared. The BDD and Ti_4O_7 are around 65%, while the TiO_2 NTAs/SnO_2-Sb_2O_3 is 70%. It indicates stronger C-F bond break power on TiO_2 NTAs/SnO_2-Sb_2O_3. However, the TiO_2 NTAs/SnO_2-Sb_2O_3 have higher mineralization efficiency. However, from the energy efficiency, the flow through Ti_4O_7 is selected for the rest of part study.
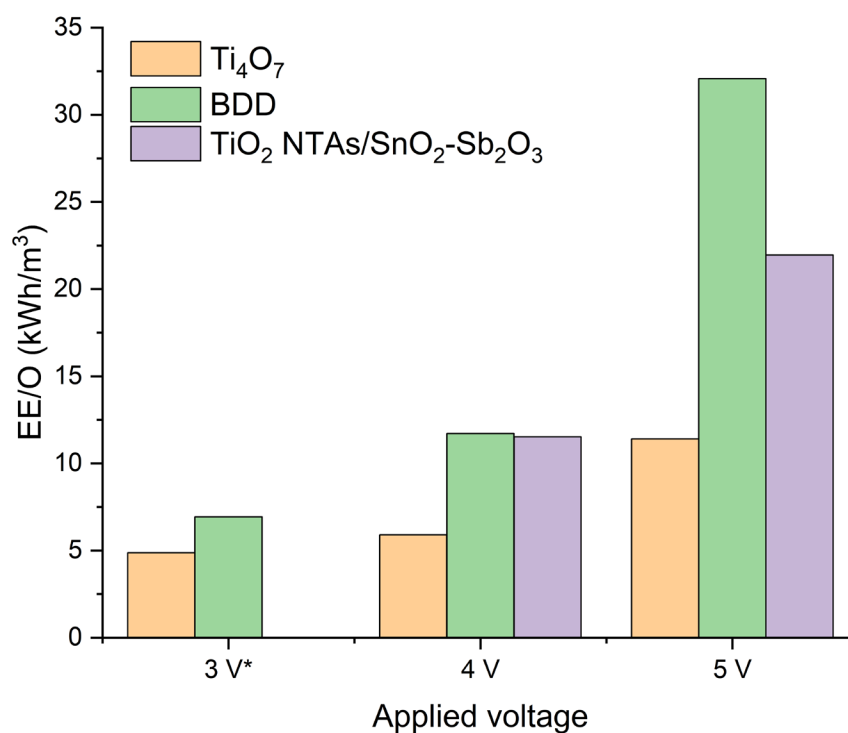
Figure 14 – The EE/O of the flow through three-layer Ti₄O₇, flow through three-layer TiO₂ NTAs/SnO₂-Sb₂O₃, and flat plate BDD. The initial PFOA concentration: 50 ppm; Supporting electrolyte: 0.05 M NaSO₄. Flow rate: 20 ml/min. The fluid velocity for three wire mesh electrodes is 0.01 m/s. The fluid velocity for the BDD electrode is 0.002 m/s. Operation time: 2 hours. * 3V flow through three-layer Ti₄O₇ operation time: 8 hours.
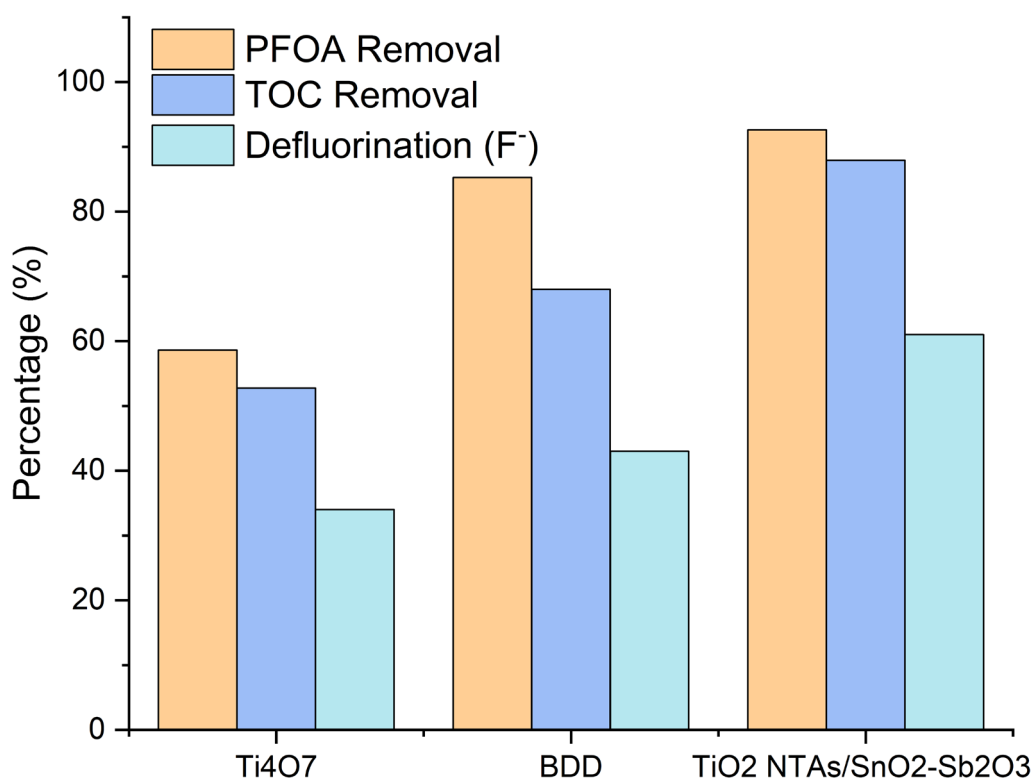
Figure 15 –The TOC, defluorination, and PFOA removal percentage of the flow through three-layer Ti4O7, flow through three-layer TiO2 NTAs/SnO2-Sb2O3, and flat plate BDD at 5V condition. The initial PFOA concentration: 50 ppm; Supporting electrolyte: 0.05 M NaSO4. Flow rate: 20 ml/min.

3.3.4   The layers of flow through Ti₄O₇ wire mesh anode

Figure 16 shows the degradation of PFOA by different Ti₄O₇ wire layer number and their EE/O in comparison with the BDD anode. The electro-oxidation percentage is increased with the increased layer numbers, especially when the number of layers increases from one to two. The EE/O did not change obviously when the number of the layers above three. The EE/O is almost identical for the single layer Ti₄O₇ wire mesh and BDD electrode. For single layer Ti₄O₇ wire mesh, though it has a parotic-like structure, it still works in flow by mode. When three-layer wire mesh is assembled, flow through porous flow pattern is established. Moreover, further increasing the number is not so helpful.
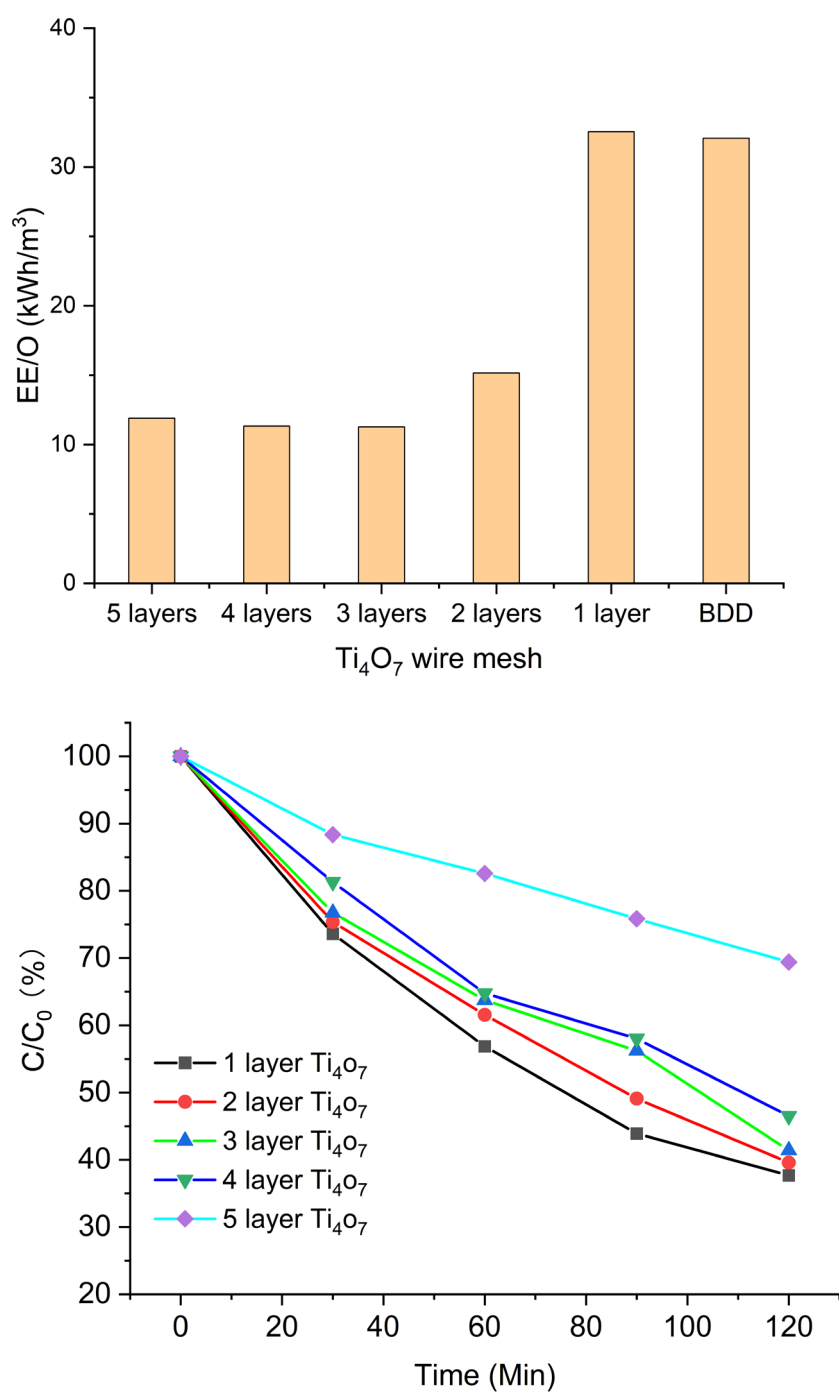
Figure 16 – The EE/O of different layer numbers Ti4O7 wire mesh anode and the corresponding PFOA oxidation percentage profile in 2 hours under 5V. The initial PFOA concentration: 50 ppm; Supporting electrolyte: 0.05 M NaSO4. Flow rate: 20 ml/min.

3.3.5 Kinetic analysis of the wire mesh electrodes

The pseudo-first-order model can fit the change of PFOA concentration, based on which the pseudo-first-order (k_{obs}) was calculated for Ti_4O_7 wire mesh and BDD electrode, respectively.

The experimental reaction rate constant (k_{obs}) of PFOA on Ti_4O_7 is controlled by both the mass transfer rate ($k_f \cdot a$, s^{-1}) of PFOA and the reaction rate per current density (k_a) times the applied current density, as shown in Equation 19. The specific area a of the DCBR reactor is defined as the reactive surface area of the electrodes dived by the reactor volume (a: specific surface area, m^{-1})

$$k_{obs} = \frac{1}{\frac{1}{k_f * a} + \frac{1}{k_{a*J}}} \tag{19}$$

The k_{obs} and J were fitted to Equation 19 to estimate $k_f \cdot a$ and Ka. The results shown in Table 5 tell that the mass transfer rate of PFOA was $0.123\ s^{-1}$ and $0.007\ s^{-1}$ for the flow through Ti_4O_7 wire mesh electrodes and BDD. The mass transfer rate of PFOA in wire mesh electrodes was about 15 times higher than that of flat plate BDD electrodes. Compared to the BDD, the flow velocity of the 3-layer Ti_4O_7 wire mesh is greater, while the Reynolds number of the wire mesh electrode is lower. Typically, a higher Reynolds number leads to a greater mass transfer rate; however, the Ti_4O_7 wire mesh electrode's porous structure enables it to achieve greater mass transfer.

Table 5 – The mass transfer coefficient of BDD and 3-layer Ti4O7 NTAs wire mesh.

Anode	Flow velocity	Re	Sc	k_f	k_f *a	a	K_a Superficial reaction rate constant
	m/s			$m·s^{-1}$	s^{-1}	m^{-1}	$cm^2·mA^{-1}s^{-1}$
3-layer Ti_4O_7 wire mesh	0.011	3.70	2293	4.67×10^{-5}	0.123	2633	0.055
BDD	0.002	11.09	2293	4.24×10^{-6}	0.007	1650	0.005

3.3.5   Energy recovery ratio of flow-through EAOP energy recovery system.

Due to the influence of the current density and other factors in the experiment, we only conducted the energy recovery experiment under 5V. The fuel cell was subjected to energy recovery experiments under oxygen and hydrogen conditions. As shown in Figure 17 below, the efficiency of the fuel cell in oxygen mode can be roughly increased by about 50%. The energy recovery ratio was estimated for the rest working potential. Since the oxidation of PFOA depends on direct oxidation, the lowest operating voltage we find in the literature is about 2.2 V. [36]. Therefore, we have simulated the range from 2 V to 5 V for energy recovery. The hydrogen-air mode is more practical for industrial applications, though its energy output is relatively low. We have considered an energy loss of 40 % for hydrogen-air mode. Moreover, the real energy recovery ratio in the 5V condition is also listed in Figure 18, and it shows the system can recover about 30% of the energy in the 2V mode, which would be a very significant saving for the system.
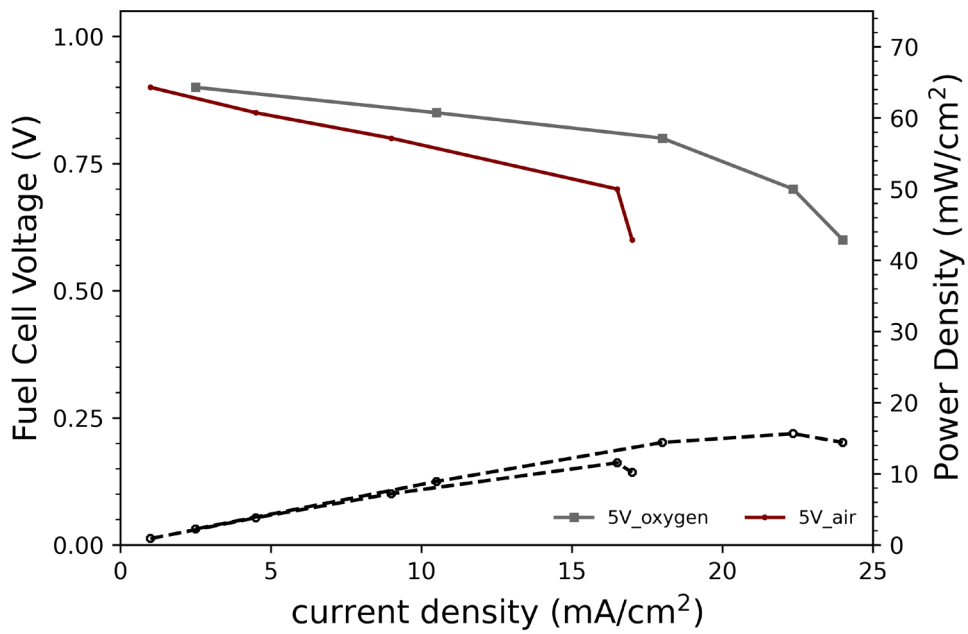
Figure 17 – The hydrogen fuel cell IV curve and the output power density in the 5V EAOPs operation condition
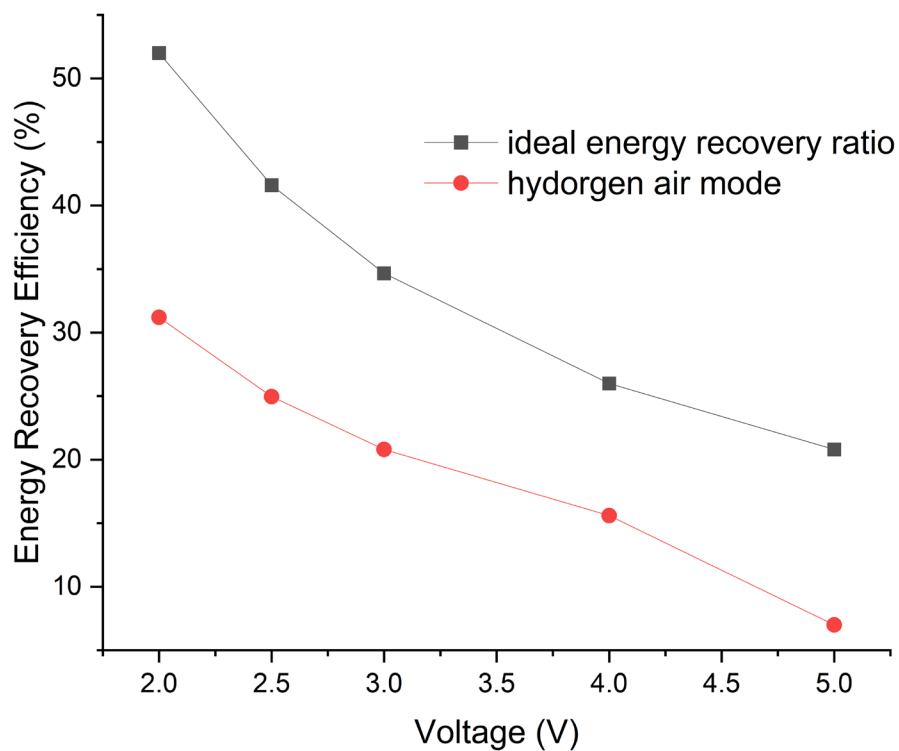
Figure 18 – The energy recovery ratio of the EAOP-fuel cell system in 2, 2.5, 3, 4, 4.5, and 5 V with the ideal energy recovery ratio and simulated H$_2$-air mode energy recovery ratio.

3.4   Conclusion

In the study, the flow through multiple layer wire mesh setup has been introduced to the EAOPs to achieve a higher oxidation efficiency by improving the mass transport. TiO_2 NTAs/SnO_2-Sb_2O_3 and Ti_4O_7 wire mesh were successfully fabricated, and both effectively degraded PFOA. When the number of electrode layers reaches three or more, it can achieve a highly efficient operating condition. We have successfully incorporated the flow-through setup into the EAOP-fuel cell energy system. This can have a combined effect of reducing energy consumption.

CHAPTER 4. INFLUENCE OF MNO$_X$ DOPING CONCENTRATION ON TIO$_2$ NANOTUBE ARRAYS ELECTROOXIDATION

4.1   Abstract

TiO$_2$ has demonstrated outstanding performance in electrochemical advanced oxidation processes (EAOPs) due to its structural stability and high oxygen overpotential. However, there is still much room for improvement in its electrochemical activity. Herein, narrow bandgap manganese oxide (MnO$_x$) was composited with TiO$_2$ nanotube arrays (TiO$_2$ NTAs) that in-situ oxidized on porous Ti sponge, forming the MnO$_x$-TiO$_2$ NTAs anode. X-ray absorption near-edge structure spectra (XANES) and X-ray Photoelectron Spectroscopy (XPS) analysis further proved that the composition of MnO$_x$ is Mn$_2$O$_3$. Electrochemical characterizations revealed that increasing the composited concentration of MnO$_x$ can increase the conductivity and reduce the oxygen evolution potential to improve the electrochemical activity of the composited MnO$_x$-TiO$_2$ NTAs anode.

Meanwhile, the optimal degradation rate of benzoic acid was achieved by using the MnO$_x$-TiO$_2$ NTAs with the MnO$_x$ concentration of 0.1 mM, and the role played by MnO$_x$ was also proposed based on the density functional theory calculation. Additionally, the required electrical energy (electrical efficiency per log order reduction, EE/O) to destroy BA was optimized by varying the composited concentration of MnO$_x$ and the degradation voltage. These quantitative results are of great significance for designing and applying high-performance materials for EAOPs.

4.2   Introduction

Electrochemical advanced oxidation processes (EAOPs) are environmentally friendly methods for oxidizing toxic organic compounds. The distinct advantages of EAOPs include: (1) they can generate sufficient HO• concentration that effectively oxidizes organic compounds, (2) they do not demand harsh reaction conditions nor any additional chemicals[17], and they cost low. Moreover, it is part of the trend towards the electrification of water treatment, paving a new way for developing decentralized and sustainable water treatment to create renewable power. However, unfortunately, its energy consumption is held back by various electrochemical properties of the anode materials, such as electrical conductivity and active sites in the valence band for hydroxyl radical generation on the valence band of electrode materials according to Equation 20:

$$h_{vb}^+ + H_2O = OH^* + H^+ \tag{20}$$

The standard redox potential of hydroxyl radicals is around 2.8 V, much higher than that of oxygen generation redox potential of 1.2 V. Therefore, a wide bandgap semiconductor as the electrode is required for producing hydroxyl radicals reducing oxygen production. However, large band gap semiconductors have low exciton carrier concentrations, which will hinder the solid/liquid interfacial charge transfer for electro oxidation[2, 63]. As a result, defect engineering by doping elements or building a heterojunction structure with narrow bandgap semiconductors can significantly increase the exciton concentrations of wide bandgap semiconductors [64, 65]. For example, the efficient boron-doped diamond (BDD) electrode is well designed using the doping technique [66]. After doping with boron, diamond, an insulator,

was transformed into a semiconductor. In terms of the heterojunction structure, for example, a Z-scheme structure can be formed by combining $BiVO_4$ with CdS, thus providing a higher quantum yield using a UV light for exciton generation [67, 68].

As one of the promising candidates for EOAPs, TiO_2 possesses excellent physical and chemical stability and a wide bandgap of 3.2 eV [35, 69]. It produces hydroxyl radicals by applying a voltage, but its electrical conductivity needs further improvement [70]. Defect engineering of TiO_2 has been achieved by using various dopants such as cobalt, niobium, and cerium [37, 71-74]. Compared to those transition element dopants, manganese oxides such as Mn_2O_3 and MnO_2 offer unique advantages, like being environmentally friendly and cost-effective and being narrow valence band semiconductors. Besides, previous studies showed that it could form the heterojunction structure by combining manganese oxide with TiO_2, efficiently reducing the recombination of electrons and holes [75-77]. Additionally, the electrical conductivity of MnO_x (~200 S m^{-1}) could also compensate for the low conductivity of TiO_2 (10^{-11} S m^{-1}) [78, 79]. Since the bandgap of MnO_2 and Mn_2O_3 are much lower than the band gap of TiO_2, it can be used to reduce the electrode's oxygen evolution potential (OEP) by compositing MnO_x in TiO_2. The optimized concentration of manganese dopants is also expected to balance the reaction rate (i.e., the rate of hydroxyl radical generation) and operating voltage [80]. Massa et al. reported that the TiO_2 NTAs deposited with MnO_x displayed higher phenol oxidation efficiency [81, 82]. However, the study of MnO_x-TiO_2 anodes is in the early stages of EAOPs applications [83] and is rarely reported in the literature.

In this study, the composited MnO_x-TiO_2 anodes were fabricated by in-situ growth of manganese oxide (MnO_x) onto TiO_2 nanotube arrays (MnO_x-TiO_2 NTAs), and the performance of the anodes was improved by using porous Ti substrates that allowed water to flow through them (i.e., flow-through operation). This allows for better mass transfer than a flat-plate anode, in which water flows over the anode. The benzoic acid (BA) was used as the target compound because it has a high rate constant with HO• [84]. The impact of MnO_x amount was investigated using a flow-through differential column batch reactor (DCBR), and its optimal composited amount was also studied. The influence of components on the anode performance is further analyzed, and the factors for performance improvement are investigated based on the band gap structure.

4.3   Materials and methods

4.3.1   Chemicals and materials

All chemicals are of analytical reagent grade or higher. 20 μm nominal pore size titanium foam, with a dimension of 20×30 mm^2 (normal to water flow) and a thickness of 1 mm, was purchased from the Northwest Institute for Non-ferrous Metals Research (Xi'an, China). The Ti foam has a purity of 99.5%. Tert-butanol (t-BuOH) and benzoic acid (BA, 95% purity) were purchased from Aladdin Biochemical Co., Ltd. (Shanghai, China). Ethylene glycol (EG), manganese (III) acetylacetonate, isopropyl alcohol, ammonium fluoride (NH$_4$F), and various electrolytes were obtained from Macklin Biochemical Co., Ltd. (Shanghai, China). All solutions were prepared with deionized water (Milli Q purification system, 18.2 MΩ.cm).

4.3.2   Preparation of the MnO$_x$-TiO$_2$ NTAs composited anode
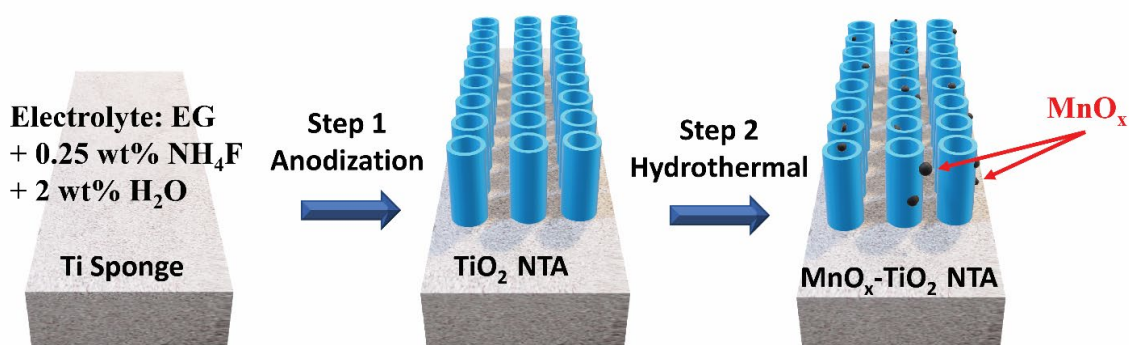
Figure 19 – Synthesis procedure of the MnO$_x$-TiO$_2$ NTA heterojunction porous anode: Step 1, anodic TiO$_2$ NTAs formation at 42 V. Step 2, deposition of MnO$_x$ by hydrothermal at 120ºC.

As shown in Figure 19, the MnOx-TiO$_2$ NTAs anode was prepared mainly through a two-step process: 1) Anodization of the Ti sponge substrate and 2) Hydrothermal deposition. The first step is to fabricate TiO$_2$ nanotube substrates by electrochemical anodic oxidation of porous Ti with 0.25 wt% NH$_4$F and 2 wt% H$_2$O in EG electrolyte at 42 V for 4 hours. The oxidized substrates are then cleaned with deionized water and ultrasound (25 W L^{-1} power, 40 kHz). The second step is preparing MnOx-TiO$_2$ NTAs by a hydrothermal method. Firstly, 60 mL of deionized water and 20 mL of isopropanol were mixed thoroughly. Secondly, manganese (III) acetylacetonate was dissolved into the precursor to give solutions of 0.1, 0.5, 1, and 5 mM. Thirdly, the TiO2 NTAs anode was autoclaved with the precursor solutions in a 125 mL Teflon-lined hydrothermal vessel (Parr Instrument Company, USA) at 120°C for 2 hours.

4.3.3   Characterization of MnO$_x$-TiO$_2$ NTAs composited anode

The surface morphology of the anode was observed by field emission scanning electron microscopy (FE-SEM, JEOL, JSM-6701F) and transmission electron microscopy (TEM, JEM-

2100F). The valence state of MnO_x was measured using X-ray photoelectron spectroscopy (XPS) (a Kratos AXISUlTRA-DLD spectrometer using an Al K_α source). Furthermore, the Mn K-edge X-ray absorption near edge structure (XANES) data was collected at BL_1W_1B station in Beijing Synchrotron Radiation Facility (BSRF, operated at 2.5 GeV with a maximum current of 250 mA). The detailed setup for XANES is given in Supplementary Material (Text S1). X-ray diffraction (XRD, X'PERT PRO MPD diffractometer, Cu K_α radiation, $\lambda=0.154$ nm, scan range of 10-90°) was used to identify the crystal structure of the TiO_2 NTAs-based anodes. A mercury intrusion porosimeter (Auto pore V9600, Micromeritics) was used to assess the porous features of the electrodes.

4.3.3.1 Electrochemical measurements

Linear sweep voltammetry (LSV) was carried out on the CH I 660D electrochemical workstation using a standard three-electrode configuration with a saturated calomel electrode (SCE) as the reference and platinum sheet as the counter electrode. The anodic scan rate of the electrode was 10 mV/s. Electrochemical impedance spectroscopy (EIS) was carried out on an electrochemical workstation (PARSTAT 3000A-DX), and the same setup was used for the LSV test.

4.3.3.2 Electrochemical measurements

The flow-through reactor was equipped with a reservoir, and a differential column batch reactor (DCBR) system is shown in Appendix. (We call it a DCBR because the influent concentration is equal to the effluent concentration, and it stimulates the performance of a plug flow reactor.) The flow-through reactor comprises a porous MnO_x -TiO_2 NTAs anode and a

56

stainless-steel cathode with a 0.2 cm electrode spacing. BA is selected as the molecular probe given its stable structure and relatively high second-order rate constant (5.9×10^9 M^{-1} s^{-1}) with •OH. 0.05 M or 0.1 M Na$_2$SO$_4$ is used as a supporting electrolyte. Radical quenching reactions were designed to evaluate the impact of radical species on BA destruction. These were performed using the same DCBR, but the electrolyte was changed to 0.05 M Na$_2$SO$_4$, and 100 mM t-BtOH was used as a quenching agent.

4.4. Results and discussion

4.4.1 *Material characterization*

The morphology and composition of bare TiO$_2$ NTAs and composited MnO$_x$-TiO$_2$ NTAs were investigated by SEM and TEM-EDS analysis, respectively. Based on the manganese precursor concentrations of 0.1 mM, 0.5 mM, 1 mM, and 5 mM, the electrodes are named 0.1_MnO$_x$-TiO$_2$ NTAs, 0.5_MnO$_x$-TiO$_2$ NTAs, 1_MnO$_x$-TiO$_2$ NTAs, and 5_MnO$_x$-TiO$_2$ NTAs, respectively. The Mn/Ti ratio of MnO$_x$-TiO$_2$ NTAs was characterized by ICP-OES, showing ratios of Mn/Ti ranging from 0.039 % to 1.38%, with precursor solutions ranging from 0.1 to 5 mM (see Appendix1).

Figure 20. displays that the uniform TiO$_2$ NTAs were formed on the Ti substrate, but the orientation of the TiO$_2$ nanotubes varied. This is mainly attributed to the high surface roughness of the porous Ti sponge, which varies the growth direction of the TiO$_2$ NTAs. A Hg porosimeter characterized the porous structure of the electrodes, and the results are shown in Appendix. Ti sponge has a porosity of 45% and a median pore diameter of 20 μm. After anodization, the differential pore volume is increased in the pore diameter range of 0.01 to 1

57

μm. Following the composite of MnO$_x$, the cumulative pore area decreases slightly. The XRD results in Appendix show that TiO$_2$ is formed after calcination. However, there is no obvious signal of MnO$_x$ using XRD as the amount of MnO$_x$ is too little. The structure and morphology of MnO$_x$-TiO$_2$ NTAs were then characterized by EDS and HRTEM, respectively. Figure 20. b-c show two different lattice spacings of 0.25 and 0.35 nm, which correspond to the lattice planes of Mn$_2$O$_3$ (110) and TiO$_2$ (101), respectively. The composite structure is formed between the Mn$_2$O$_3$ and TiO$_2$ NTAs. Figure 20.d is the sample of 0.1_MnO$_x$-TiO$_2$ NTAs stripped from the Ti base. The EDS elemental mapping of MnO$_x$-TiO$_2$ NTAs (Figure 20. e-g) shows the distribution of manganese throughout the TiO$_2$-rich particles, suggesting that hydrothermal treatment generates uniformly distributed MnO$_x$-TiO$_2$ NTAs.

As shown in Figure 20. h-k, high-resolution XPS spectra of Ti_2p, O_1s, Mn_2p, and Mn_3s were carried out to investigate the surface chemical conditions of the composited MnO$_x$-TiO$_2$ NTAs electrode. In our MnO$_X$-TiO$_2$ NTAs samples, the binding energy of Mn_2p is 642.2 eV, and the Mn_2p binding energies are almost identical for different valences of manganese. Therefore, the Mn 3s binding energy was used to detect the valance state of MnO$_x$ [85]. According to the literature[86, 87], the Mn_3s multiplet splitting energies of MnO (Mn^{2+}), Mn$_2$O$_3$ (Mn^{3+}), and MnO$_2$ (Mn^{4+}) are 5.9, 5.3, and 4.7 eV, respectively. Here the multiplet splitting energy of Mn 3s is 5.43 eV. Therefore, it can be determined that Mn$_2$O$_3$ (Mn^{3+}) is the major component of the MnO$_x$ -TiO$_2$ NTAs anode. Further, XANES spectra of the 0.1_MnO$_x$-TiO$_2$ NTAs were performed using Mn metal, MnO, and MnO$_2$ (see Appendix). It can be observed that the absorption edge of 0.1_MnO$_X$-TiO$_2$ NTAs lies between MnO and MnO$_2$, which confirms that the valence state of the Mn in MnO$_x$ is located between 2$^+$ and 4$^+$.

Therefore, Mn_2O_3 is formed on the TiO_2 NTAs as a result of the self-decomposition of manganese oxide at 500 °C, as described in the equation[88]:

$$4MnO_2 \rightarrow 2Mn_2O_3 + O_2 \qquad (21)$$
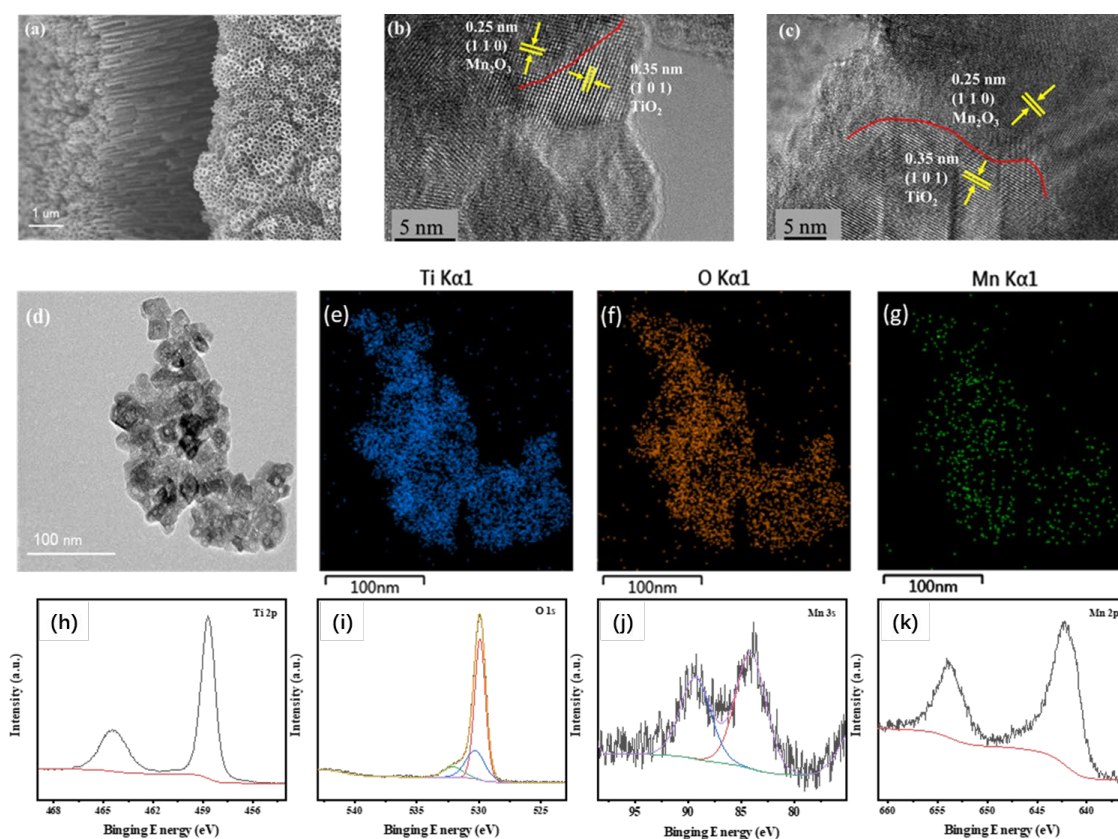
Figure 20 – SEM image of bare TiO_2 NTAs (a), HRTEM images of 0.1_MnO_x-TiO_2 NTAs (b-c), STEM of 0.1_MnO_x-TiO_2 NTAs (d), elemental images from TEM-EDS proves that Mn is uniformly distributed through the whole plate. TiO_2 NTAs also uniformly grow on the Ti substrate(e-g), and high-resolution XPS spectra of Ti_2p, O_1s, Mn_3s, and Mn_2p of MnO_x-TiO_2 NTAs (h-k).

4.4.2   Electrochemical properties of the anode

In Figure 21. a the OEPs (oxygen evolution potential) for 0.1_MnO_x-TiO_2, 0.5_MnO_x-TiO_2, and bare TiO_2 NTAs are all approximately 3.1 V, while those for 1_MnO_x-TiO_2 and 5_MnO_x-TiO_2 NTAs are 3.0 and 2.9 V, respectively. For convenient comparison, the potentials

here have been converted to vs. RHE based on the pH of the systems. In the MnO_x-TiO_2 NTAs system reported in the literature[82], the OEPs decreased with increasing the amount of manganese oxide. Although the OEPs for 0.1 mM and 0.5 mM MnO_x-TiO_2 NTAs are almost identical, the slope of the *I-V* curve increases with increasing composited concentration, indicating enhanced electrooxidation activity. As shown in Figure 21. b, the EIS measurement determines the charge transfer properties of the anode [89, 90]. It can be observed that the EIS plots of the bare TiO_2 NTAs and 0.1_MnO_x-TiO_2 NTAs show significant semicircle regions, meaning the charge transfer resistance (R_{ct}) at the interface of the two electrodes is large, while the straight lines suggest a better mass transfer property of the 0.1_MnO_x-TiO_2 NTAs. Moreover, the R_{ct} of the MnO_x-TiO_2 NTAs decreases with the increment of composited MnO_x concentration. When the concentration of MnO_x in the MnO_x-TiO_2 NTAs electrode reaches 5mM, although its R_{ct} is reduced, the mass transfer is poor. Therefore, it can be deduced that only a small amount of MnOx benefits EAOPs. The Mott-Schottky plots depict the flat band position of MnOx-TiO2 NTAs (Figure 21. c). The positive slope of the Mott-Schottky plots indicates that all samples are n-type semiconductors, as oxygen vacancies serve as the main electron carriers in TiO_2 [91]. The flat band potential (E_{fb}) is determined by taking the x-intercept of $1/C^2$ as a function of applied potential E. It is clear that the bare TiO_2 NTAs possess the smallest negative E_{fb}. As the MnO_x concentration increases, the E_{fb} of the sample becomes more negative. For Mn_2O_3, the E_{fb} was reported to be around 1.4 V vs. (Ag/AgCl) [92]. It also confirms that the deposition of Mn_2O_3 increases with the increment of Mn impregnation.
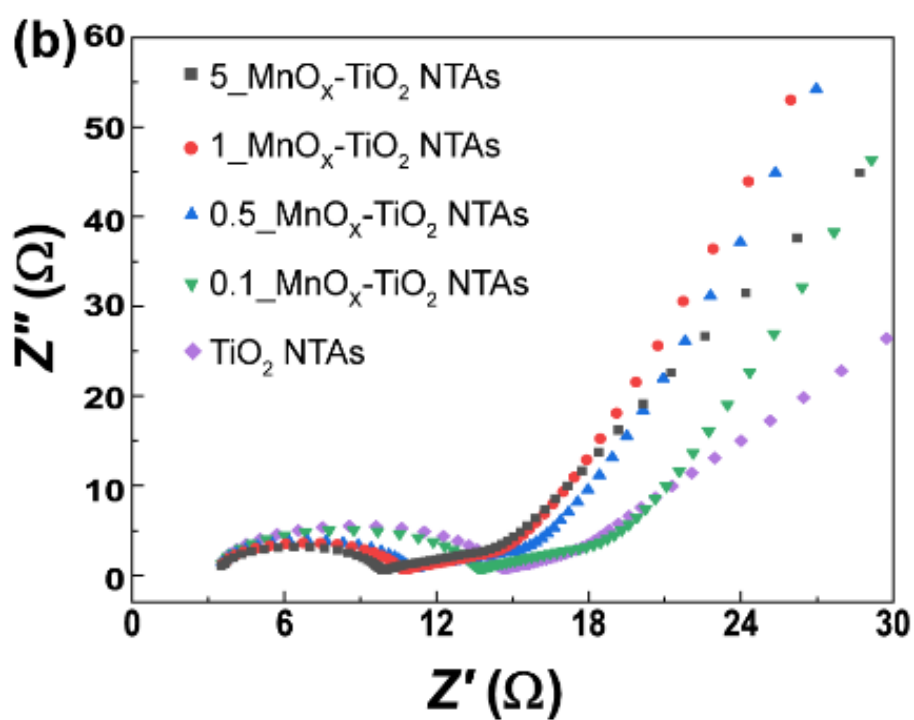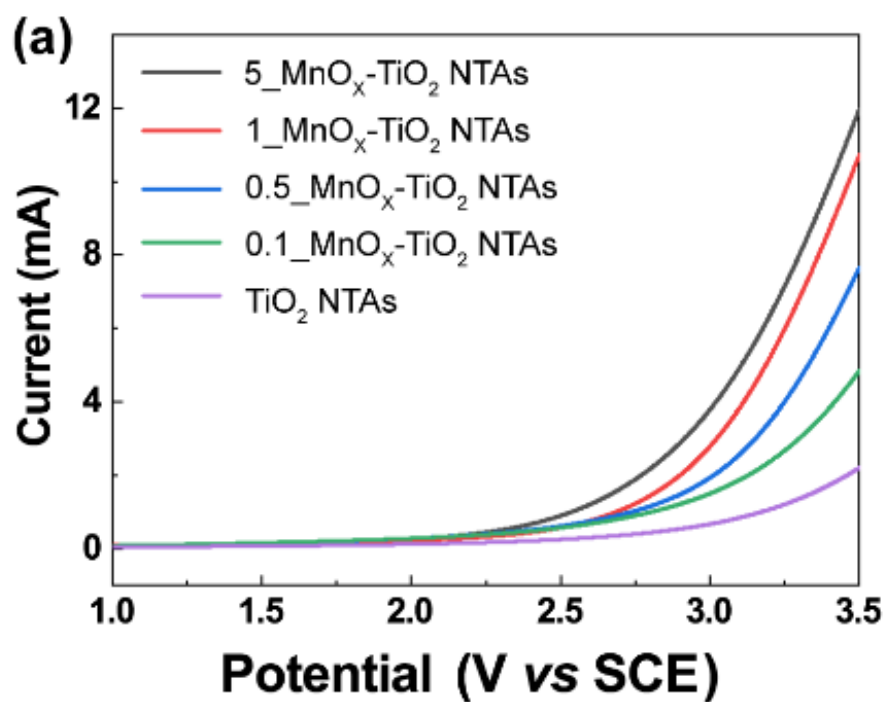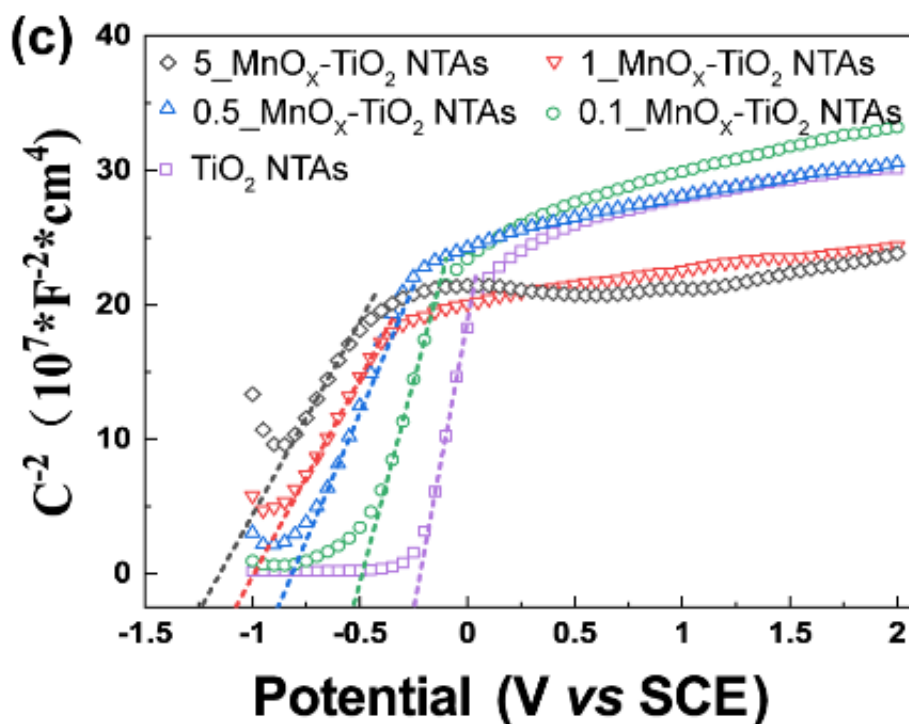
Figure 21 – The LSV of the anodes (a), EIS of the anodes tested at open circuit potential (b), and Mott-Shockey plot of the anodes (c). The electrode spacing is 1 cm with Pt as the counter electrode and a saturated calomel electrode (SCE) as the reference electrode. The supporting electrolyte is 0.05 M Na_2SO_4.

4.4.3 Electrochemical oxidation experiments

Benzoic acid (BA) was used as the target compound to be oxidatively degraded on the prepared MnO_x-TiO_2 NTAs anode. Figure 22. depicts the degradation efficiency (C/C_0) of BA versus electrolysis time at constant current density. It is shown that the C/C_0 of 0.1_MnO_x-TiO_2 NTAs displays the greatest degradation rate. As the amount of MnO_x deposition increases, the rate of BA destruction decreases, and the reaction rate for 5_MnO_x-TiO_2 NTAs is the smallest of all samples. The figure in the Appendix shows that BA degradation follows a pseudo-first-order model. The rate constant of 1_MnO_x-TiO_2 NTAs is close to that of bare TiO_2 NTAs. However, the operating voltage of 1_MnO_x-TiO_2 NTAs is lower at the same current
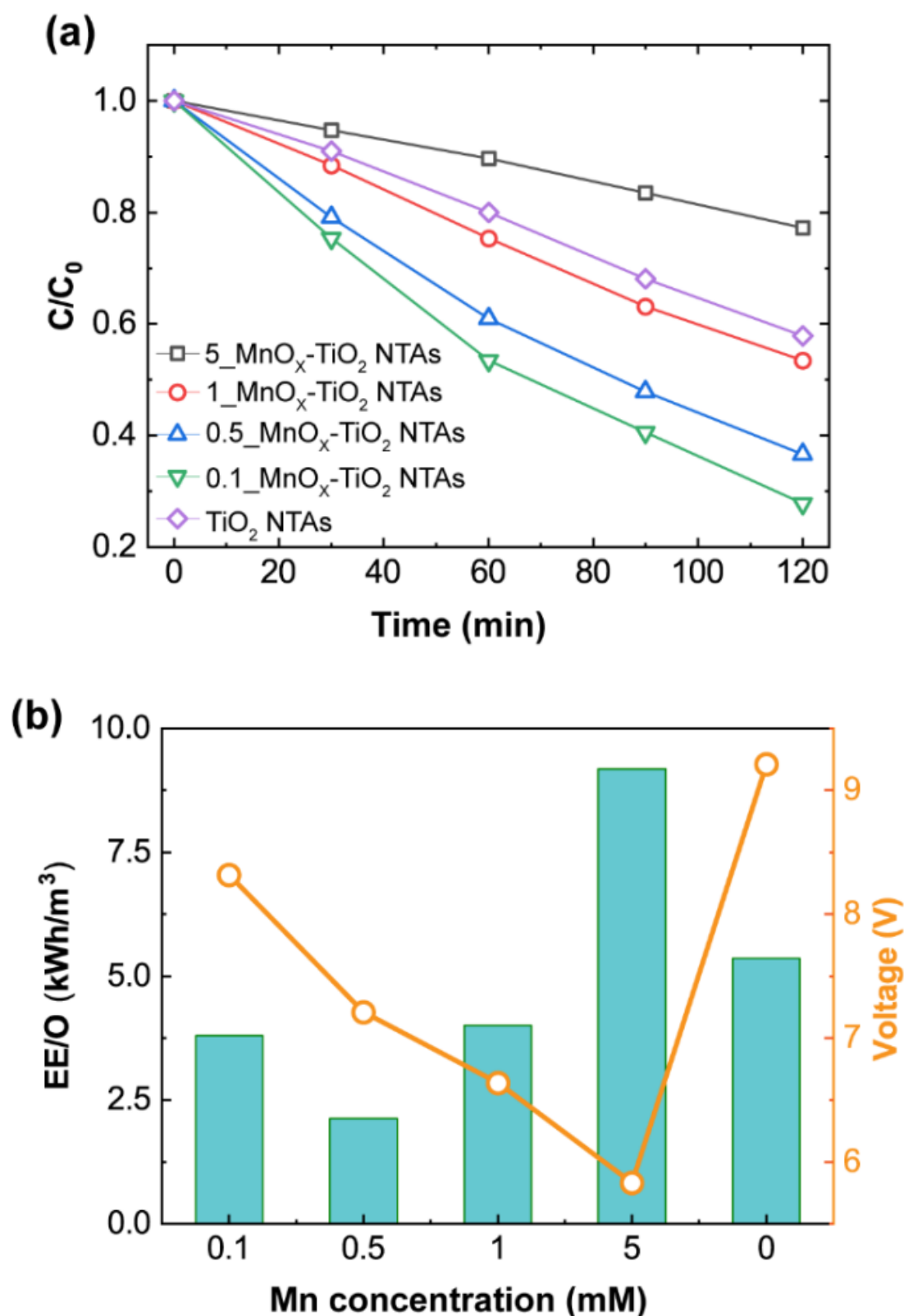
Figure 22 – (a) Effect of Mn doping concentration on BA degradation (Supporting electrolyte: 0.05 M NaSO4, BA concentration: 20 ppm (b). The EE/O of the flow-through DCBR reactor. Supporting electrolyte: 0.05 M NaSO4, BA concentration: 20 ppm. Flow velocity: 0.08 cm s-1, nominal pore size= 50 um, volume =100 mL

density condition, as demonstrated in the previous LSV and EIS measurements. Since BA

destruction follows a pseudo-first-order reaction, the electrical efficiency per log order reduction (EE/O)[93] can be used to determine the efficiency of the various anodes and can be calculated using Equation 4 below.

Figure 4a depicts the C/Co of BA versus electrolysis time for a constant current density. The C/Co of 0.1 mM MnO_x-TiO_2 NTAs has the greatest degradation rate. As the Mn deposition increases, the destruction rate of BA decreases, and the reaction rate for 5 mM MnO_x-TiO_2 NTAs is the smallest, including bare TiO_2 NTAs. The figure in the Appendix shows that the BA degradation followed a pseudo-first-order model. The rate constant of 1 mM MnO_x-TiO_2 NTAs is close to the bare TiO_2 NTA. However, the 1 mM MnO_x TiO_2 NTAs have a lower operating voltage for the same current density condition, which was already proved in our LSV and EIS measurements.

As illustrated in Figure 4b, 1 mM MnO_x-TiO_2 NTAs have a much greater energy efficiency than bare TiO_2 NTAs when the operating voltage is considered. As the Mn concentration increases, the applied voltage U lowers. When both voltage and reaction rate are considered, the 0.5 mM MnOx TiO2 NTAs have the highest overall EE/O, despite the fact that the 0.1 mM electrode has the highest reaction rate.

4.4.4   Direct and indirect BA degradation Rates

For EAOP, direct oxidation on the electrode and indirect hydroxyl radical oxidation (produced by the reactions between the valence band holes and water) are the two reaction pathways. HO• radicals' generation is considered the main oxidation pathway, and its reaction can be quantified by quenching it using t-BtOH because it selectively reacts with •OH. Figure

5a displays the percentage of BA oxidation after two hours. The direct and indirect percentage is estimated based on the relation below:

$$\eta_{dir} = \frac{C_{t-BuOh} - C_0}{C - C_0} = 1 - \eta_{indir} \tag{22}$$

As can be noted from Figure 5b, 0.1_MnOx-TiO2 NTAs and bare TiO2 NTAs have similar percentages of indirect oxidation, while the 5_MnOx-TiO2 NTAs have a lower indirect oxidation percentage. These results explain the drop in the reaction rate constant for the highly impregnated 5_MnOx-TiO2 NTAs. The manganese oxide lowers the OEP and thus the generation of radicals, but at the same time, the electric conductivity of the electrode increases.
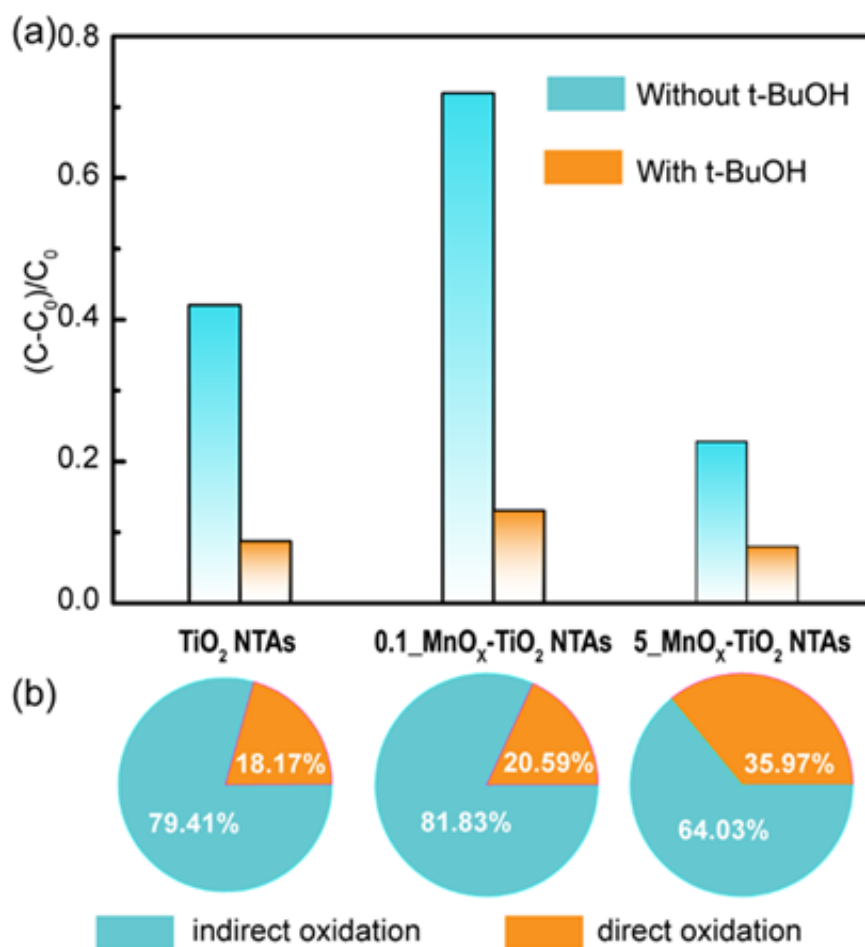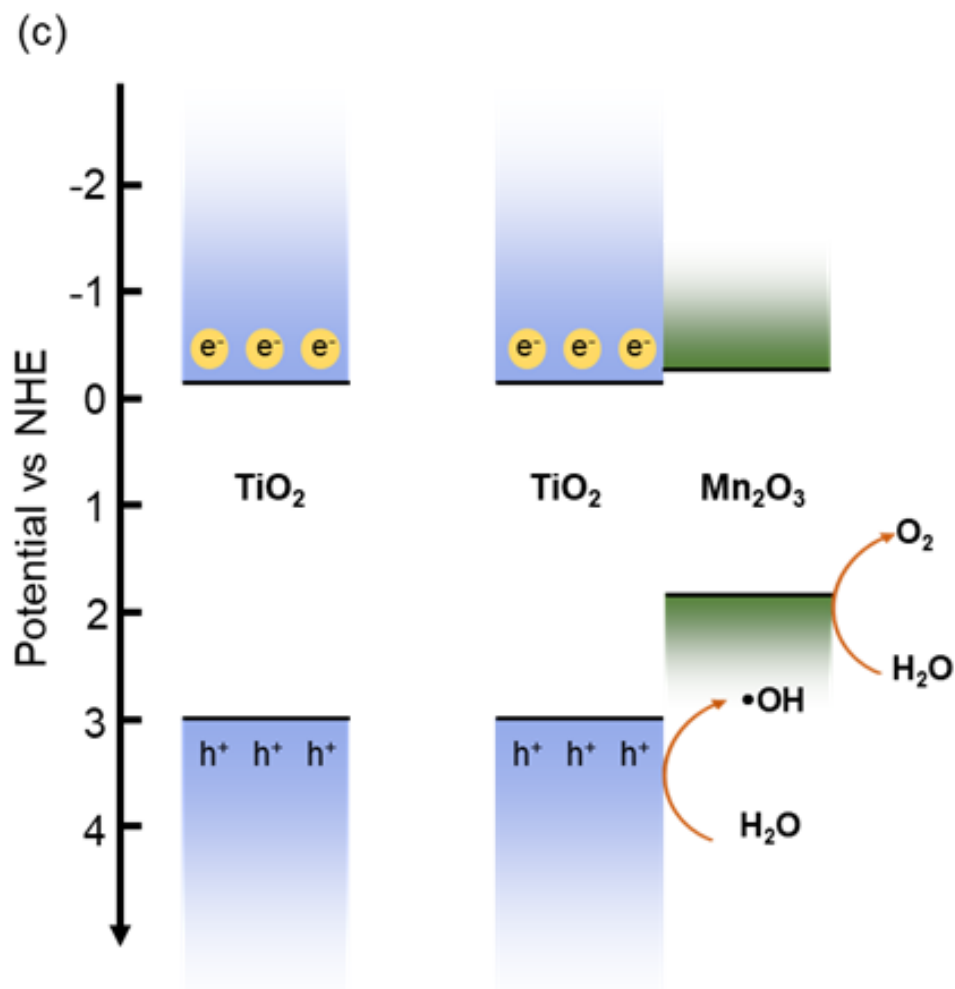
Figure 23 – C/C₀ of BA degradation before and after applying 0.1 M t-BuOH after 2 hours of reaction time (a), the percentage of direct and indirect oxidation (b), the schematic bandgap structure of TiO_2, and TiO_2-Mn_2O_3 heterojunction structure(c). Supporting electrolyte: 0.05 M Na_2SO_4, BA concentration: 20 ppm, flow velocity: 0.08 cm s^{-1}, nominal Ti sponge pore size: 50 um, volume:100 mL.

We also used DFT calculations to measure the electronic structures of TiO_2 and Mn_2O_3 (see Supplementary Material Text S2 for details of the calculations), which shows that the band gap for TiO_2 is 2.33 eV, while that for Mn_2O_3 is 0.27 eV (Appendix). It should be noted that the calculated band gap is smaller than the experiment due to the use of the PBE functional form. However, the band gap order from the DFT calculation is consistent with the experimental value. That is to say, the electronic conductivity of Mn_2O_3 is far better than that

for TiO$_2$, which agrees well with the above experiment results on the electrical resistance of MnO$_x$-TiO$_2$ NTAs. Furthermore, we proposed an enhanced mechanism of the water decomposition reaction of the TiO$_2$/Mn$_2$O$_3$ composite (Figure 23. c). Because Mn$_2$O$_3$ possesses more electrons near the Fermi energy level, the Mn$_2$O$_3$ can directly promote the transformation from water to oxygen. However, TiO$_2$ can only promote the transformation from water to oxyhydrogen radical. As a result, the valence band of Mn$_2$O$_3$ has a more significant effect on oxidation when we increase the concentration of Mn$_2$O$_3$, thus reducing the oxidation rate of BA. Hence, the TiO$_2$/Mn$_2$O$_3$ composite anode should be a better choice for enhancing the water decomposition reaction.

4.5 Conclusions

The composited anode of MnO$_x$ with porous TiO$_2$ NTAs was fabricated, demonstrating better electrochemical oxidation performance towards BA degradation. From LSV, EIS, and Mott-Schottky analyses, the presence of MnO$_x$ on TiO$_2$ NTAs greatly reduces the working potential of the anode during electrooxidation. This result confirmed the vital role of MnO$_x$ in enhancing the charge transfer properties. Besides, MnO$_x$ overlaps the conduction band region of TiO$_2$ and lowers the valence band position of TiO$_2$, thus reducing the combination of charges and promoting the production of HO•. On the one hand, as more MnO$_x$ is impregnated into the TiO$_2$ NTAs, the hole at the valence band possesses a lower reduction potential, and as a result, fewer HO• is produced, leading to a lower BA oxidation rate as well.

On the other hand, as more MnO$_x$ is impregnated into the TiO$_2$ NTAs, the higher the conductivity of the anode, which may increase the oxidation rate of BA. Therefore, an

optimized composite concentration is expected in the low deposition region. Finally, crucial factors, including current density, voltage, and reaction rate of BA degradation using the DCBR, are obtained and used to estimate the performance of EAOPs.

CHAPTER 5. PULSE POTENTIAL EAOPS FOR BA OXIDATION

5.1   Abstract

The pulse potential EAOPs (electrochemical advanced oxidation processes) are conducted for benzoic acid oxidation. The pulse potential EAOPs save more energy than the traditional DC EAOP. The pulse potential and on/off voltage frequency were investigated in terms of oxidation efficiency. The study obtained optimal conditions to achieve high organic removal and low energy consumption.

5.2   Introduction

Electrochemical advanced oxidation processes (EAOPs) have emerged as a viable method for water treatment due to their high voltage efficiency, no chemical additive, and ease of control. The EAOPs utilize anodic direct and indirect oxidation for organic removal. Direct oxidation is the oxidation process by the hole excited on the anode surface, and indirect oxidation is the oxidation process by hydroxyl radical • OH, which is generated by the reaction of a surface hole and water molecular. The radical lifetime is 10^{-9} s. Their diffusion distance is restricted to the electrode surface. Therefore, EAOPs are a heterogeneous reaction. Accordingly, the practical application for industrial wastewater treatment faces obstacles, including side reaction (oxygen evolution) and low oxidation rate due to mass transfer limitation of organic to the electrode surface. This is notably true for conventional direct current (DC) electrolysis conditions. The term 'limiting current density' has been used in DC

electrooxidation to refer to the maximum current density for organic removal prior to the mass transfer limitation.

Pulsed electrolysis has been the subject of research for several decades. During the electrolysis, the pulsed voltage mode changes the voltage from a base value (known as off-voltage) to a peak value (called on-voltage). The pulse period is the sum of on-time (ton) and off-time (toff). EAOPs are an application of electrolysis. Therefore, the pulsed electrolysis methods are also applicable to EAOPs. In DC mode, the current is all faradic current which refers to electron transfer caused by oxidation or reduction. In pulse potential mode, the current i_p consists of two parts: non-faradic current i_C (which charges the double layer) and a faradaic current i_f. The non-faradic current (Equation 23) could be approximated as the charge/discharge of an ideal polarized electrode when a voltage pulse is applied:

$$i_c(t) = \frac{\Delta E}{R_s} e^{-\frac{t}{R_s C_d}} \qquad (23)$$

with ΔE the amplitude of the voltage pulse, Rs the solution resistance, C_D the double layer capacitance, and t is the ton/off time.

Based on Equation 23, the non-Faraday current i_c will be influenced by the voltage pulse's amplitude and on/off time (t). Therefore, the choice of frequency is crucial to pulse potential EAOPs. In addition, the previous experimental results also show that pulse frequency affects the following distinct processes: bubble removal, diffusion layer formation, and electrical double layer (EDL) formation.

The diffusion layer formation time (Equation 24) is the time for the reactant concentration at the electrode surface to fall to zero:[94]

$$\tau = \frac{D(C_o nF)^2}{2i^2} \tag{24}$$

The frequency range study of the diffusion layer formation is usually in 1-1000 Hz.[95]

The electric double layer formation time (Equation 25): [96]

$$t = \frac{1}{4D_o}(\frac{X_{ad}}{X})^2 = \frac{\delta_{max}^2}{4D_o} \tag{25}$$

where D_o: the diffusion coefficient, X_{ad}: the density of hydrogen ions on the cathode (cm), X: the concentration of hydrogen ions in bulk, and δ: the thickness of the diffusion layer. The electric double layer formation in the microsecond level, thus the pulse range above 100 kHz, is required to study EDL.

The bubble removal:

It has previously been observed that bubble coverage reduces conductivity and increases ohmic losses of electrolysis. The increment of electrolysis energy efficiency is reported in the 10- 100 Hz frequency range due to the bubble removal. Researchers found a reduction in the thickness of the gas diffusion layer and a quicker bubble rise from the electrode's surface [97]. The previous work of Pospisil shows that the pulses in the range of 40–240 Hz positively impact electrolysis, which would be caused by the removal of bubbles on the electrode surface.[98]

71

A literature search revealed only a few studies about EAOPs using pulsed potential/current mode. In the work of Wei et al. [93, 94], the electrochemical oxidation of phenol using pulsed BDD electrodes was studied. Their results reveal that the pulse frequency (10–500 Hz) and the square pulse's duty cycle significantly influence the degradation of phenol. Robert showed that the oxidation efficiency of pulse potential is greater than that of the DC mode in the 1-5 Hz range. He reported that the BDD's double layer capacity is 81 μFcm^{-2}.[99] In contrast, the standard metal or graphite (considered surface roughness) is around 1- 20 μFcm^{-2} in aqueous.[100, 101] BDD's relatively larger double layer capacity should be noticed because it is closely related to non-faradic current density. The published pulsed potential/current EAOPs mainly discuss the frequency and on-voltage effect. There is little published data on the off-voltage effect. Previous research in pulse water electrolysis suggests that the greater the off-voltage, the lower the on-time current. In the meantime, the hydrogen generation rate is enhanced by increasing the base voltage.[97] A possible explanation for this might be that a portion of the measured on-current was non-faradic capacitive charging. If so, an off-time discharge would be recorded. The evidence from this study suggests that the change of off-voltage should affect pulse potential EAOPs. Because a wideband semiconductor like BDD is used in the experiment for radical generation, its double layer capacity is much larger than the metal anode for water electrolysis.

In this study, a pulse potential EAOPs was conducted to degrade the benzoic acid wastewater using BDD as the anode. This work aimed to investigate the influence of the off-voltage and frequency during electro oxidation. A comparison between the constant and pulse voltage EAOPs was made to

evaluate the performance. The LSV and Electrochemical Impedance Spectroscopy (EIS) analyses were conducted to optimize the pulse potential condition.

5.3   Materials and methods

Pulsed potential supply:

Instead of using an electrochemical workstation or an expensive computer-based controller, the Low-cost TTL (Transistor-Transistor Logic) and CMOS (Complementary Metal Oxide Semiconductor) analogy switches were used as PWM (Pulse Width Modulation) for the control of the on/off voltage, pulse voltage frequency, and duty cycle.

In our experiment, the duty cycle is 50 %, and the on-voltage is 4V as default. The pulse amplitude is varied for investigation. The frequency is in the range of 10-1000 Hz. The duty cycle is the ratio between on-time and pulse period, while the frequency is the inverse of the pulse period. The difference between the on-voltage and off-voltage is the pulse amplitude illustrated in Figure. For example, in 4V on-voltage and 1 V off-voltage conditions, the pulse amplitude is 3V.
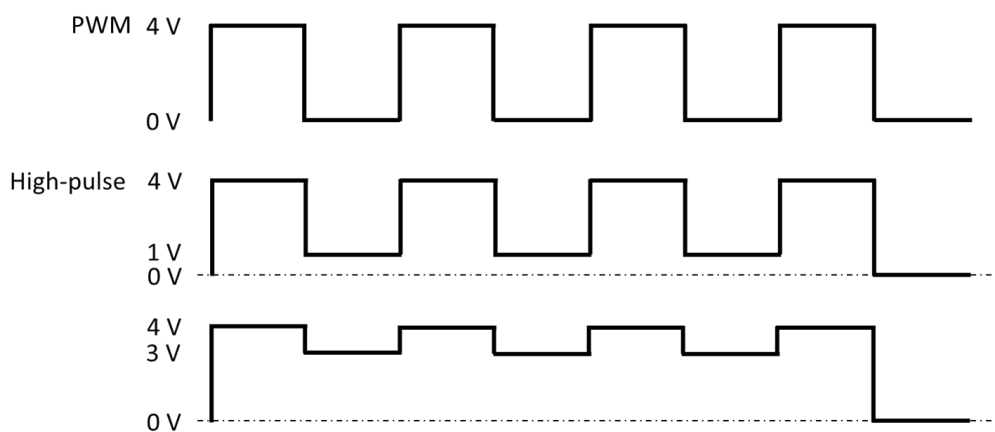
Figure 24 – An example of an ideal PWM on/off voltage profile of 4-0 V,4-1 V, and 4-3 mode.

UV-vis analysis:

The determination of the BA concentration within the degradation experiments was carried out using UV-Vis (Hitachi, UH5700)

Electrochemical characterization:

The electrochemical characterization was performed in a three-electrode setup. A silver/silver chloride electrode was used as a reference electrode.

Electrochemical degradation experiments

The degradation experiments of BA were performed in a two-electrode setup with 0.1 M Na_2SO_4 solution.

5.3   Results and discussion

a)

b)

c)

$$Z_{Im}$$

$$\omega = 1/R_{ct}C_d$$

$$\omega \qquad \qquad \omega$$

$$\infty \qquad \qquad 0$$

$$R_\Omega \qquad \qquad R_\Omega + R_{ct} \qquad Z_{Re}$$

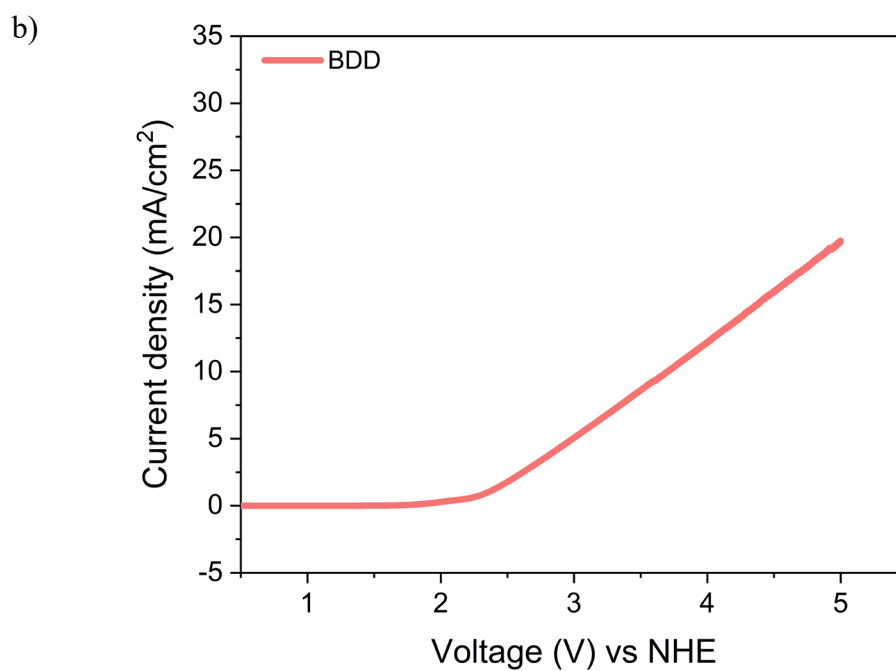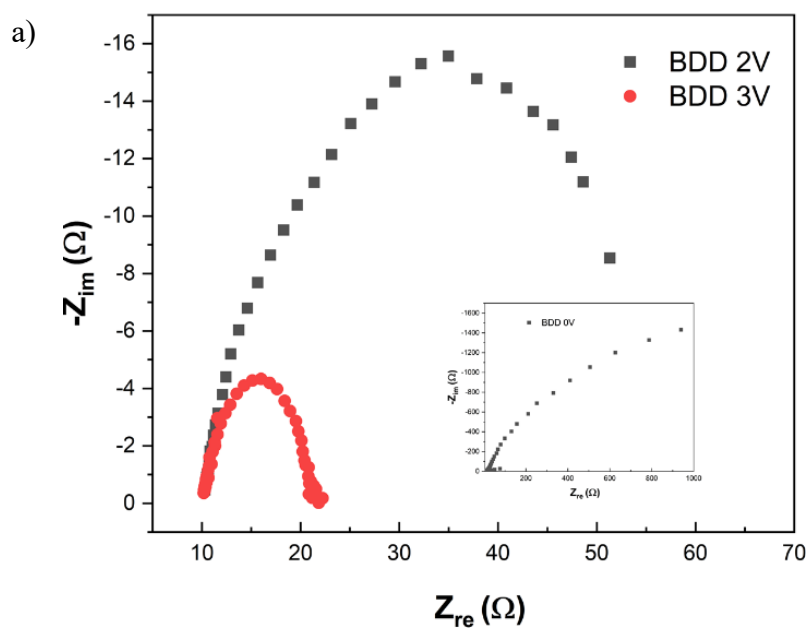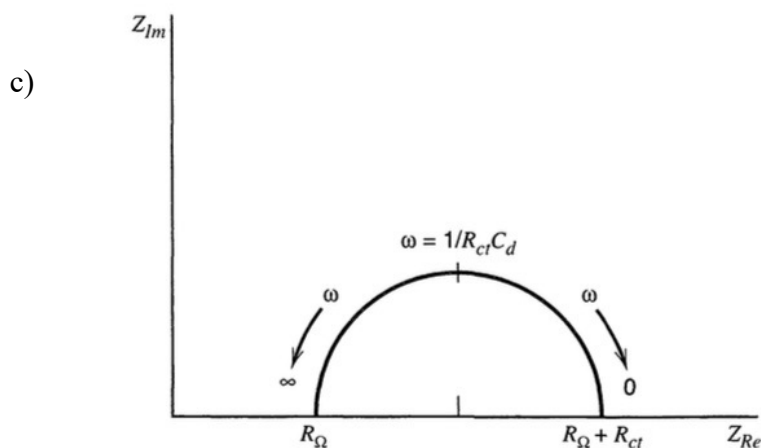**Figure 25 – a) The EIS of BDD with different biased potentials (2V and 3V vs NHE), Subplot: the EIS of BDD at 0 V vs NHE. b) The LSV plot of BDD. Both a) and b) are tested in 0.1 M Na₂SO₄ with 1 cm electrode spacing. c) the ideal plot of the relationship between the frequency and the electron transfer resistance (Z_f) and the capacitance (C_d).**

The applied voltage strongly affects the electrochemical activity of the BDD anode. The Nyquist plot of the BDD is shown in Figure 25. a. With increased biased potential applied to the BDD, the impedance of the BDD drops rapidly, which is especially obvious when the applied voltage increases from 2 to 3 V. The BDD as a wide semiconductor is non-conducting with applied voltage below the OEP and has a very small current density. The BDD's LSV plot (Figure 25. b) is around 2.2 V/NHE. When the applied voltage is higher than the OEP, the BDD becomes a conductor with much smaller electron transfer resistance (Z_f) and surface capacitance (C_d) for electron oxidation. Therefore, the on-voltage should be at least beyond 2.2V for effective oxidation. The off-voltage should be lower than 3 V to avoid oxidation in the off-time. Except for suggesting the operational off-voltage condition, the interpretation of the EIS of BDD and ideal EIS plot (Figure 25. c) can help understand the optimal frequency for pulse potential EAOPs. The characteristic frequency ω is directly obtained by reading the

highest point of the EIS circle. In 2 V biased potential conditions, the characteristics frequency ω is 50 Hz. It indicates that the non-faradic process outweighs the faradic process if the applied frequency is much higher than 50 Hz. The capacitance is dramatically smaller in the 3 V biased potential condition. Its corresponding ω is 400 Hz. It is hard to directly read the ω of BDD in the open circuit condition (OCP), because there is no circle formed in that situation. We still can reasonably extrapolate the frequency, which should be much lower than 50 Hz. Therefore, the current may barely charge and discharge the electron double layer (Cd) in high frequency and low off-voltage conditions. Therefore, pulse potential EAOPs should adjust the off voltage based on the applied frequency. The pulse potential EAOPs are compared with the constant DC EAOPs in the following BA oxidation experiments.

Table 6 tells that the Power density of high-frequency pulse EAOP is higher than the 50 % power density of the DC mode in the 50% duty cycle condition. The power density P is calculated based on Equation 26:

$$P = \frac{\int U \cdot |I| \, dt}{t} \tag{26}$$

The reasons for higher than 50 % power density are: 1) In the off-voltage state, there is still current. 2) In the on-voltage state, the pulse potential EAOPs have a higher current density than the constant DC EAOP. Table 7 shows the EE/O of the BA oxidation in different on/off voltage and frequency conditions. It is apparent from the table that when the applied frequency is beyond 100 Hz, the EE/O of pulse potential EAOPs are higher than that of the DC EAOPs. This is inconsistent with our previous discussion. The non-faradic process gradually dominates

the process with a higher frequency applied. When the frequency is beyond 1 kHz, almost no

BA oxidation occurs in 4-1 V and 4-2 V mode, which can therefore be another strong evidence

of a non-faradic process, instead of faradic process which dominates the current. Another

important finding was a positive shift of optimal frequency with increased off-voltage. In 4-0

V mode, 10 Hz is the best frequency compared to others. In 4-1 V, both 50 and 10 Hz has lower

EE/O than the DC EAOP. In 4-2 V, the lowest EE/O is obtained at 50 Hz. This also accords

with our earlier observations, which showed increased ω for increased biased potential.

Table 6 – The power density of the EAOPs with different voltage and frequency. Note: 4-0V, 4-1 V, and 4-2 V denote the off-voltage is 0, 1, and 2, respectively, and the on-voltage is 4 V.

Power density U*I (W/cm2)	Voltage Mode			
	DC 4V	4-0 V	4-1 V	4-2 V
10 HZ	0.030	0.023	0.021	0.020
50 Hz	0.030	0.029	0.026	0.023
100 Hz	0.030	0.031	0.030	0.025
200 Hz	0.030	0.036	0.035	0.029
1 kHz	0.030	0.045	0.040	0.031
10 kHz	0.030	0.049	0.049	0.032

Table 7 – The EE/O of the EAOP reactor with different on/off voltage and frequency.

EE/O (KWh/m3)	Voltage mode			
	DC 4V	0-4 V	1-4 V	2-4 V
10 HZ	3.93	2.88	2.61	2.40
50 Hz	3.93	5.02	3.41	1.83
100 Hz	3.93	7.08	6.56	3.15
200 Hz	3.93	12.87	10.90	4.46
1 kHz	3.93	53.25	31.84	7.06
10 kHz	3.93	231.05	300.12	7.15
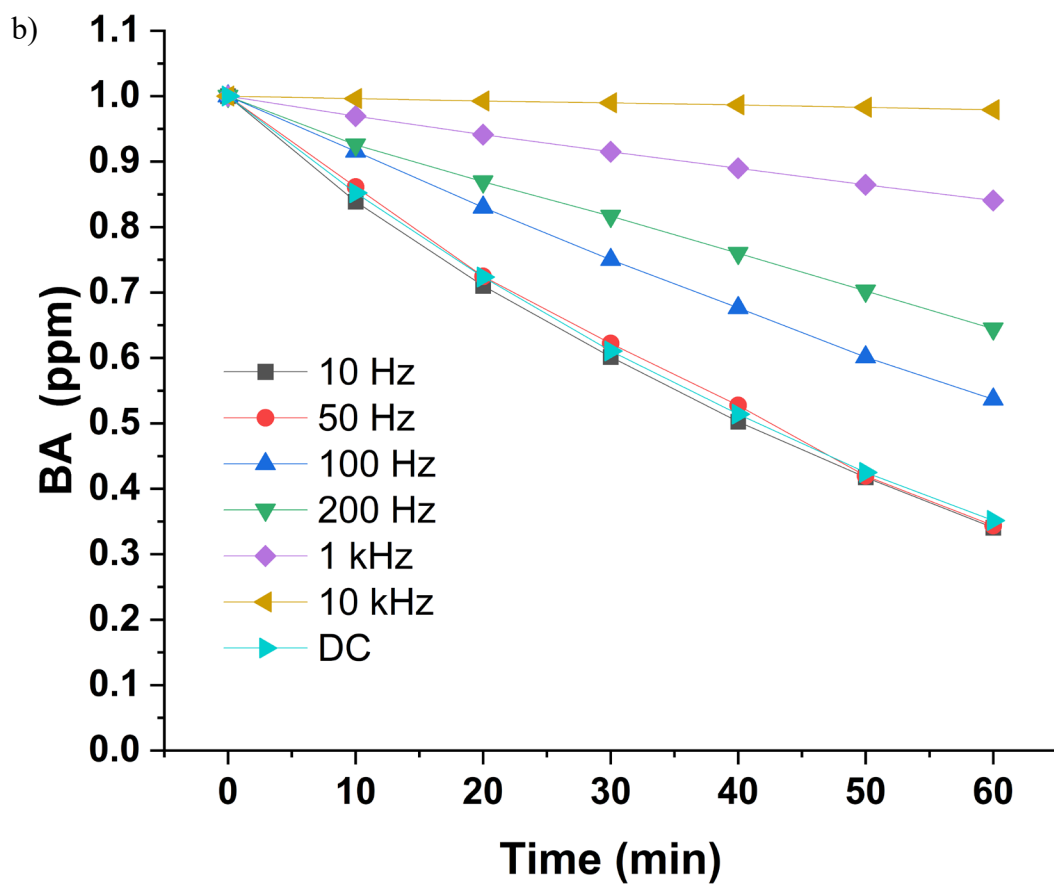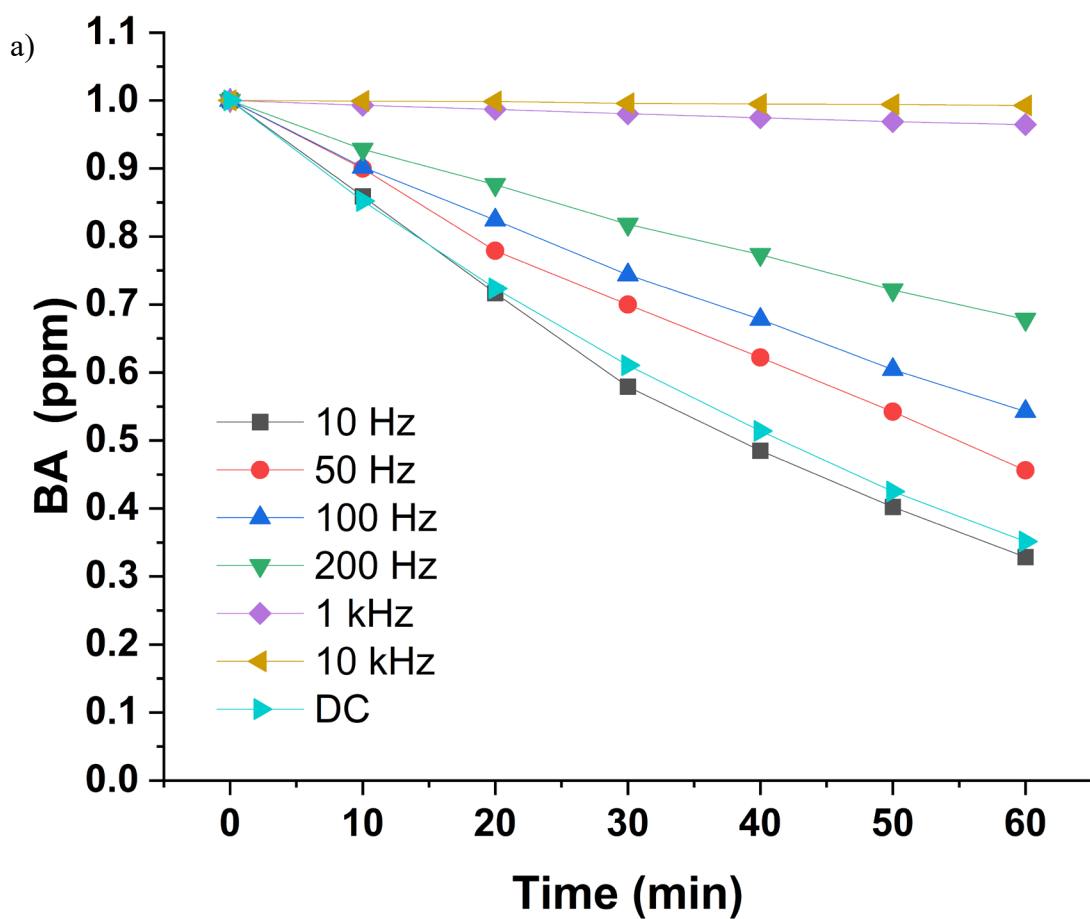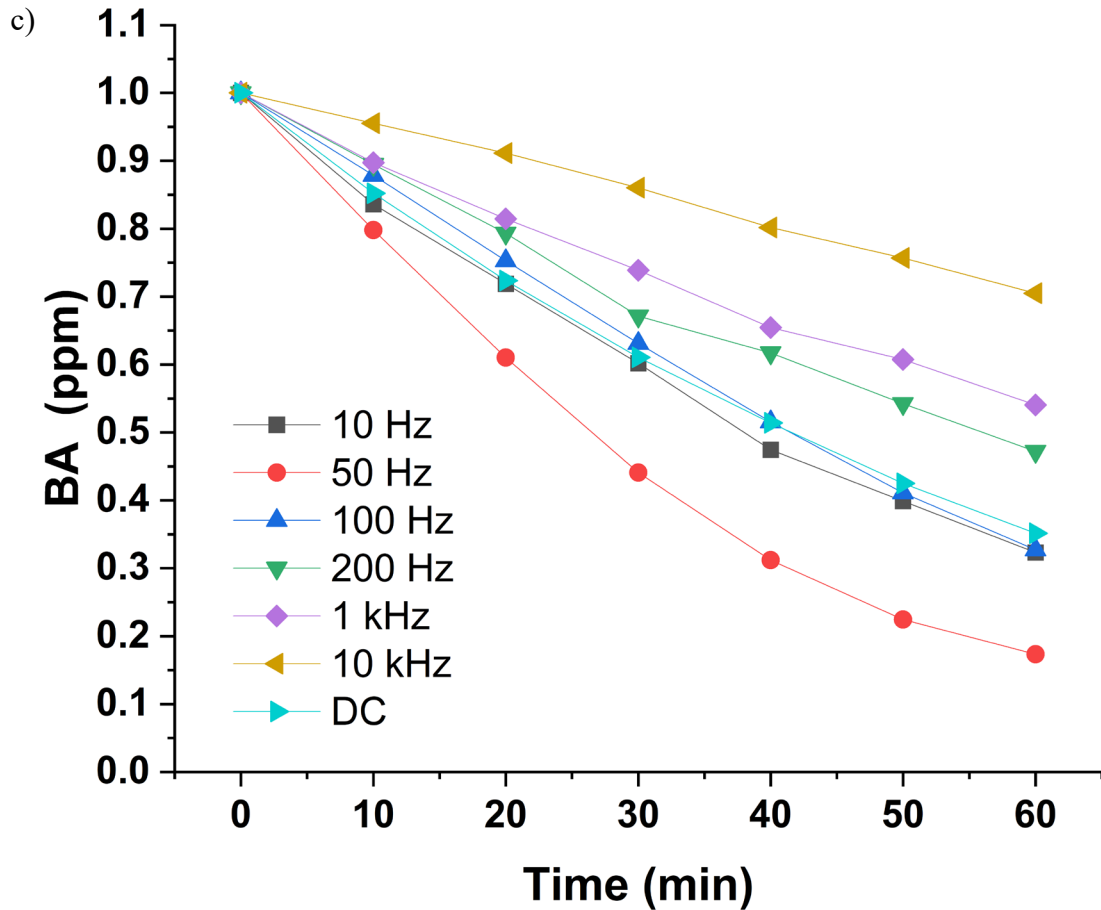
Figure 26 – a) The BA oxidation at 4-0 V mode b) at 4-1 mode and C) 4-2 mode. The initial BA concentration is 20 ppm and the Na2SO4 concentration is 0.1 M Na2SO4 with 0.5 cm electrode spacing.

Figure 26 shows the experimental data on 1-hour BA oxidation with different frequencies and off-voltage. As mentioned, the duty cycle is 50 % as default. In 1 hour experiment, the on-time of pulse potential is 30 mins, only half that of DC EAOPs. Therefore, the expected removal percentage of pulse potential EAOPs is 50 percent of that of DC EAOPs in the same current density condition. However, it is important to bear in mind that the power density of pulse potential EAOPs is certainly lower than that of the DC EAOPs but higher than the 50 % of DC EAOPs. Therefore, it is not surprising to see removal percentage of pulse

potential EAOPs is higher than 50 %. In 4-2 V Mode, the oxidation percentage of 50 Hz is even higher than the DC one, which is explained by the high current density and mass transfer during the on-time.

Figure 27 shows the IV curve of the pulse potential EAOPs. Recoding the IV investigated the non-faradic effect regarding the applied pulse frequency. The positive current density corresponds to an on-voltage state in all three cases, and the negative current corresponds to an off-voltage state, 0 V, 1 V, and 2V, respectively. In the off-time period, the negative current spike gradually converges to $0 \ mA/cm^2$ with time. To be noticed, the spike current density decreases as the off voltage rises. The 4_0 mode has the highest peak current density in an on-time period and the slowest convergent rate to $0 \ mA/cm^2$. Moreover, the 4_2 V mode has the lowest peak current and the fastest rate to drop to $0 \ mA/cm^2$. This is explicable by our description of the EIS model and the discussion about the faradic and non-faradic current based on Equation xx. In the 4_0 mode, the voltage amplitude is the largest among the three-setup condition, leading to the high peak current value. These results are consistent with EE/O and Powe density data. Though the power density of the 4_0 mode is the highest, the percentage of non-faradic is also high, leading to high EE/O. Though the 4_1 V and 4_2 V modes still have charge and discharge through the surface capacitance, a portion of the EDL charge remains adsorbed, reducing the non-faradic percentage.
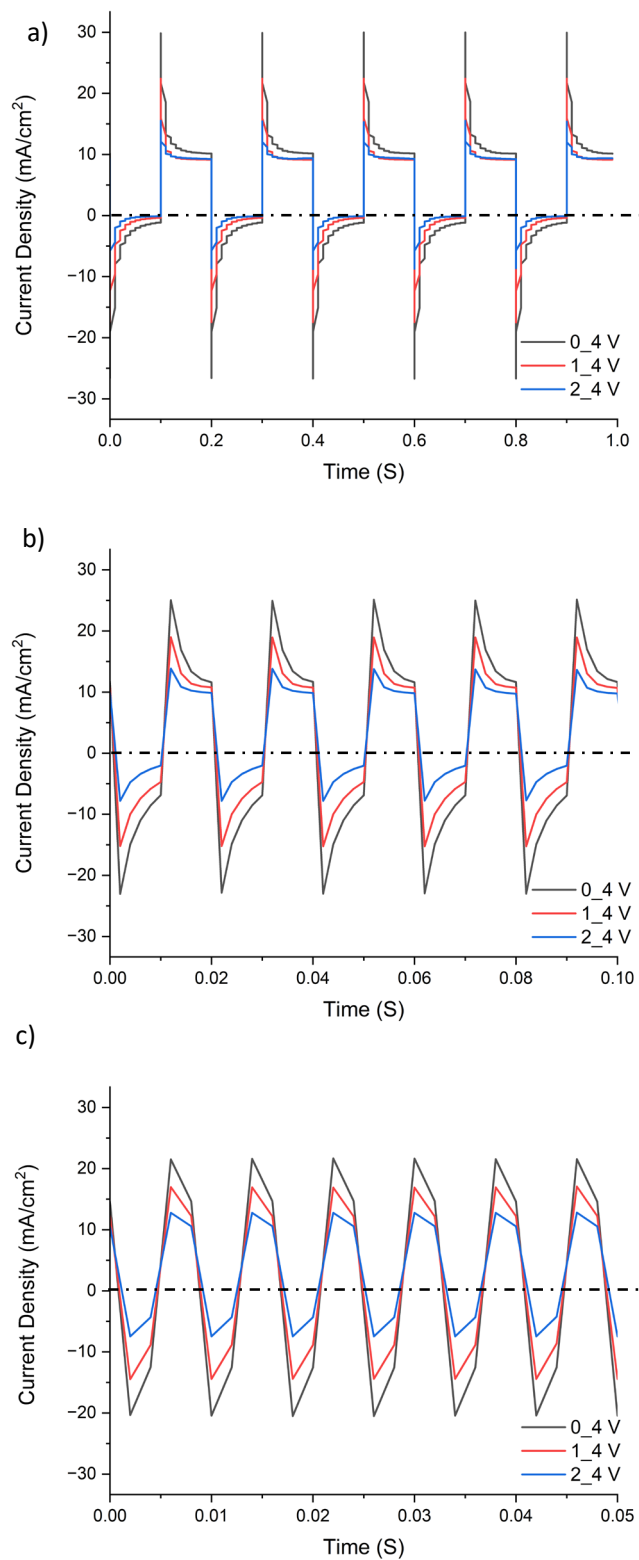
Figure 27 – The IV curve of the high-frequency pulse EAOP with 4_0 V, 4_1 V, and 4_2 V mode in a) 10 Hz, b) 100 Hz c) 200 Hz mode.

5.4. Conclusion

In this experiment, we have done high pulse EAOPs with BDD electrodes. After analysis, we can conclude that since our electrode is a broadband semiconductor, it is unsuitable for the ultra-high frequency electrolysis method in the water electrolysis field. At low and medium frequencies, the high pulse affects the mass transfer and the detachment of gas bubbles. Furthermore, we find that the energy efficiency is improved by high pulse power compared to DC. In particular, the turn-off voltage strongly influences the non-Faraday current part of the process. Therefore, a proper 1,2 V off-voltage compared to 0 V helps improve the electrode's performance in pulse potential.

CHAPTER 6. EXTRACTION OF PFOA FROM DILUTE WASTEWATER USING IONIC LIQUIDS THAT ARE DISSOLVED IN N-OCTANOL

6.1 Abstract

Polyfluoroalkyl Substances (PFAS), such as perfluorooctanoic acid (PFOA), are resistant to biodegradation leading to adverse health outcomes. Therefore, PFAS removal from drinking water is paramount. Liquid-liquid extraction processes can remove them from water; however, the hydrophobic and oleophobic properties of PFOA lead to low extraction efficiency and severe emulsification, especially for the ppm-levels concentration of PFOA. Therefore, we introduced ionic liquid (IL) methyltrioctylammonium bis(trifluoromethylsulfonyl)imide ($[A336][NTf_2]$) as extractant into octanol. We found that using hexadecyl trimethyl ammonium bromide (CTAB) as an extractant caused severe and stable emulsion. In comparison, $[A336][NTf_2]$ could suppress the emulsification with high extraction efficiency. The extraction performance of PFOA was examined as a function of various parameters. The results showed that the extraction efficiency strongly depended on the concentration of IL and aqueous pH. Further research revealed the extraction mechanisms at the molecular level, and density functional theory (DFT) and molecular dynamic (MD) simulation agreed with the trends in the experiment. We determined that the extraction efficiency of PFOA from water could be up to 88.21 wt.% for the optimized condition,

indicating that the extraction system of [A336] [NTf₂] + octanol was efficient for separating PFOA from the diluted aqueous solution

6.2   Introduction

Fluorinated compounds are widely applied in the semiconductor, polymer, and energy industries.[102-105] Among them, Polyfluoroalkyl Substances (PFAS) and their salts have been the primary concerns because they bioaccumulated in the food chain and are exceptionally resistant to typical degradation processes.[44, 106-110] The traditional low-cost methods like coagulation–sedimentation and activated sludge process are not effective enough in removing PFAS.[111, 112] In recent years, it has been reported that ion exchange, granular activated carbon, and electrocoagulation are efficient for PFAS removal.[113-116] However, they are costly and produce sludges that need further treatment. Besides, residual PFAS on activated carbon or in coagulation sludge needs to be destroyed because it is difficult to recover. The processes that can destroy them are intensively energy-demanding, for example, using thermal decomposition or ultrasonic cavitation.[117-119] For environmental sustainability, developing highly efficient and green extraction and recovery methods for PFAS separation from wastewater is necessary. This study focused on perfluorooctanoic acid (PFOA) and developed the liquid phase extraction method using ionic liquid (IL) and octanol. The concentrated PFOA in organic solution could be further concentrated using reduced pressure distillation.[119]

The main challenge for liquid-liquid extraction is the high hydrophilicity of PFOA. Though the fluorinated hydrocarbon chains are oleophobic and hydrophobic, the hydrophilic end (hydroxyl group) results in a reasonably high water solubility (9.5 g/ml).[120] The octanol-

water partition coefficient (Kow) allows a quantitative evaluation of the hydrophobicity. However, the value of PFOA cannot be obtained by the OECD shake flask because it adsorbs to the flask due to its surface reactive property.[121] Therefore, we used the Kow of perfluorooctanesulfonic acid (PFOS) to estimate it. The (Kow) of PFOS was determined to be -0.18 (log (56 mg/L in n-octanol / 680 mg/L in water), which implies we will have a low extraction efficiency for PFOA. Besides, suppressing the emulsion of n-octanol is another critical challenge because PFOA is also an emulsifier. Most extractants are water-insoluble organic liquids, and PFOA can emulsify these organic liquids. If the emulsion formed is relatively stable, it requires time to demulsify. Otherwise, it will cause a series of problems, such as a slow extraction rate, low efficiency, and secondary pollution (e.g., emulsion in the water phase).

An appropriate extractant should meet the following criteria: (1) The extractant should form a complex structure with PFOA to shift the equilibrium balance toward the organic phase. (2) The extractant should suppress the emulsification during the extraction. (3) The extractant should be hydrophobic (high solubility in the organic phase and extremely low solubility in the aqueous phase. Based on the above selection principles, hexadecyl trimethyl ammonium bromide (CTAB) and methyltrioctylammonium bis(trifluoromethylsulfonyl)imide ([A336][NTf2]) IL were chosen to enhance the liquid-liquid extraction, because both of them are long-chain quaternary ammonium salts with weak alkalinity, and can form relatively strong interaction with organic acids, which is conducive to the extraction of organic acids, such as PFOA. In order to reduce the loss of extractants in the aqueous phase, one way is to change the alkyl chain length of the cation, and the other is to change the structure of the anion. The longer

the alkyl chain length, the poorer the extraction ability; If the alkyl chain length is too short, then the hydrophilic is enhanced, resulting in the loss of extractants and secondary water contamination.[122-125] Conventional anions, such as Cl and Br, are easily solvated and hydrophilic. However, hydrophobic anions, such as NTf2, should be preferably considered. Moreover, the rationality of our choice has been further supported by other related references. CTAB has been reported to significantly increase the adsorption of PFOA to sediments or activated carbon due to electrostatic forces and hydrophobic group interactions.[126-128] As for ILs, such as [A336][NTf2], their advantages include but not limited to low vapor pressure, high thermal stability, and adjustable hydrophobicity and polarity.[129-131] The ILs could, therefore, increase water-immiscibility (low water solubility) by lengthening the alkyl chain of the cation and adopting hydrophobic anions (e.g., NTf2), resulting in the excellent suppression of the emulsification.[132, 133] Furthermore, the electrostatic or H-bonding interactions of the IL with PFOA are expected to enhance the liquid-liquid extraction significantly.[134] [A336][NTf2] has already been applied in the extraction of metal ions and organic acids (methacrylic acid and acetic acid et al.) and showed excellent stability and higher extraction efficiency.[135-137] In addition, our preliminary experimental results showed that the solubility of [A336]NTf2 in water was only 8.52 ppm. Hence, [A336] [NTf2] was selected as an extractant in this work.

We design and develop an efficient liquid-liquid extraction method for PFOA separation from the diluted aqueous solution containing a ppm-level concentration of PFOA. The effect of various parameters, i.e., the aqueous pH, IL concentration, PFOA concentration, temperature, and equilibrium time, on the separation efficiency of PFOA will be investigated,

and the optimized conditions will be obtained. The extraction mechanisms will be revealed using theoretical analysis, DFT, and molecular simulation to understand the role of IL in the liquid-liquid extraction process. We will examine the inherent differences of PFOA species (ions and/or molecules) by examining the impact of pH. This work will provide a novel approach for treating wastewater containing non-biodegradable fluorides and contribute to solving the grand challenge and green development for semiconductor, polymer, and energy industries.

6.3   Materials and methods

The extractants, [A336][NTf$_2$] (98.5% purity) and hexadecyl trimethyl ammonium bromide (CTAB, 98.0% purity), were supplied by Shanghai Aladdin Biochemical Technology Co., Ltd. The octanol used as the diluent (99.99%, Sinopharm Chemical Reagent Co., Ltd., high purity) and sodium hydroxide (98.0%, Tianjin Kermel Chemical Reagent Co., Ltd., analytical grade) were used without further purification in the experiments. Hydrochloric acid was obtained from Sinopharm Chemical Reagent Co., Ltd., and high-purity Milli-Q water (resistivity > 18.2 MΩ·cm and conductivity < 0.1μS·cm^{-1}) was used to prepare all aqueous solutions.

6.3.1   Solution preparation

The organic phase was prepared by diluting [A336][NTf$_2$] or CTAB in octanol. The aqueous solution was prepared by dissolving PFOA in water. The pH of the aqueous phase was adjusted by adding a 0.5 mol/L NaOH solution or HCl solution. All qualities were weighed by

a METTLER analytical balance accurate to ±0.0001 g. The standard deviations of the concentrations were calculated and corresponded to an experimental uncertainty of ±0.003.

6.3.2 Extraction procedure

Extraction experiments were carried out in 20 mL flasks. Equal volumes of the organic and aqueous phases were used unless otherwise stated. Firstly, the flasks were immersed in a temperature-controlled water bath. The aqueous solution was stirred for about 30 min to establish the temperature equilibrium. Then, the organic phase was mixed with the aqueous solution and stirred for another 30 min for complete extraction. Subsequently, the mixture was centrifuged at 4000 rpm for 5 min. The aqueous phase was carefully separated, and its equilibrium pH was measured. Finally, the concentrations of PFOA in the aqueous phase were determined by a high-performance liquid chromatography (HPLC) system and mass spectroscopy (MS). According to the data obtained, the extraction percentage of PFOA (E_{PFOA}) was determined using the following Equation 27:

$$E_{PFOA} = \frac{C_{i,PFOA} \times V_{i,A} - C_{e,PFOA} \times V_{e,A}}{C_{i,PFOA} \times V_{i,A}} \tag{27}$$

Where C denotes the concentration of PFOA (mg/L), and V denotes the volume of the aqueous phase (L). The subscript A denotes the aqueous solution. The subscript i and e denote the initial and equilibrated concentrations of PFOA in an aqueous solution. The extraction mechanism of the studied system containing [A336][NTf$_2$] was investigated using electrospray ionization mass spectra (ESI-MS) and Fourier transform infrared spectroscopy (FTIR). All

experiments were conducted at least three times, and the average and standard deviation were calculated and reported.

6.3.3   Apparatus and measurements

The concentration of PFOA in the aqueous phase was determined using HPLC MS using an Agilent 1100 HPLC (Agilent Technologies, Santa Clara, United States) equipped with a Zorbax SB C18 column (Agilent Technologies, Santa Clara, United States). The electrospray ionization mass spectra (ESI-MS) of [A336] [NTf2] and PFOA were acquired using a Waters/Micromass ZQ mass spectrometer (Manchester, UK) equipped with a Harvard Apparatus syringe pump. Mass spectra were acquired in the negative ion detection modes with the unit mass resolution at 1 m/z unit. The mass range for ESI experiments was from m/z = 100 to m/z = 1000. FTIR spectroscopy was used to determine the chemical compositions using a Nicolet iS50 spectrometer (Thermo Fisher Scientific Corporation, USA). The scanning frequency range was 4000-500 cm-1 under ambient conditions, with a spectral resolution of 2 cm^{-1}. The pH values of the aqueous phase were measured using a pH meter (Rex PHS-3C, China).

6.3.4   Computation details

Density functional theory (DFT) calculations were performed using the Gaussian 09 program[138]. All the geometries optimization and frequency calculations were conducted using the B3LYP-D3/ 6-31++G(d,p) basis set in both the implicit and explicit water solvent models. For each system, different geometries were screened to determine the thermodynamically favorable one.

91

All the Molecular dynamics (MD) simulations were carried out using the large-scale atomic/molecular massively parallel simulator (LAMMPS)[139]. The all-atom optimized potentials for liquid simulations (OPLS-AA) potential[140] were employed to describe the interatomic interactions, including van der Waals, bond, angle, and dihedrals interactions in the ILs and n-octanol. For n-octanol, the united atom (UA) method was used to decrease the computation time because UA is simpler while keeping its characteristic structures, where -CH_2- or -CH_3 is represented by one single bead. The van der Waals interaction between ILs and PFOA was described using the Lennard-Jones potential $4\varepsilon[(\sigma/r)^{12} - (\sigma/r)^{6}]$ at an interatomic distance r, where ε was the depth of potential well and σ was the finite distance at where the potential was zero. The Lorentz-Berthelot mixing rules were used to model the parameters of PFOA and IL, which were truncated at 1.2 nm. The long-range electronic interaction was computed using the particle-particle-particle-mesh (PPPM) algorithm.[141] The density of pure n-octanol was calculated to be 0.827 g/ml using MD methods for temperature (300 K) and 1 bar pressure, and this is very close to the experimental value, which shows the accuracy of the force field models in the MD.

The concentration of IL was controlled by changing the number of IL in the system. The corresponding numbers of IL for different C_{IL} are listed in Table S1. The size for IL-n-octanol systems was nearly $10 \times 10 \times 10$ nm^3, allowing the capture of the ionic cluster formation. The periodic boundary conditions (PBCs) were used in three directions. The system was relaxed in the NVT ensemble[142] for 5 ns. It then was relaxed in the constant pressure-temperature NPT ensemble for 25 ns. The temperature and pressure were controlled using the

Berendsen thermostat.[143] After the system was equilibrated, an additional 10 ns long simulation was carried out to collect the data for structural analysis.

6.4 Results and discussion

6.4.1 Emulsification and equilibrium conditions

Understanding emulsification is essential for repeatable results and obtaining an optimized equilibrium extraction condition. PFOA as a surfactant could cause the formation and stabilization of emulsions, which impedes the equilibrium distribution of PFOA between the organic and aqueous phases using CTAB and n-octanol. This approach required a demulsifier like methanol or acetonitrile to break the emulsion. However, the demulsifier increases the cost of PFOA extraction and causes high TOC wastewater. Moreover, the standard deviation of extraction efficiency using CTAB fluctuated wildly, indicating that it is unsuitable for industrial applications, not to mention the production of a water phase emulsion. However, no emulsification was formed with [A336] [NTf$_2$] extractant dissolved in n-octanol, which permitted the efficient extraction of PFOA. Therefore, in the following work, the extraction system of [A336] [NTf$_2$] + n-octanol was chosen for further study.

6.4.2 Equilibrium analysis

For the aqueous solution of PFOA + H$_2$O, Equations 28, 29, and 30 describe the equilibria conditions:

$$PFOA \underset{}{\overset{K_a}{\longleftrightarrow}} PFO^- + H^+ \tag{28}$$

93

$$H_2O \xleftrightarrow{\quad K_w \quad} H^+ + OH^- \tag{29}$$

$$K_a = \frac{[PFO^-]_A \times [H^+]_A}{[PFOA]_A} \tag{30}$$

The total concentration of PFOA in the aqueous phase is defined as the sum of concentrations of the free PFOA and the dissociated species, PFO$^-$ as shown in Equation 31.

$$[PFOA]_{A,\,sum} = [PFOA]_A + [PFO^-]_A \tag{31}$$

The following extraction reaction is proposed for the IL-based extraction system (Equation 32):

$$aCA + PFO^- + H^+ \leftrightarrow PFOA \cdot aCA \tag{32}$$
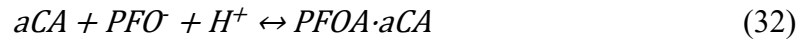
where CA denotes the IL, and a is the stoichiometric coefficients of CA in the extracted complex. Based on Equation 32, the extraction equilibrium constant of PFOA ($K_{e,\mathrm{PFOA}}$) at a specific temperature is expressed by Equation 33:

$$K_{e,PFOA} = \frac{[PFOA \cdot aCA]_O}{[H^+]_A \times [PFO^-]_A \times [CA]_A^a} \tag{33}$$

where the subscript O denotes the organic phase. The distribution coefficient of PFOA (D_{PFOA}) for the liquid-liquid extraction system can be expressed as Equation 34:

$$D_{PFOA} = \frac{[PFOA]_O}{[PFOA]_{A,sum}} \tag{34}$$

where $[PFOA]_O$ is equal to $[PFOA \cdot aCA]_O$ as shown in Equation 32 on a molar basis. Therefore, Equation 35 can be derived by combining Equations 30, 31, 33, and 34.

$$log(D_{PFOA}) = log(K_{e,PFOA}) + alog([CA]_O) - log\left(\frac{1}{K_a} + \frac{1}{[H^+]_A}\right) \qquad (35)$$

From Equation 35, it can be seen that the distribution coefficient D_{PFOA} increases with the increasing extraction equilibrium constant $K_{e,PFOA}$ and IL concentration in n-octanol. Because K_a is a constant at a fixed temperature, increasing the aqueous H^+ concentration will promote the formation of PFOA molecules rather than the dissociated species PFO⁻, which will be favorable for the extraction of PFOA to the organic phase and D_{PFOA} increases as pH decreases. We will validate this analysis in the following experiments.

6.5   Optimization of the extraction conditions

6.5.1   Effect of extraction time

The initial concentration of PFOA was 100 mg/L in the aqueous solution. The [A336][NTf2] concentration was 0.0025 mol/L in the n-octanol solution. The volume of the aqueous phase was equal to that of the n-octanol phase. Figure 28 shows the effect of the extraction time on the extraction percentage of PFOA by the [A336][NTf2] and n-octanol at 298.15 K. We found that the extraction percentage of PFOA was almost constant after 10 minutes of extraction and increased rapidly in the first 2 min to reach around 35 wt.%, and then slowly increased to 53.57 wt.% at 15 min. Therefore, we used an extraction time of 30 min for the remaining experiments.
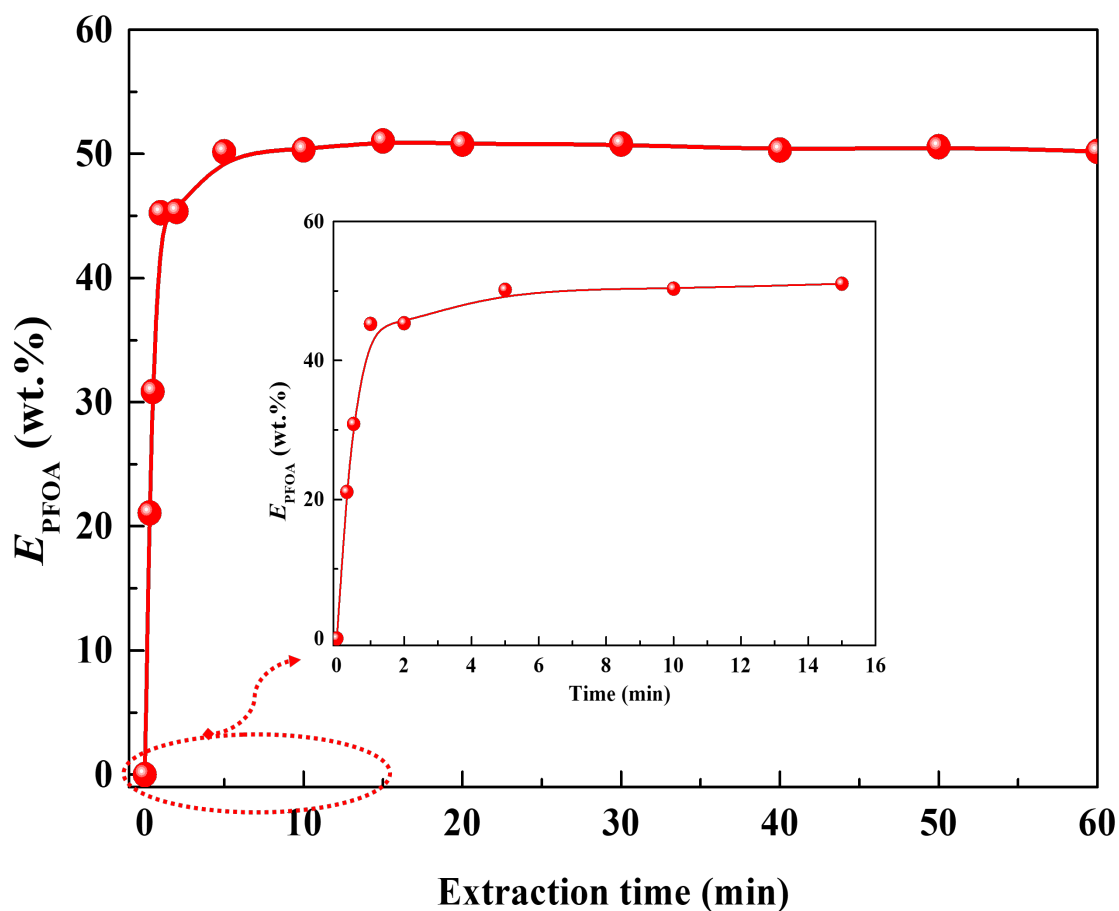
Figure 28 – The relationship between the extraction percentage of PFOA and the extraction time. The aqueous phase: 100 mg/L PFOA. The n-octanol phase: 0.0025 mol/L [A336][NTf2], T=298.15 K and ratio of the aqueous phase and organic phase (A/O) = 1:1.

6.5.2   Effect of pH

The effect of pH on the extraction efficiency and dissociation degree of PFOA and the molar ratio of Na^+ to PFO^- was investigated at the constant IL and PFOA concentrations. As shown in Figure 29, the extraction efficiency of PFOA declined from 70.61 wt.% to 35.74 wt.%, with the initial aqueous pH value increasing from 2 to 7, and then increasing to 50.64 wt.% at a pH of 10.
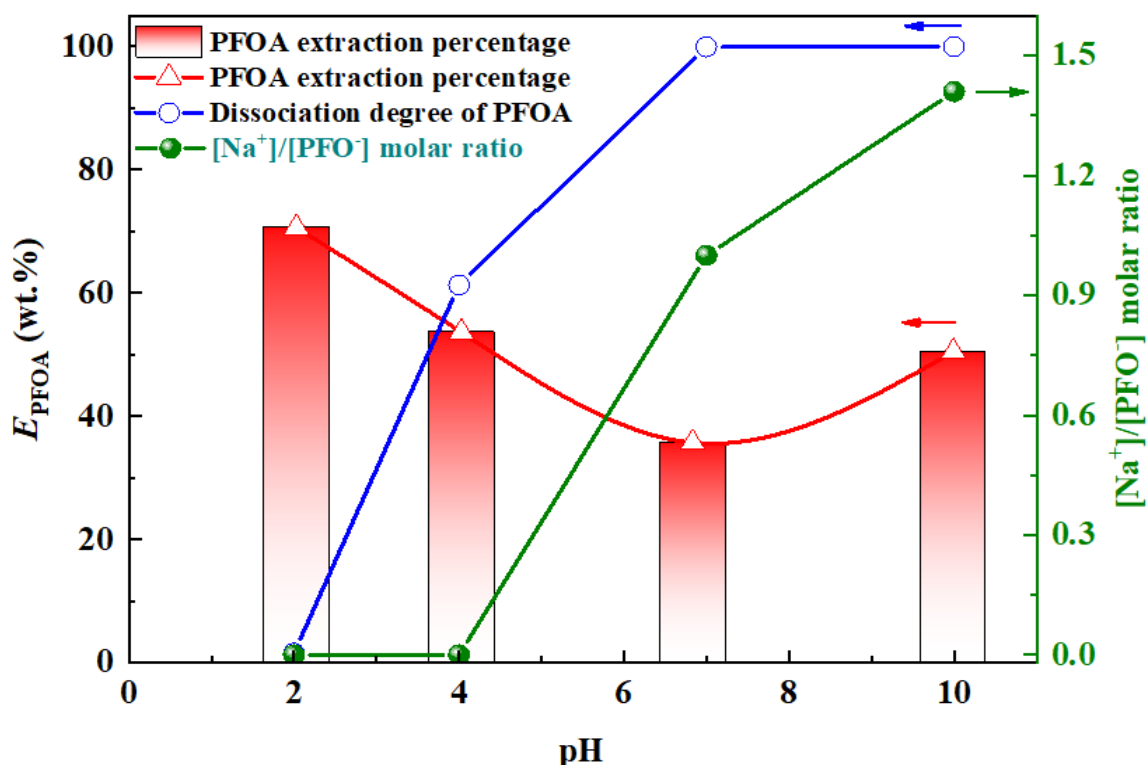
Figure 29 – Effect of pH on the extraction efficiency and dissociation degree of PFOA and [Na+]/[PFO-] molar ratio by the system of [A336][NTf2] + n-octanol at: [A336][NTf2] = 0.0025 mol/L, PFOA = 100 mg/L, T=298.15 K, extraction time=30 min, and A/O=1:1.

For PFOA, which has a carboxyl group, the ionized function group has better water solubility, while the unionized one prefers to be in the non-polar organic solvent.[144] The PFOA (pKa) dissociated constant in the water at 298.15 K is 3.8.[145, 146] Therefore, a pH that is lower than the pKa (3.8) corresponds to higher extraction efficiency, which was confirmed by the experiment results (Figure 29). The ratio of ionized PFOA, $[PFO^-]_A/[PFOA]_A$, sum (see Equation 32) increased from 1.56% to 99.94% as the pH increased from 2 to 7. The results show that the extraction of PFOA functions best in strong acid. It could be attributed to the fact that the lower the pH value, the lower the degree of dissociation. Moreover, the unionized PFOA is more hydrophobic, making it easier to enter the organic phase.

The lowest extraction efficiency of PFOA happened at a pH of around 7. It is because nearly all the PFOA molecules were dissociated into PFO$^-$ ions by the addition of NaOH, as shown in Figure 29 (blue line), and the concentration of H$^+$ was equal to that of OH$^-$, meaning that the species in the aqueous solution mainly existed in the forms of Na$^+$ and PFO$^-$ ions, and their molar ratio was equal to one. Na$^+$ and PFO$^-$ could be extracted into the organic phase, as shown in Equation 36. The extraction ability of [A336] [NTf$_2$] to Na$^+$ and PFO$^-$ ions was lower than that of the PFOA molecule.

$$aCA + PFO^- + Na^+ \leftrightarrow PFONa{\cdot}aCA \qquad (36)$$
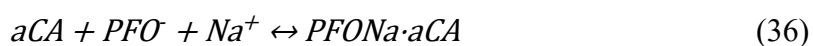
However, with a further increase of the aqueous pH to 10, the concentration of Na$^+$ was up to ~0.341 mmol/L, corresponding to a molar ratio of Na$^+$ to PFO$^-$ 1.41 as shown in Figure 29 (green line), while OH$^-$ concentration ~0.1 mmol/L. The increase of Na$^+$ concentration promoted the extraction of PFO$^-$ because of the salting-out effect.[147, 148] The concentrations of Na$^+$ in the organic phase at pH around 7 and 10 were measured to be 1.92 mg/L and 2.75 mg/L, respectively. This result indicated that, after the extraction equilibrium, the molar ratio of PFO$^-$ and Na$^+$ in the organic phase was around 1, which further proved the rationality and correctness of Equation 36.

6.5.4   *Effect of temperature*

Figure 30(a) plots the variations of E_{PFOA} as a function of the temperature (293.15 to 323.15 K), which were the experimental results three times with average relative deviations of less than 5%. The dependence of log (D_{PFOA}) against $1/T$ was shown in Figure 30(b). At first,

with the temperature increasing, both the extraction percentage and the distribution coefficient of PFOA increased, and the maximum extraction efficiency and distribution coefficient of PFOA occurred at 313.15 K. However, with different temperature rising, the PFOA extraction percentage decreased. Bai et al. found the same trend using ILs to separate methacrylic acid from dilute aqueous solutions.[38] An increase in temperature from 293.15 to 313.15 K led to a decrease in the viscosity of the organic solution from 10.01 to 4.60 mPa · s according to our experimental data, probably increasing to the free ions/ion pairs in the organic phase, which enhanced the PFOA extraction efficiency.[39] With the further increase in temperature from 313.15 to 323.15. K, the thermal motion of molecules or ions was intensified [38]; thus, the interactions between IL and PFOA were weakened, resulting in a decrease in the extraction efficiency of PFOA.
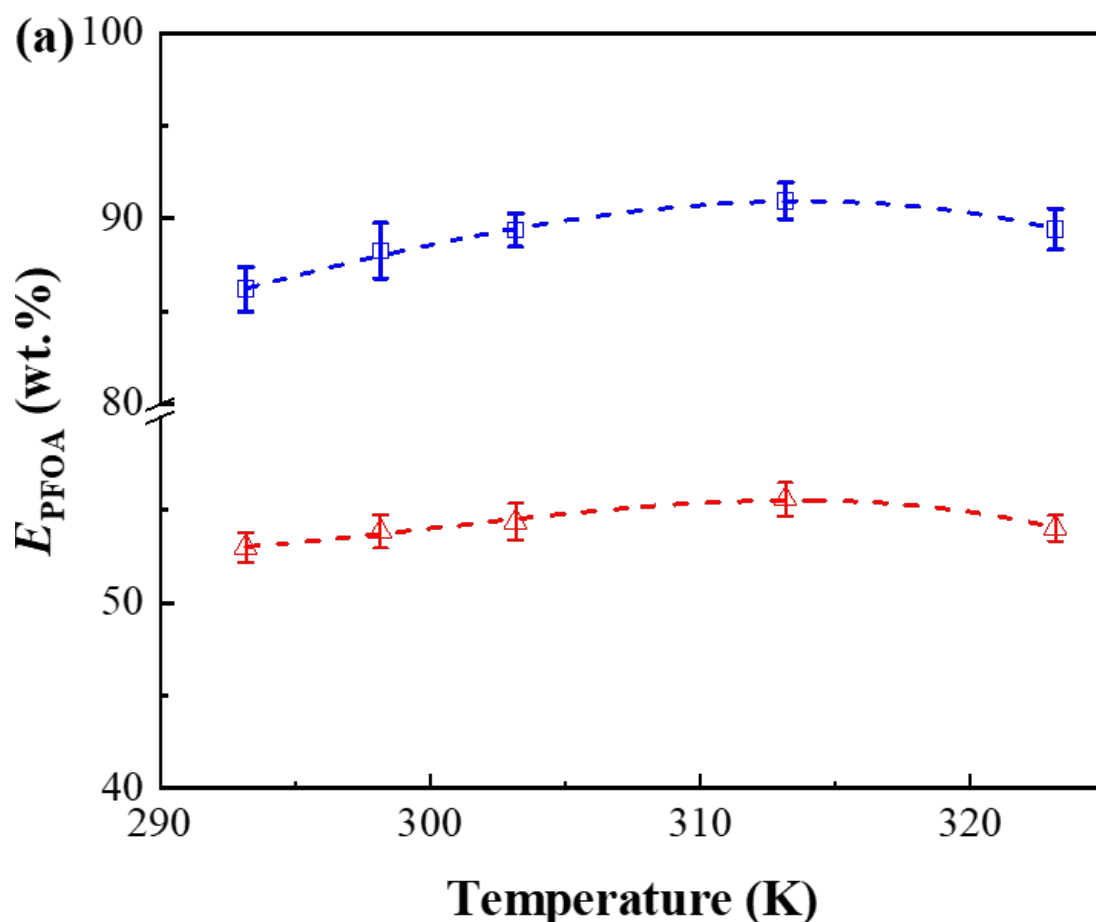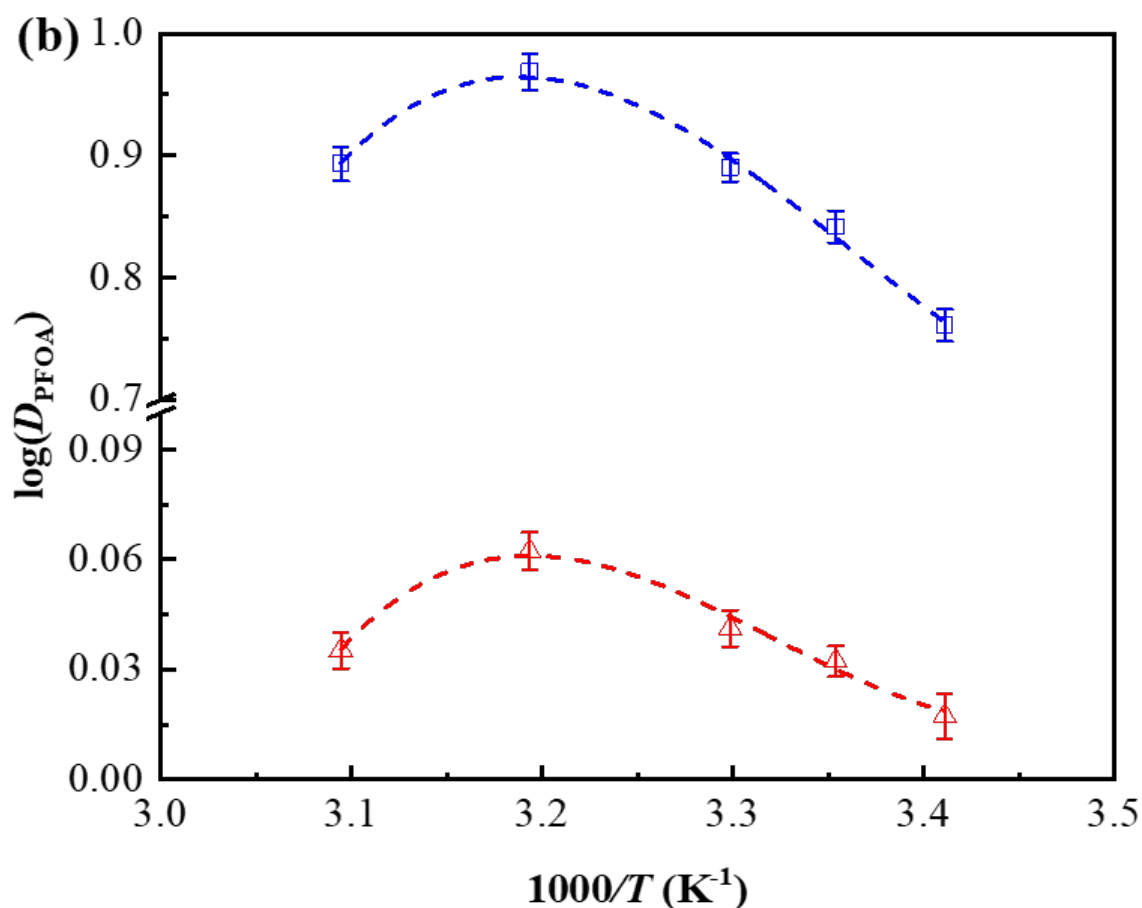
Figure 30 – Effect of temperature on the extraction efficiency of PFOA by the system of [A336][NTf2] + n-octanol at an O/A ratio of 1:1 and extraction time of 30 min; (b) Relationship of the PFOA distribution ratio versus 1/T. Red triangle (△): the experimental data at PFOA concentration 100 mg/L, Blue square (□): the experimental data at PFOA concentration 500 mg/L. The figure's red and blue dash lines are smoothed in terms of the experimental data.

6.5.5   Effect of [A336][NTf₂] concentration

The effect of [A336][NTf2] concentration in the organic phase on the PFOA extraction efficiency was investigated at the constant PFOA concentration of 100 mg/L. The [A336][NTf2] concentration range was varied from 0.00005 to 0.05 mol/L. We found in the preliminary experiments that severe emulsification occurred without the addition of [A336][NTf2]. This was similar to the PFOA extraction process using CTAB + n-octanol (Figure S1). The addition of IL eliminated the emulsification problems.
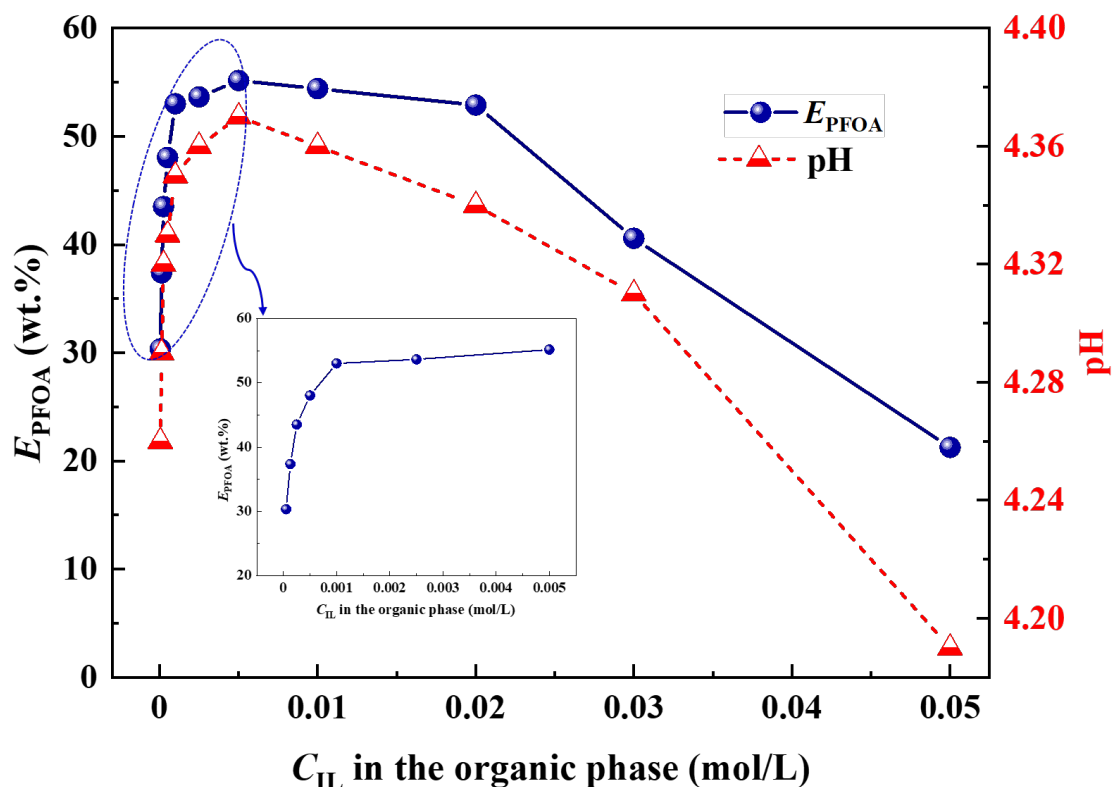
Figure 31 – The extraction efficiency of PFOA as a function of the concentration of [A336][NTf2] in n-octanol. Organic phase, 0-0.05 mol/L [A336][NTf2]; aqueous phase, 100 mg/L PFOA, no buffer added. T=298.15 K, extraction time=30 min, and A/O=1:1.

As shown in Figure 31, the extraction efficiency increased initially and then decreased.

As the [A336][NTf$_2$] concentration was in the range of 0.001~0.005 mol/L, the extraction

efficiency of PFOA reached a higher value (blue line), which was also corresponding to a

higher pH value (red line). The further addition of [A336][NTf$_2$] resulted in the obvious decline

of the PFOA extraction percentage. In order to further explain this phenomenon, the critical

micelle concentration (CMC) of IL in the organic solution was obtained by measuring the

conductivities of the [A336][NTf$_2$] + n-octanol system at 298.15 K, as shown in Figure S2.

Obviously, the CMC of IL was around 0.0018 mol/L, just corresponding to the IL concentration

range with a higher extraction efficiency level of PFOA, which further proved that the self-assembly of ILs was one of the important factors affecting the extraction efficiency.

Molecular dynamics simulations (MDs) of [A336] [NTf2] in n-octanol were performed to gain a mechanistic understanding of the process. In general, a high concentration of [A336] [NTf2] could lead to the formation of ionic clusters. The ionic cluster is defined by the nearest distance (dn) between two ions, where two ions will be viewed as in the same ionic cluster when the dn is smaller than 4.0 Å. The cluster size is simply described by the number of atoms in the single cluster. In Figure 32(a), the size distribution of clusters for the system of various C_{IL} is shown. When the concentration of IL (C_{IL}) was deficient ($C_{IL} < 0.02$ mol/L), there was only one ionic pair or small cluster (1 CA+2 AN), which was in the system. However, when C_{IL} was beyond 0.02 mol/L, a large cluster (2CA+2AN, 3CA+2AN, etc.) could be formed. The specific probability distribution function was listed in Table S3. Specifically, the maximum size of ionic cluster was 95 (1CA + 1AN) and 270 (3CA + 2AN) for C_{IL} = 0.005 and 0.02 mol/L, respectively. The detailed structure of the ionic cluster with different sizes is displayed in Figure 32(b). Interestingly, the critical point for forming the sizeable ionic cluster agreed with a decrease in extraction efficiency. That is to say, the larger cluster significantly decreased the free ion pairs in the system and decreased the productive extraction efficiency.
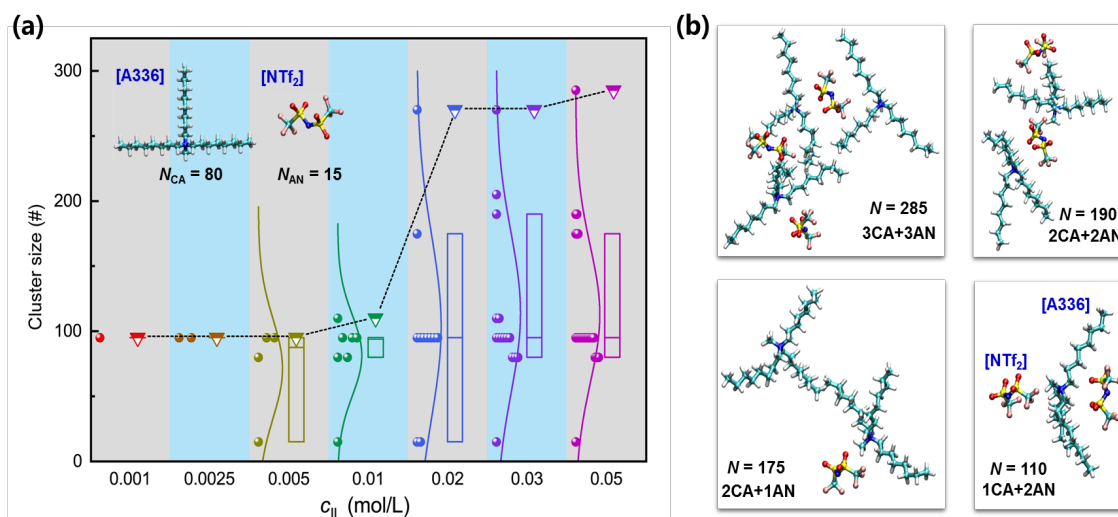
Figure 32 – (a) The cluster size distribution for the system with the different concentration of ILs, where the line in the box charts show the corresponding fraction of the cluster size. For the box chart, the horizontal lines from bottom to top represent 15, 50 and 85%, respectively. "#" represents the number of atom in the single cluster. (b) The snapshots of the ionic cluster with different sizes, where "CA" and "AN" represent the cation and anion of IL, respectively. The cyan, white, blue, red, yellow, and pink represents carbon, hydrogen, nitrogen, oxygen, sulfur,

6.5.6 Effect of PFOA concentration

The effect of PFOA concentration in the aqueous solution was investigated at a constant IL concentration of 0.005 mol/L. The PFOA concentration ranges from 20 to 1000 mg/L. As shown in Figure 33, the extraction efficiency of PFOA increased from 0.65 wt.% to 88.21 wt.%, with the increase of PFOA concentration from 20 to 500 mg/L. A further increase in PFOA concentration resulted in a decrease in the PFOA extraction percentage. These results indicated that the extraction system of [A336][NTf2] + n-octanol was also suitable for the high concentrated PFOA wastewater.

We also need to consider the impact of pH in data analysis. The initial aqueous pH values were always lower than the equilibrated aqueous pH value, as shown in Appendix3, because only PFOA, not PFO$^-$ could be extracted to the organic phase. PFOA is a strong acid.

103

This leads to a decrease in H$^+$ concentration and an increase in pH. The initial aqueous pH value decreased from 6.55 to 2.58 as the PFOA concentration increased from 20 to 1000 mg/L. Meanwhile, the equilibrated pH values changed from 6.56 to 3.08, as shown in Figure 33 (blue line). The pH change only explains the extraction of 0.5% to 0.13% dissociated PFOA. These results reconfirmed that the extraction efficiency was determined by undissociated PFOA. The maximum extraction value was 500 mg/L of PFOA corresponding to ~ 1mmol/L, while IL = 5 mmol/L.
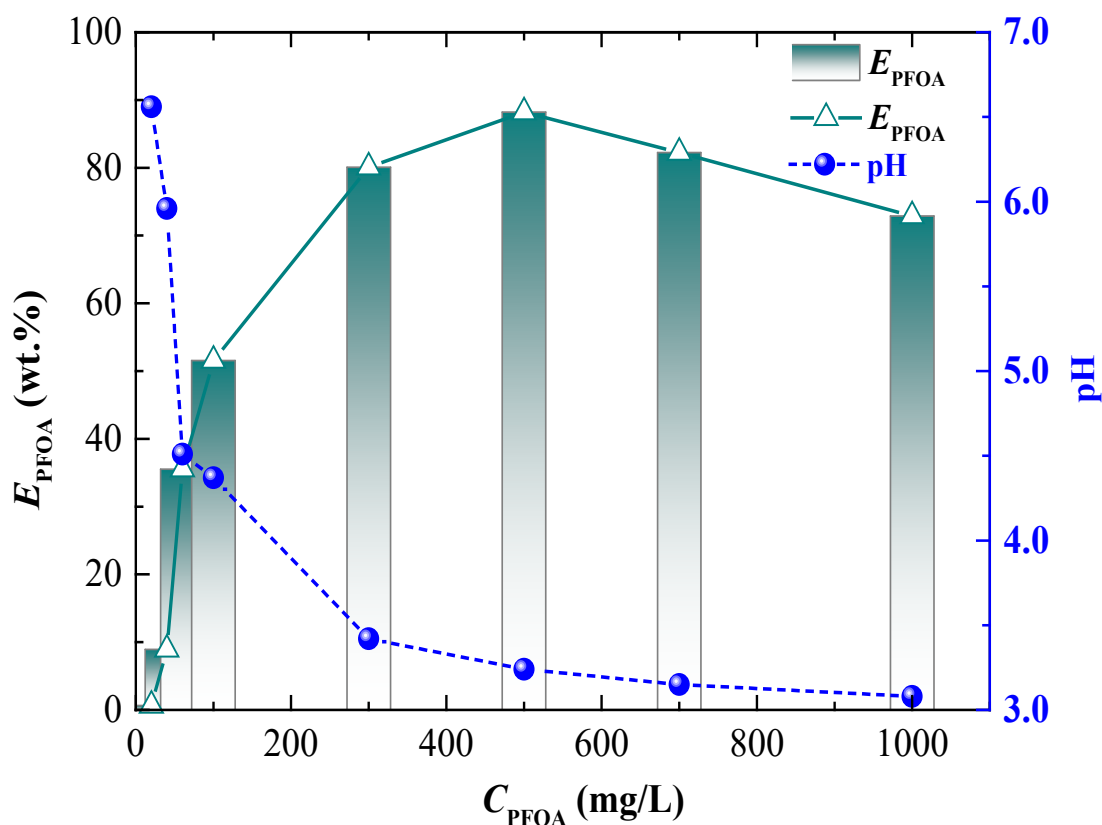
Figure 33 – Effect of PFOA concentration on the extraction of PFOA by the system of [A336][NTf2] + n-octanol at: [A336][NTf2] = 0.005 mol/L, T=298.15 K, extraction time=30 min, and A/O=1:1.

6.6   Extraction mechanisms
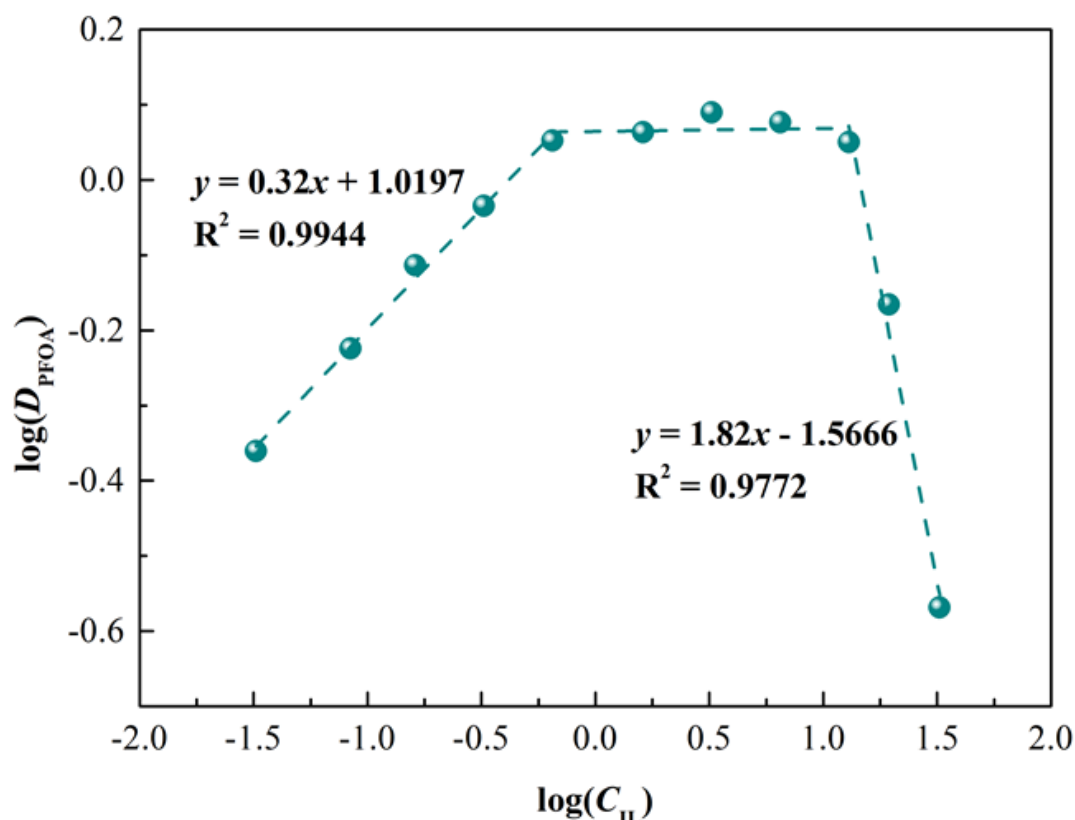
Figure 34 – PFOA extraction mechanisms using the system of [A336][NTf2] + n-octanol at: PFOA = 100 mg/L, T=298.15 K, extraction time=30 min, and A/O=1:1.

The distribution coefficient of PFOA is a function of [A336][NTf$_2$] concentration, as shown in Equation 35. Figure 34 plots the variation of log (D_{PFOA}) as a function of the logarithmic value of the [A336][NTf$_2$] concentration in the organic phase (log(C_{IL})). A linear relationship between log (D_{PFOA}) and log (C_{IL}) was obtained when the concentration of IL was lower than 0.001 mol/L. The slope of the line was 0.32, which is to say the molar ratio of [A336][NTf$_2$] to PFOA equals 1/3, which means one IL molecule involved with three PFOA in the extraction. Therefore, a possible adduct complex, 3PFOA·[A336][NTf$_2$] was formed, as shown in Equation 37.

$$3PFO^- +[A336][NTf_2]+3H^+ \leftrightarrow 3PFOA \cdot [A336][NTf_2] \qquad (37)$$
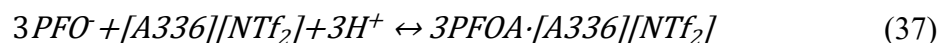
The distribution coefficient was almost constant with the further increase of [A336][NTf2] concentration to 0.02 mol/L. However, when the [A336][NTf$_2$] concentration increased from 0.02 to 0.05 mol/L, the slope of the line became negative, which was probably due to the formation of the ionic clusters of ILs in the n-octanol, as confirmed by the CMC experimental data (0.0018 mol/L IL in n-octanol) shown in Figure S2. Accordingly, not all the ILs can participate in the extraction process, especially for concentrations above 1 mol/L
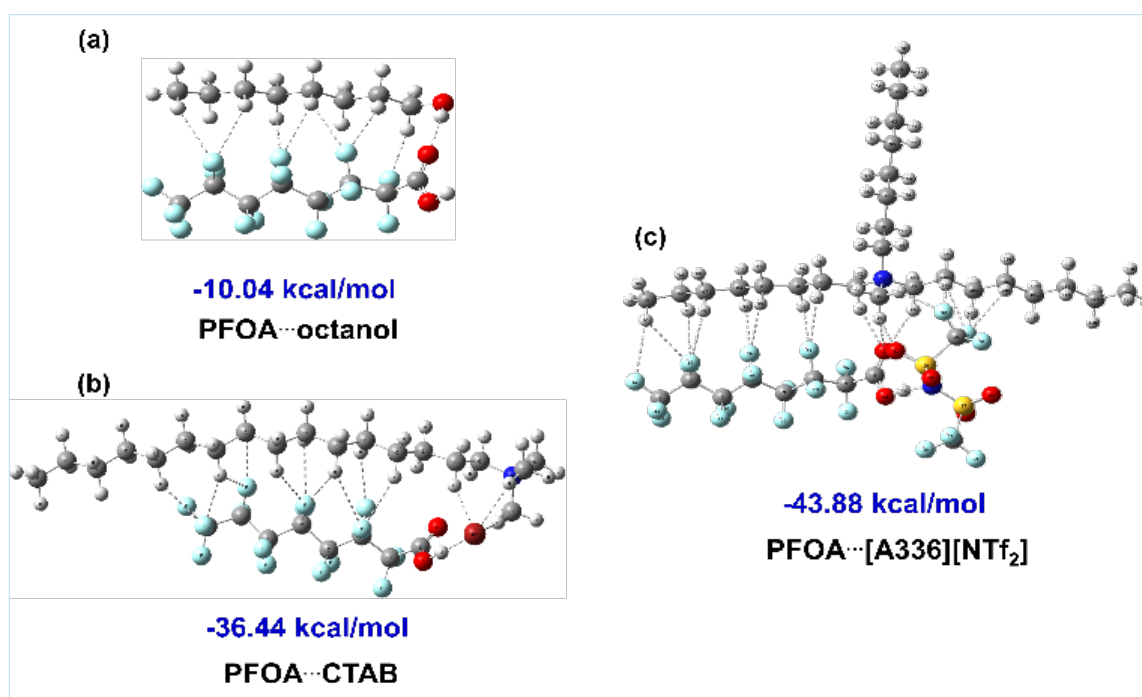
Figure 35 – Optimized complexes of the mixtures from DFT calculations: a) PFOA…octanol, b) PFOA…CTAB, and c) PFOA…[A336][NTf2].

in the n-octanol.

Also, the equilibrated organic solution was characterized by FTIR, and the highlighted spectra are shown in Appendix4. Following the literature,[149] the spectra in the range between

1000 to 1400 cm^{-1} contained the following bonds: axial stretches of CF$_2$ ($\sim$ 1363 cm^{-1}, 1319 cm^{-1}), an asymmetric stretch of CF$_2$ ($\sim$ 1238 cm^{-1}), and mixed asymmetric and axial stretches CF2 ($\sim$ 1204 cm^{-1}). In our experiments, two minor peaks (1240 cm^{-1}, 1210 cm^{-1}) were detected in the equilibrated organic phase due to CF$_2$ vibration. PFOA samples with [A336][NTf$_2$] had weaker signal peaks, which indicated that the ILs showed strong intermolecular interaction via hydrogen bond and hydrophobic group interaction. No peaks disappeared, or new peaks appeared in an n-octanol-PFOA-ILs mixed solution, indicating that no chemical reaction occurred during the extraction process.

Further, the density functional theory (DFT) calculations were carried out to understand why the extraction system of [A336][NTf$_2$] + n-octanol was more efficient than that of CTAB + n-octanol at the atomic level. Figure 35 depicts the optimized complexes of PFOA$\cdots$n-octanol, PFOA$\cdots$CTAB, and PFOA$\cdots$[A336][NTf$_2$]. In terms of the calculation of the intermolecular interaction energy (Equation 38):

$$\Delta E_{\text{(A-B)}} = 627.5 \times (E_{\text{A-B}} - E_{\text{A}} - E_{\text{B}}) \tag{38}$$

where $E_{\text{A-B}}$ (in kcal/mol) is the total energy of IL/n-octanol-PFOA complexes, E_{A} is the energy of the IL or n-octanol, and E_{B} is the energy of PFOA in a. u., respectively. The $\Delta E_{\text{(PFOA}\ldots\text{[A336][NTf2])}}$ is -43.88 kcal/mol, which is lower by 7.44 and 33.84 kcal/mol than the $\Delta E_{\text{(PFOA}\ldots\text{CTAB)}}$ and $\Delta E_{\text{(PFOA}\ldots\text{octanol)}}$. This lower energy was mainly attributed to the fact that O-H$_{\text{PFOA}}\cdots$N$_{\text{NTf2}}$ H-bond in PFOA$\cdots$[A336][NTf$_2$] is stronger than the O-H$_{\text{PFOA}}\cdots$Br$_{\text{CTAB}}$ H-bond in PFOA$\cdots$CTAB and O$_{\text{PFOA}}\cdots$HO$_{\text{octanol}}$ H-bond in PFOA$\cdots$octanol (-22.50 *vs*. -7.73 and -3.24 kcal/mol) and the C$_{\text{Alkyl}}$-H$\cdots$F H-bond in all complexes have a similar magnitude (around -2.0

~ -4.5 kcal/mol). Further investigation showed that the binding energy between PFOA with [A336][NTf2] and CTAB is governed by electrostatics (55.56% and 54.78%), whereas it is dominated by dispersion (49.37%) in PFOA···octanol. These results reveal that the interaction of PFOA···[A336][NTf2] is strong enough to extract PFOA from the aqueous phase.

Based on Equation 35, a general model considering all aspects such as pH, IL concentration, PFOA concentration, etc., was developed by fitting the experimental data at 298.15 K, as shown in Equation 39.
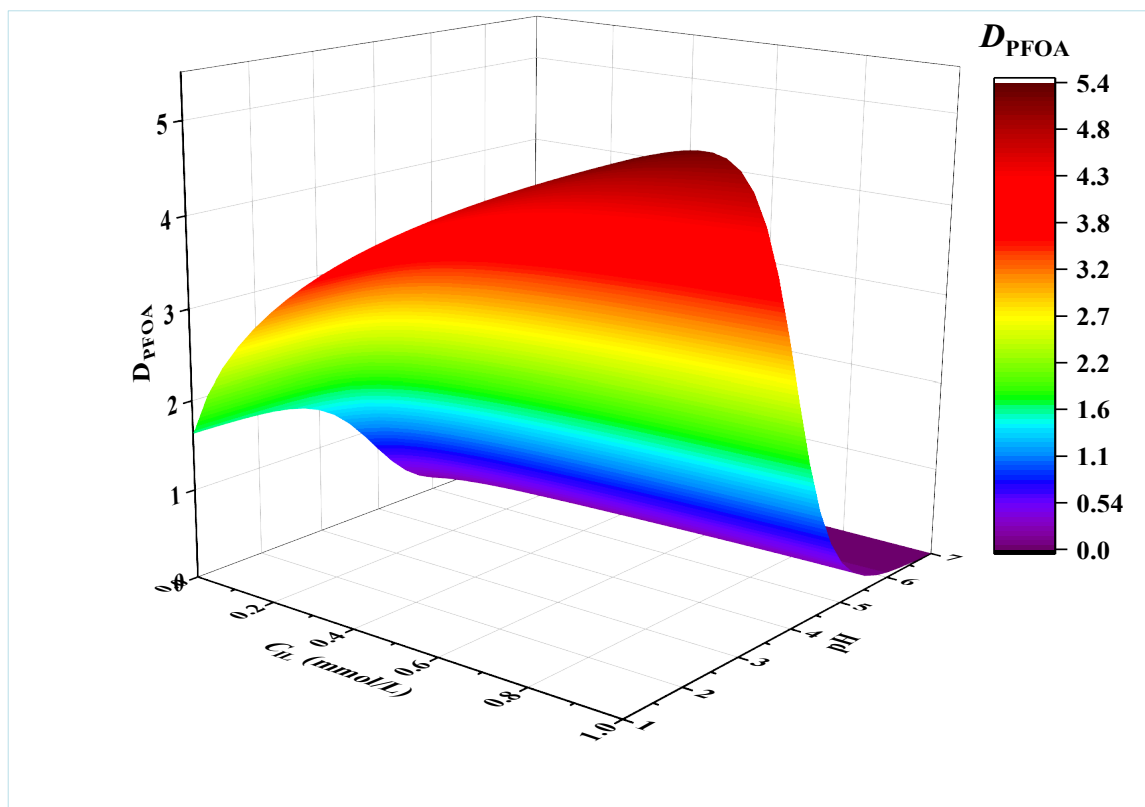
Figure 36 – The 3D surface map for the distribution coefficient of PFOA versus IL concentration and pH using the system of [A336][NTf2] + n-octanol at: PFOA = 20~500 mg/L, T=298.15 K, IL = 0~0.005 mol/L, pH=1~7 and A/O=1:1.

$$log(D_{PFOA}) = 5.25 + 0.33log([CA]_O) - log\left(6309.57 + \frac{1}{[H^+]_A}\right) \quad (39)$$

Through the model, the distribution coefficients of PFOA (D_{PFOA}) versus the IL concentration and pH values were plotted in Figure 36. It is evident that the lower the pH and the larger the IL concentration, the higher the distribution coefficient of PFOA; the larger the pH and the smaller the IL concentration, the lower the distribution coefficient of PFOA; furthermore, the effect of pH on the PFOA separation factor was more substantial than that of IL concentration. The model can determine the optimum parameters for PFOA separation from the diluted aqueous solution, which is pH less than 3, and the molar ratio of IL concentration to PFOA concentration is 1 to 2. In addition, the calculated $\log(D_{Cal,\ PFOA})$ obtained by Equation 39 was compared with the experimental $\log(D_{Exp,\ PFOA})$, as shown in Figure S5. It could be seen from this Figure that the calculated results showed a similar changing trend with the experimental values.

6.7 Conclusions

Liquid-liquid extraction of PFOA was successfully carried out using [A336][NTf$_2$] as the extractant and n-octanol as the diluent. The IL [A336][NTf$_2$] showed extremely low solubility in water and significant inhibition of emulsification during the PFOA extraction process. The extraction behavior of PFOA with IL was systemically investigated as a function of various parameters such as the aqueous pH, IL concentration, PFOA concentration, temperature, and equilibrium time. The pH of the aqueous solution was found to be critical for the PFOA extraction. Theoretical analysis, DFT, and MD simulation revealed that the extraction mechanisms differed for various pH values. At the pH of around 7, the extraction efficiency was the lowest because PFO$^-$ is the main existing form and, therefore, hard to be

extracted into the organic phase. The decrease or increase of pH from 7 was more favorable for the PFOA extraction. The extraction stoichiometry indicated the formation of a 0.32:1 complex between [A336][NTf$_2$] and PFOA when the IL concentration in the organic phase was less than 0.001 mol/L. Under the optimized experimental conditions, 88.21 wt.% PFOA from the aqueous solution could be extracted into the organic phase. Even for the aqueous solution with a low PFOA concentration (100 mg/L), the extraction efficiency of PFOA still could reach 55.16 wt.%. This work provides an efficient and green method for treating wastewater containing non-biodegradable fluorides.

CHAPTER 7. IONIC LIQUIDS ENABLING EFFICIENT EXTRACTION OF PFACS: COSMO-RS SCREENING AND EXPERIMENTAL VERIFICATION

7.1 Abstract

Liquid-liquid extraction (LLE) using ionic liquids (ILs)-based methods to remove perfluoroalkyl chemicals (PFACs), such as perfluorooctanoic acid (PFOA) and perfluorooctanesulfonic acid (PFOS), from wastewater, is an important strategy. However, the lack of physicochemical and LLE data limits the selection of the most suitable ILs for extracting PFACs. In this work, 1763 ILs for PFACs extraction from water were systematically screened using COSMOtherm to estimate the infinite dilution activity coefficient ($\ln\gamma^\infty$) of PFOA and PFOS in water and ILs. To evaluate the accuracy of COSMOtherm, 8 ILs with various $\ln\gamma^\infty$ values were selected, and their extraction efficiency (E) and distribution coefficient (D_e) were measured experimentally. The results showed that the predicted $\ln\gamma^\infty$ decreased with the increase of the experimental extraction efficiency of PFOA or PFOS, while the predicted distribution coefficient (D_p) was consistent with the experimental (D_e) results. This work provides an efficient basis for selecting ILs for extracting PFACs from wastewater.

7.2 Introduction

Perfluoroalkyl chemicals are a group of chemically stable compounds that owe their stability to strong C-F bonds. As a result, they are persistent in the environment, which leads to bioaccumulation and adverse effects on ecosystems and human health [44]. Among them,

111

perfluorooctanoic acid (PFOA) and perfluorooctane sulfonic acid (PFOS) have been recognized as the persistent organic pollutant (POP) at the fourth meeting of the Stockholm Convention [150]. After 2002, the production of PFOA and PFOS declined, and they were gradually banned in Western countries. However, they are still being produced in many developing countries [151] and are widely used in clothing treatments, leather products, and the semiconductor industry [46]. In practice, we could not eliminate fluorinated chemicals. Therefore the efficient removal of PFACs from wastewater will be required and challenging in the foreseeable future.

The conventional treatment methods are inefficient or economically infeasible [115]. For example, coagulation treatment with alum or other multivalent metals is ineffective at removing PFACs [152]. Granular activated carbon (GAC) has a large adsorption capacity, but its performance declines quickly and requires frequent replacement or reactivation, leading to high treatment costs [153]. The ion exchange method can be used to absorb PFACs, and the lifetime of the ion exchange column is ten times longer than GAC, but it has the disadvantage of being much more expensive than GAC [154]. Another main direction is defluorination. The most widely used methods are activated sludge or advanced oxidation processes (AOPs), which remain inefficient due to their limited oxidation or reduction capacity [45]. Recently, UV/persulfate and Vacuum Ultra-Violet (VUV) radiation have been applied for PFAC treatment to overcome the problem. The most challenging aspects of those methods are the formation of secondary harmful byproducts and the low energy efficiency of VUV radiation [155]. The electrochemical advanced oxidation process (EAOP) is an emerging technology that can oxidize organics with direct and indirect oxidation. It can break down PFOA or PFOS into

short-chain PFACs but cannot achieve complete mineralization [53, 156]. Given the problems existing in the above methods, as well as the extremely low concentration of PFACs in the real wastewater (ppm or ppb level), it is quickly realized that the enrichment of PFACs by pretreatment using extraction methods is a reasonable strategy.

The extraction of PFACs using common organic solvents such as octanol or long-chain polymers has been proven ineffective [157]. Ionic liquids (ILs) are promising solvents composed of organic cations and organic or inorganic anions [158, 159]. The countless combinations of those cations and anions allow engineering of the ILs properties for specific purposes [10]. In our case, the solubility of ILs can be regulated by selecting cations and anions with different hydrophobicity, which has been successfully utilized for the liquid-liquid extraction (LLE) of rare-earth metals, organic acids, esters, aromatic hydrocarbons, etc. [160-163]. Compared to other extraction methods, LLE offers the greatest energy savings and is very easy to operate, while LLE is a non-destructive method of removing PFOA/PFOS and can easily be reused after reverse extraction. The octanol-water partition coefficient (K_{ow}) is a critical metric to evaluate its feasibility. The log K_{ow} for PFOS is about -0.18, indicating that its extraction from the aqueous phase into an organic phase is quite complex [164]. However, some ILs (e.g., Fe_3O_4-cyclodextrin IL) have strong electrostatic and hydrophobic interactions with PFOA and PFOS [165]. Accordingly, LLE with IL as an extractant to extract PFOA from the aqueous was reported in our previous work [157], finding that specific ILs substantially improved the extraction efficiency in the octanol-water extraction setup. The selected ILs should be insoluble in aqueous to prevent secondary pollution to the water phase and, simultaneously, to extract the PFACs into the organics.

These requirements could translate to two important criteria: 1) high activity coefficients of ILs in water and 2) low activity coefficient for PFOA or PFOS in ILs [157]. To be noticed, as both PFOA and PFOS are surfactants, the extractant must be hydrophobic (*i.e.*, have a large activity coefficient) to prevent extreme emulsification. Therefore, a low $\ln\gamma^\infty$ of PFACs in IL (lower γ^∞ corresponding to higher solubility) is needed. The combination of cations and anions can synthesize numerous possible ILs. It would be costly to synthesize and characterize all of them. Thus, an initial screening method for selecting ILs is essential.

The Conductor-like Screening Model for Real Solvents (COSMO-RS) is suitable for fast thermodynamic calculations and screening parameters, such as γ^∞ [166-176]. The COSMO-RS predicted γ^∞ had been compared with other common solvent selection methods like the Hildebrand and Hansen solubility parameters. The results indicate that COSMO-RS is more reliable for fast solvent selection [177, 178]. The COSMO-RS model relies on the sigma profile (σ-profile) data, calculated from the molecular structure and electronic densities determined by the quantum chemical calculations based on density function theory (DFT) [179, 180]. Several studies have reported that the COSMO-RS model can be used to calculate the physicochemical properties of PFACs. For example, the COSMO-RS calculated membrane-water partition coefficient (K_{mw}) results aligned with the experimental K_{mw} values for C8-C14 alkyl chains, although it underestimated the impacts of the CF_2 and CH_2 increments and C4-C8 PFAS anions [181]. *p*Ka estimates from COSMO-RS for carboxylic acids and fluorinated carboxylic acids (including PFOA and its related short-chain substances) show differences between calculated and experimental *p*Ka in the range of ± 0.5 log unit [182, 183]. Therefore, COSMO-RS is a promising method for determining the physicochemical properties of PFOA

and PFOS. To the best of our knowledge, the COSMO-RS method has so far focused on the impact of chain length on the physical and chemical properties of fluorinated compounds, and no studies regarding the extraction of PFOA and PFOS using ILs have been reported.

This work aims to develop a method for screening the potential ILs for extracting PFOA and PFOS from wastewater. COSMO-RS was used to determine the $\ln\gamma^\infty$ for 1763 ILs, consisting of 41 cations and 43 anions. The primary goal of this analysis was to screen appropriate ILs for LLEs of PFOA and PFOS using COSMO-RS. To verify the screening method, the properties of a small number of ILs with various γ^∞ values predicted by COSMOtherm were compared with the experimental results.

7.3   Computational Details

COSMO-RS calculations were performed using COSMOtherm software (version 19.0.4, release 5528, using the parameters BP_TZVP_19, COSMOlogic (Leverkusen, Germany), with the reported standard methods.[36] The temperature was set at 298 K in our modeling. The first step in the COSMO-RS prediction procedure is to apply the continuum solvation model COSMO to simulate a virtual conductor environment for the molecule of interest. Standard quantum chemical calculations then obtain the screening charge density (σ). σ is the charge density observed outside the continuous dielectric solvent surface with the unit of e·Å^{-2}, which is the average electron charge number. The 3D distribution of the screening charge density on the surface of each molecule is converted into a surface composition function called the σ-profile. For the second step, the statistical thermodynamics of molecular interactions is performed in the COSMOtherm software. σ and σ' are the screening charges of

two interacting surface segments. $P(\sigma)$ is the probability distribution of a specific charge

density on a molecular surface segment. The interaction energies of surface pairs misfit

represent electrostatic force) are specified in terms of their respective screening charge

densities σ and σ′. The chemical potential μ_s of σ, referred to as the σ-potential, was computed

using Equation 40 as below:

$$
\mu_s(\sigma) = -\frac{RT}{a_{eff}} \ln \left[\iint P_s(\sigma') exp \left\{ \frac{a_{eff}}{RT} [\mu_s(\sigma') - E_{MF}(\sigma,\sigma') \right. \right.
$$
$$
\left. \left. - E_{HB}(\sigma,\sigma')] \right\} d\sigma' \right]
$$

(40)

Where a_{eff} stands for the effective contact area, and $P(\sigma')$ represents the surface

screening charge distribution of the whole system. The chemical potential of a compound is

calculated from the integration of the σ-potential over the surface of the molecule.

Equation 41 shows the μ of PFACs in water and ILs. At equilibrium, the μ values in

the two phases should be equal; therefore, the predicted distribution coefficient of $D_{i,p}$ is

proportional to the ratio of $\gamma_{i,L}$ to $\gamma_{i,w}$ (Equation 42).[184] In this study, the concentration of

PFACs was at ppm levels. Hence, γ_{iL} and γ_{iw} were approximately equal to γ^{∞} as calculated by

COSMO-RS. For simplicity, the ratio of $\gamma_{i,w}^{\infty}$ to $\gamma_{i,L}^{\infty}$ is defined as $D_{i,p}^*$. Further, the relative

selectivity $S_{i,j,p}^*$ can be calculated by Equation 43.

$$
\mu_i = \mu_i^* + RT ln\gamma_i x_i
$$

(41)

$$
lD_{i,p} = \frac{x_{i,L}}{x_{i,w}} = A_i \frac{\gamma_{i,w}}{\gamma_{i,L}} \approx A_i \frac{\gamma_{i,w}^{\infty}}{\gamma_{i,L}^{\infty}} \propto \frac{\gamma_{i,w}^{\infty}}{\gamma_{i,L}^{\infty}} = D_{i,p}^*
$$

(42)

$$S_{i,j,p} = \frac{D_{i,p}}{D_{j,p}} \propto \frac{D_{i,p}^*}{D_{j,p}^*} = S_{i,j,p}^* \qquad (43)$$

where μ is the chemical potential, 0 expresses the standard state; γ is the activity coefficient; x is the mole fraction; D and S represent the distribution coefficient and selectivity, respectively, D^* and S^* are the proportional relative value of the actual distribution coefficient and selectivity; i and j denote the different compounds, w and L stand for the aqueous phase and the IL phase, respectively; A is a constant value, which equals to $\exp[(\mu_{i,l}^0 - \mu_{i,w}^0)/RT]$.

From the viewpoint of thermodynamics, the ionization equilibrium constant of PFACs in water is a fixed value at a specific temperature, while in the ILs phase, they mainly exist as the molecular form. In our previous work [157], it has also been put forward that most PFOA in the aqueous solution could be extracted into the organic solvent in the form of a molecule. Therefore, the extraction process of PFACs is the distribution equilibrium of PFACs molecules in the two phases. According to Equation 43, the selectivity $S_{i,j,p}$ should be a value of $S_{i,j,p}^*$ multiplied by a constant, relating to the A_i/A_j and the ionization equilibrium constants of i and j in the aqueous phase. For simplicity, in this work, $S_{i,j,p}^*$ is applied to screen the ILs extractants, which will not affect the sequence of the predicted extraction efficiency. Thus, from the point of qualitative screening and prediction, the strategy provided in this study is practically effective.

In COSMO-RS calculation, PFOA and PFOS are treated as molecular compounds. COSMOfiles are required for all the PFOA, PFOS, water, ILs cations, and anions for the COSMO-RS prediction. All studied ILs were treated in an electroneutral way, *i.e.*, each IL was

treated as two different compounds in a stoichiometric mixture. The names and structures of PFOA and PFOS are provided in Appendix, while cations and anions of ILs are listed in Appendix. Among them, the components marked in gray in Appendix were calculated according to the method described in the literature [185]. The COSMOfiles for other components in this work were taken from the COSMO-RS database.

7.3   Materials and methods

7.3.1   Experimental materials

PFOA and PFOS were supplied by Shanghai Aladdin Biochemical Technology Co., Ltd. [N_{8881}][Tf_2N] (98.0% purity), [N_{8881}][BF_4] (98.0% purity), [N_{8881}][Tf_2N] (98.0% purity) were bought from Lanzhou Institute of Chemical Physics. [N_{8881}][PF_6] (99.0% purity), [N_{1114}][Tf_2N] (99.0% purity), [N_{1114}][BF_4] (99.0% purity), [N_{1114}][PF_6] (99.0% purity), [BMIM][PF_6] (99.0% purity), and [BMIM][BF_4] (99.0% purity) were purchased from the Shanghai Aladdin Biochemical Technology Co., Ltd. The *n*-octanol used as the diluent for the ILs (99.99%, Sinopharm Chemical Reagent Co., Ltd., high purity) was used without further purification. High-purity Milli-Q water (resistivity > 18.2 MΩ·cm and conductivity < 0.1 µS·cm^{-1}) was used to prepare all aqueous solutions. The information on the used chemicals is listed in detail in Appendix.

7.3.2   Solution preparation

The extractive systems were prepared by diluting the ILs in *n*-octanol at a 1.25 mmol/L concentration. The ILs + n-octanol, instead of pure ILs, were used as the extractive systems to

avoid the formation of emulsification. The aqueous solutions were prepared by dissolving PFOA or PFOS in high-purity Milli-Q water, and the concentration of PFOA or PFOS was kept at 50 ppm. All qualities were weighed using a METTLER analytical balance with an accuracy of ±0.0001 g.

7.3.3 Extraction procedure

Extraction experiments were carried out in 20 mL flasks. The optimized extraction conditions reported in our previous work were adopted presently with IL of 1.25 mmol/L, PFOA/PFOS of 50 ppm, O/A of 1:1 (v/v), and the temperature at 298 K and extraction time of 30 min. The volume of the aqueous phase was equal to that of the *n*-octanol phase. The detailed steps were as follows:

1) The flasks were immersed in a temperature-controlled water bath. The initial pH for the aqueous solution was measured, then the organic phase was mixed with the aqueous solution and stirred for 30 min to reach equilibrium.

2) The mixture was centrifuged at 4000 rpm for 5 min. After separating the mixture, the equilibrium pH for the aqueous solution and the volume of the two phases were measured.

3) PFOA or PFOS remaining in the aqueous phase was measured by high-performance liquid chromatography (HPLC) and mass spectroscopy (MS). According to the data obtained, the extraction efficiency of PFOA (E_{PFOA}) or PFOS (E_{PFOS}) and the distribution coefficient of PFOA (D_e) were determined by Equation 44 and Equation 45, respectively.

$$E_{\text{PFOA or PFOS}} = \frac{C_{i,\text{PFOA or PFOS}} \times V_{i,\text{w}} - C_{e,\text{PFOA or PFOS}} \times V_{e,\text{w}}}{C_{i,\text{PFOA or PFOS}} \times V_{i,\text{w}}} \tag{44}$$

$$D_e = \frac{C_{e,\text{PFOA or PFOS in IL}}}{C_{e,\text{PFOA or PFOS in }water}} = \frac{E_{\text{PFOA or PFOS}}}{1 - E_{\text{PFOA or PFOS}}} \tag{45}$$

Where C is the concentration of PFOA or PFOS (mg·L^{-1}); V is the volume of the aqueous phase (L); The subscript w denotes the aqueous solution; The subscripts i and e denote the initial and equilibrated concentrations of PFOA or PFOS in the aqueous solution.

7.3.4   *Apparatus and measurements*

The concentration of PFOA in the aqueous phase was determined by HPLC-MS using an Agilent 1100 HPLC equipped with a Zorbax SB C18 column (Agilent Technologies, Santa Clara, USA). Electrospray ionization mass spectra (ESI-MS) of PFOS were obtained using a Waters/Micromass ZQ mass spectrometer (Manchester, UK) equipped with a Harvard Apparatus syringe pump. Mass spectra were obtained in negative ion detection mode with a unit mass resolution at a step of 1 m/z unit. The mass range for ESI experiments ranged from m/z = 100 to 1000. The pH of the aqueous phase was measured using a pH meter (Rex PHS-3C, China).

7.4   **Results and discussion**

7.4.1   *Evaluation of IL extraction efficiency using the COSMO-RS model*

σ-potential is the polarization charge density, a thermodynamic property that qualitatively interprets the mixtures and their affinity towards another component.[186, 187] In general, the σ-potential can be divided into three central regions: 1) H-bond donor region (where $\sigma < -0.0082$ e·Å^{-2}, related to its ability to interact with H-bond donors), 2) non-polar region (where -0.0082 e·Å$^{-2} < \sigma < 0.0082$ e·Å^{-2}, related to its ability to interact with non-polar

groups (i.e., Van der Walls forces (VdW), and 3) H-bond acceptor region (where $\sigma > 0.0082$ e·Å^{-2}, related to its ability to interact with H-bond acceptors).[188]
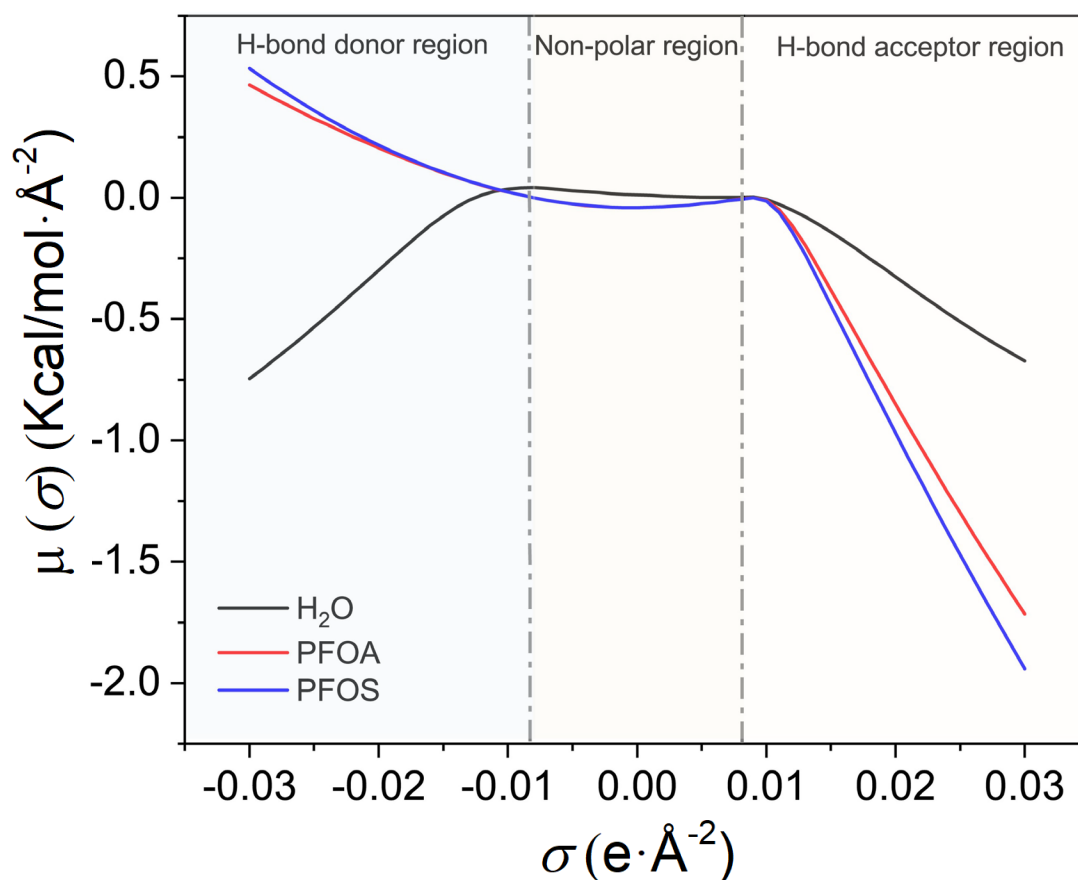
Figure 37 – σ-potentials of H$_2$O, PFOA, and PFOS predicted by COSMO-RS. The dashed vertical lines denote the 3 regions used to evaluate the H-bond donor region ($\sigma < $ -0.0082 e·Å^{-2}), non-polar region (-0.0082 e·Å$^{-2} < \sigma < $ 0.0082 e·Å^{-2}) and H-bond acceptor region ($\sigma > $ 0.0082 e·Å^{-2}).

From Figure 37, σ-potential values of PFOA and PFOS are more negative than that of water in the H-bond acceptor region, which means that PFOA and PFOS are strong H-bond acceptors. The non-polar region of PFOA and PFOS is lower than that of water due to their non-polar CF$_3$CF$_n$ chains. It also confirms that the non-polar interactions through VdW forces are also essential for the extraction process, and the finding is consistent with our previous results using Molecular Dynamics (MD) simulations.[157] In brief, it is expected that the

selected ILs can interact with PFOA or PFOS via the VdW forces and their strong H-bond acceptor groups.

For practical purposes, the selection of ILs should consider all three compounds in the system, i.e., PFOA, PFOS, and water. Therefore, we further predicted the $\ln\gamma^\infty$ of water, PFOA, and PFOS in ILs using COSMO-RS, and the results are shown in Figures 38(a)-(c). The color change from purple to red corresponds to an increase of $\ln\gamma^\infty$, corresponding to a decrease in the solubility of water, PFOA, and PFOS in ILs. ILs with cations such as $[N_{1111}]^+$, $[EMPyrr]^+$, $[P_{2228}]^+$, and $[N_{4444}]^+$ have lower predicted $\ln\gamma^\infty$ for PFOA and PFOS than the others. In addition, ILs with anions like $[Gly]^-$, $[OAc]^-$, $[2\text{-}OP]^-$, $[CPC]^-$, and $[CHC]^-$ also have a lower $\ln\gamma^\infty$ for PFOA and PFOS. Consequently, ILs like $[P_{8884}][Gly]$, $[EMPyrr][Gly]$ and $[EMPyrr][OAc]$ show an exceptionally low $\ln\gamma^\infty$ value. The σ surfaces for cations and anions (Tables S2 and S3) show the COSMOS-RS charge density distribution of the molecule, where the red and blue parts of the molecule represent the negative and positive molecular charge density, respectively. Anions such as $[Gly]^-$ and $[OAc]^-$ contain strongly negative charge densities, which provide sufficiently high σ for hydrogen bonding. As should be noted, once the screening charge density exceeds 0.0082 e·Å^{-2}, it is considered polar.[189] Common cations that exhibit good solubility for PFOA and PFOS are non-polar molecules such as $[N_{1111}]^+$ and $[N_{4444}]^+$ because they can interact with PFOA and PFOS via VdW forces, as shown in our previous work.[157]

In contrast to the $\ln\gamma^\infty$ for PFOA and PFOS in ILs, the desired $\ln\gamma^\infty$ of water in ILs should be high, as severe emulsification may form if water is partially dissolved in ILs.

According to the report of Khan et al.,[190] the solubility property of water in ILs can be divided into three regions: 1) $\ln\gamma^\infty < -2.2$, water is completely soluble in ILs, 2) $-2.2 \leqslant \ln\gamma^\infty \leqslant -0.03$, water is partially dissolved in ILs, and 3) $\ln\gamma^\infty > -0.03$, water is insoluble in ILs. We cited these three intervals in our work and cited the relevant literature.[43] Thus, for the screening of ILs, $\ln\gamma^\infty$ of water more than -0.03 is strongly recommended. In combination with the soluble region of PFOA and PFOS in ILs, 43 ILs were identified as possible candidates for extracting PFOA and PFOS from H_2O. They include the following cations $[N_{8881}(NH_2)_2]^+$, $[N_{8888}]^+$, $[N_{8881}]^+$, $[N_{4444}]^+$, $[N_{11116}]^+$, $[P_{66614}]^+$, $[P_{8884}]^+$, $[P_{4442}]^+$, $[P_{2228}]^+$, $[P_{4442}OH]^+$, $[C_8Mmim]^+$, and these anions $[BH_2(CN)_2]^-$, $[BF_4]^-$, $[B(CN)_4]^-$, $[Tf_2N]^-$, $[ClO_4]^-$, $[I]^-$ (Table **8**). Of these, the ILs formed from $[I]^-$ were reported to undergo hydrolysis in water, which prevents them from being considered further.
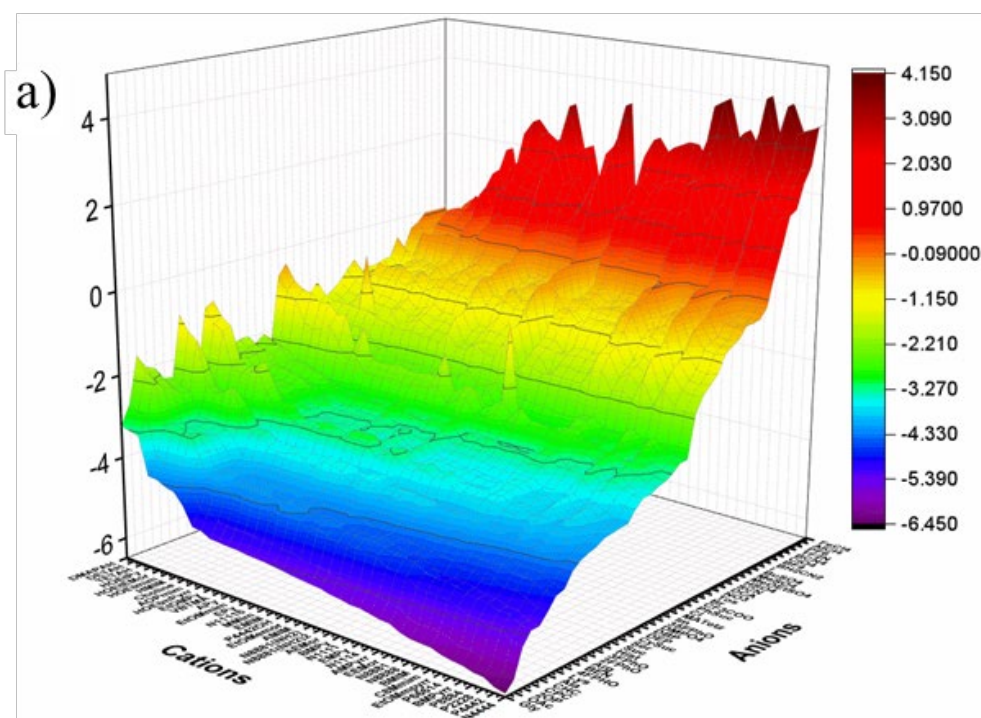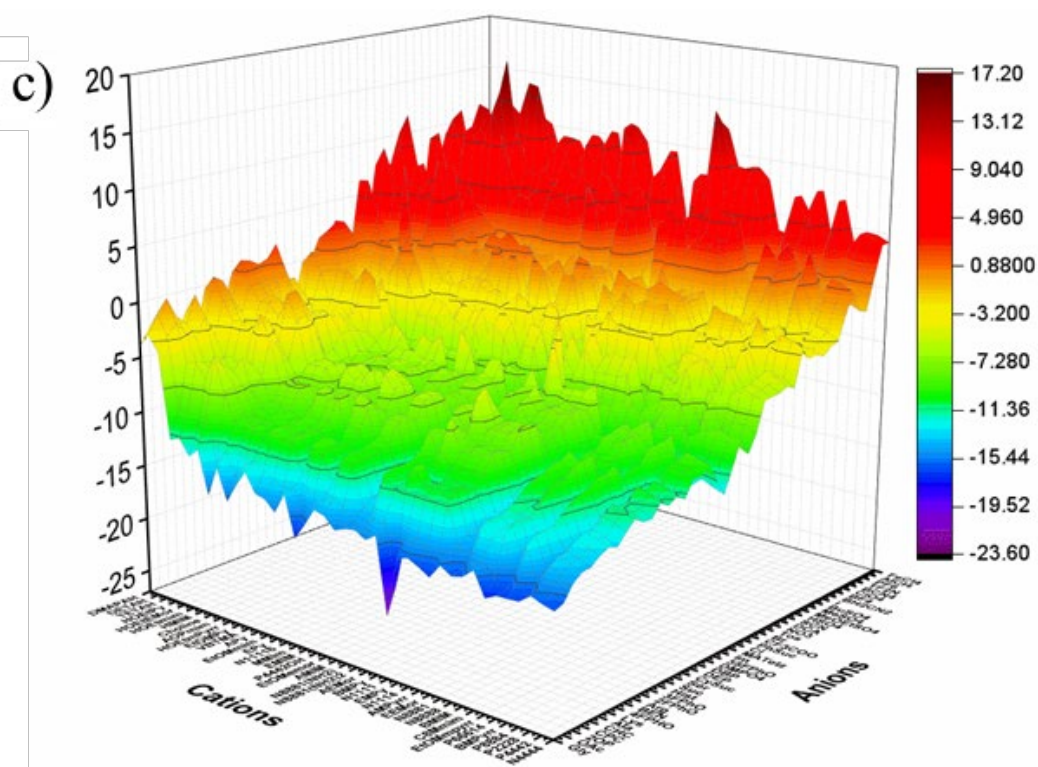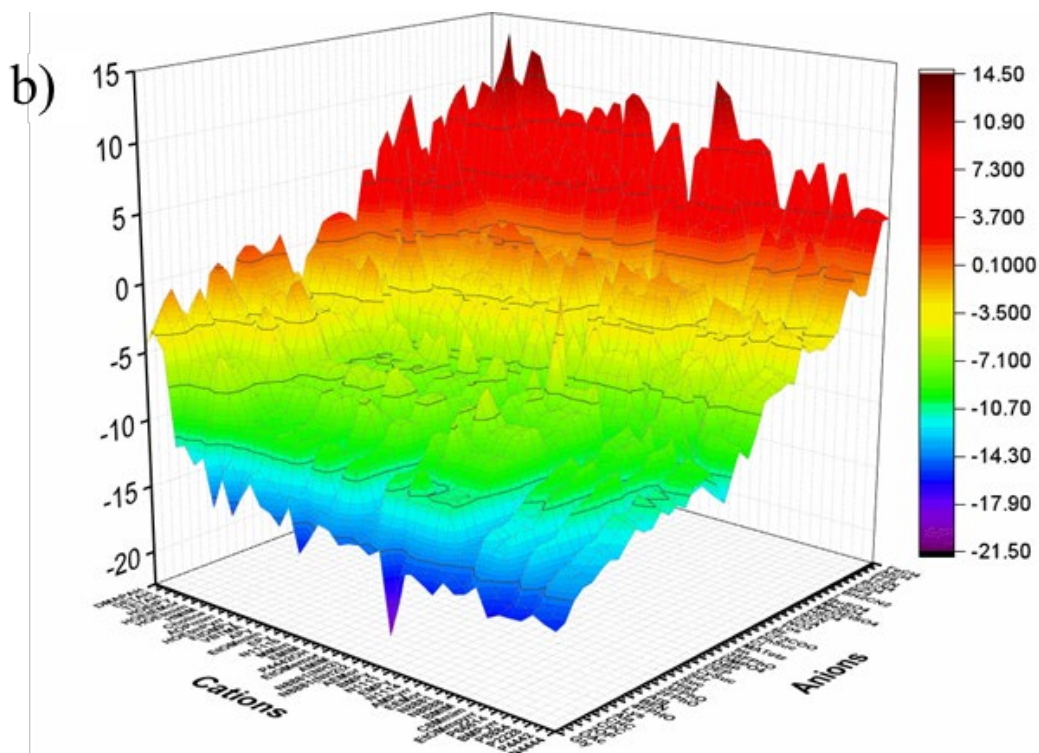
Figure 38 – COSMO-RS prediction of the logarithmic infinite dilution activity coefficient (lnγ∞) of (a) water, (b) PFOA, and (c) PFOS in ILs at 298 K. The full name of the cations and anions in Figure 2 are provided in the supporting information. The ILs used for the prediction can be combined freely by cations and anions

Table 8 – The logarithmic infinite dilution activity coefficient ($\ln\gamma^\infty$) of PFOA and PFOS at 298 K in selected ILs.

No.	ILs	$\ln\gamma^\infty$		
		PFOA	PFOS	H_2O
1	$[N_{8881}(NH_2)_2][BH_2(CN)_2]$	-8.42	-8.95	-1.20
2	$[P_{66614}][BH_2(CN)_2]$	-4.13	-4.31	1.03
3	$[P_{8884}][BH_2(CN)_2]$	-4.03	-4.16	0.88
4	$[N_{8888}][BH_2(CN)_2]$	-3.96	-4.10	0.92
5	$[N_{8881}][BH_2(CN)_2]$	-3.49	-3.56	0.79
6	$[N_{8881}][I]$	-3.39	-3.19	0.12
7	$[N_{4444}][BH_2(CN)_2]$	-3.26	-3.20	0.46
8	$[P_{4442}][BH_2(CN)_2]$	-2.68	-2.53	0.39
9	$[P_{2228}][BH_2(CN)_2]$	-2.40	-2.24	0.40
10	$[N_{11116}][BH_2(CN)_2]$	-2.02	-1.92	0.62
11	$[P_{66614}][BF_4]$	-1.84	-1.86	1.75
12	$[P_{66614}][B(CN)_4]$	-1.77	-1.87	2.40
13	$[P_{8884}][BF_4]$	-1.76	-1.75	1.57
14	$[P_{8884}][B(CN)_4]$	-1.74	-1.82	2.25
15	$[N_{8888}][BF_4]$	-1.73	-1.72	1.59
16	$[P_{4442}OH][BH_2(CN)_2]$	-1.70	-1.50	0.20
17	$[N_{8888}][B(CN)_4]$	-1.70	-1.78	2.24
18	$[C_8Mmim][BH_2(CN)_2]$	-1.52	-1.28	0.41
19	$[N_{8881}][B(CN)_4]$	-1.39	-1.41	0.79
20	$[N_{4444}][Tf_2N]$	-1.34	-1.43	2.40
21	$[N_{8881}][BF_4]$	-1.31	-1.22	1.39
22	$[P_{8884}][Tf_2N]$	-1.29	-1.43	2.80

Table 8 continued

23	[N$_{8881}$(NH$_2$)][B(CN)$_4$]	-1.29	-1.32	1.94
24	[N$_{4444}$][B(CN)$_4$]	-1.24	-1.18	1.84
25	[N$_{8888}$][Tf$_2$N]	-1.21	-1.35	2.77
26	[P$_{66614}$][Tf$_2$N]	-1.19	-1.33	2.93
27	[N$_{8881}$(NH$_2$)][BF$_4$]	-1.18	-1.08	1.28
28	[N$_{4444}$][BF$_4$]	-1.15	-0.96	1.06
29	[N$_{8881}$][Tf$_2$N]	-1.12	-1.23	2.61
30	[P$_{4442}$][Tf$_2$N]	-1.12	-1.18	2.29
31	[N$_{8881}$(NH$_2$)][Tf$_2$N]	-1.03	-1.13	2.43
32	[P$_{2228}$][Tf$_2$N]	-0.97	-1.02	2.23
33	[P$_{4442}$][B(CN)$_4$]	-0.76	-0.63	1.73
34	[P$_{4442}$OH][Tf$_2$N]	-0.69	-0.68	0.99
35	[P$_{4442}$][BF$_4$]	-0.67	-0.39	0.92
36	[C$_8$Mmim][Tf$_2$N]	-0.57	-0.59	2.15
37	[P$_{2228}$][B(CN)$_4$]	-0.54	-0.40	1.70
38	[N$_{11116}$][Tf$_2$N]	-0.54	-0.56	2.23
39	[P$_{66614}$][ClO$_4$]	-0.52	-0.40	2.38
40	[P$_{2228}$][BF$_4$]	-0.41	-0.11	0.90
41	[N$_{8888}$][ClO$_4$]	-0.40	-0.25	2.21
42	[P$_{8884}$][ClO$_4$]	-0.40	-0.24	2.21
43	[N$_{11116}$][B(CN)$_4$]	-0.31	-0.19	1.77

7.4.2 Experimental validation

As seen in Table **8**, the activity coefficients exhibit a wide range of variation. Therefore, we selected ILs with a range of distribution coefficients to check the accuracy of COSMO-RS. Based on the predicted results, these cations $[N_{8881}]^+$, $[N_{1114}]^+$, $[BMIM]^+$, and these anions of $[Tf_2N]^-$, $[BF_4]^-$, $[PF_6]^-$ were selected. For the selected 8 ILs, $[N_{8881}][Tf_2N]$ and $[N_{8881}][BF_4]$ come from the optimized region of $\ln\gamma^\infty$ of water more than -0.03, while for the rest of 6 ILs of $[N_{8881}][PF_6]$, $[N_{1114}][Tf_2N]$, $[N_{1114}][BF_4]$, $[N_{1114}][PF_6]$, $[BMIM][BF_4]$, $[BMIM][PF_6]$ of $-2.2 \leq \ln\gamma^\infty \leq -0.03$ to verify the accuracy of the prediction result. The experimental values of $\ln D_e$ of PFOA and PFOS of these 8 ILs and pure octanol extractants are listed in Table 9.

Table 9 – The experimental results (*E*, *D*, and pH after extraction equilibrium) for PFOA and PFOS.

No.	ILs	PFOA			PFOS		
		E (%)	D_e	pH	*E* (%)	D_e	pH
1	[N$_{8881}$][Tf$_2$N]	33.70	0.51	4.48	49.50	0.98	4.38
2	[N$_{8881}$][BF$_4$]	25.60	0.34	4.35	38.20	0.62	4.29
3	[N$_{8881}$][PF$_6$]	16.60	0.20	4.27	28.10	0.39	4.21
4	[N$_{1114}$][Tf$_2$N]	8.60	0.09	4.51	22.30	0.29	4.43
5	[N$_{1114}$][BF$_4$]	5.10	0.05	4.43	12.50	0.14	4.34
6	[N$_{1114}$][PF$_6$]	1.80	0.02	4.36	6.20	0.07	4.30
7	[BMIM][BF$_4$]	12.50	0.14	4.34	19.30	0.24	4.27
8	[BMIM][PF$_6$]	7.80	0.08	4.26	15.60	0.18	4.23
9	Pure Octanol	1.96	0.02	4.90	3.85	0.04	4.87

Note: Experimental conditions: concentration of IL = 1.25 mmol/L, concentration of PFOA/PFOS = 50 ppm, O/A = 1:1 (v/v), temperature = 298 K, initial pH value of PFOA solution = 4.11, initial pH value of PFOS solution = 4.05, and extraction time = 30 min.

From Table 9, the D_e for ILs was up to 5 times higher than the D_e pure octanol, indicating that ILs were superior extractants. In Figure 3, the COSMOS-RS model predictions $\ln D_p^*$ are compared with the experimental data $\ln D_e$, it can be seen that the correlation coefficients were 0.90 and 0.95 between $\ln D_e$ and $\ln D_p^*$ for PFOA and PFOS, respectively,

indicating that $\ln D_e$ and $\ln D_p^*$ are linearly correlated, which is in agreement with the theoretical

Equation 3. Meanwhile the $\ln D_p^*$ values of PFOS were consistently higher than those of PFOA,

meaning PFOS is easier to be extracted than that of PFOA, which is also consistent with the

results for $\ln D_e$. The detailed data of $\ln D_p^*$ for PFOA and PFOS are listed in Tables S5, and S6,

respectively, and the corresponding 3D plots are illustrated in Appendix1. For ILs with the

same cation but different anions, the relative difference in $\ln D_p^*$ values were significantly larger

than ILs with the same anion but different cations, indicating that the predicted $\ln D_p^*$ was more

sensitive to the types of anions rather than to the cations. For example, for ILs with the same

cation $[N_{8881}]^+$, the $\ln D_p^*$ values for PFOA were +26.42 for $[N_{8881}][Gly]$ and +12.52 for

$[N_{8881}][Tf_2N]$ (Table S5). And for PFOS they were +29.13 for $[N_{8881}][Gly]$ and +14.86 for

$[N_{8881}][Tf_2N]$ (Table S6). For ILs with the same anion, the $\ln D_p^*$ values for PFOA varied from

+26.42 of $[N_{8881}][Gly]$ to +26.58 of $[P_{4442}][Gly]$ (Table S5), while $\ln D_p^*$ values of PFOS were

+29.13 for $[N_{8881}][Gly]$ and +29.64 for $[P_{4442}][Gly]$ (Table S6). Therefore, it can be concluded

from the predicted $\ln D_p^*$ values that anion selection significantly influences the extraction of

PFOA and PFOS from water using ILs.

In general, as both PFOA and PFOS are present in water, thus the selectivity of the ILs is of great importance. The higher the selectivity (S), the easier it is to extract PFOA or PFOS from the wastewater. Appendix2 shows the predicted logarithmic selectivity ($\ln S_p^*$) of PFOA to PFOS in ILs at 298.15 K. It is evident that $\ln S_p^*$ of PFOA concerning PFOS is always less than zero. The results indicate that the selectivity of PFOS in ILs is higher than that of PFOA, which is generally consistent with the experimental results. Take [N$_{8881}$][Tf$_2$N], [N$_{8881}$][BF$_4$], [BMIM][BF$_4$], and [BMIM][PF$_6$] as examples, the $\ln S_p^*$ values of [N$_{8881}$][Tf$_2$N] and [N$_{8881}$][BF$_4$] are 2.35 and 2.15, respectively, showing the same tendency with the experimental $\ln D_e$.
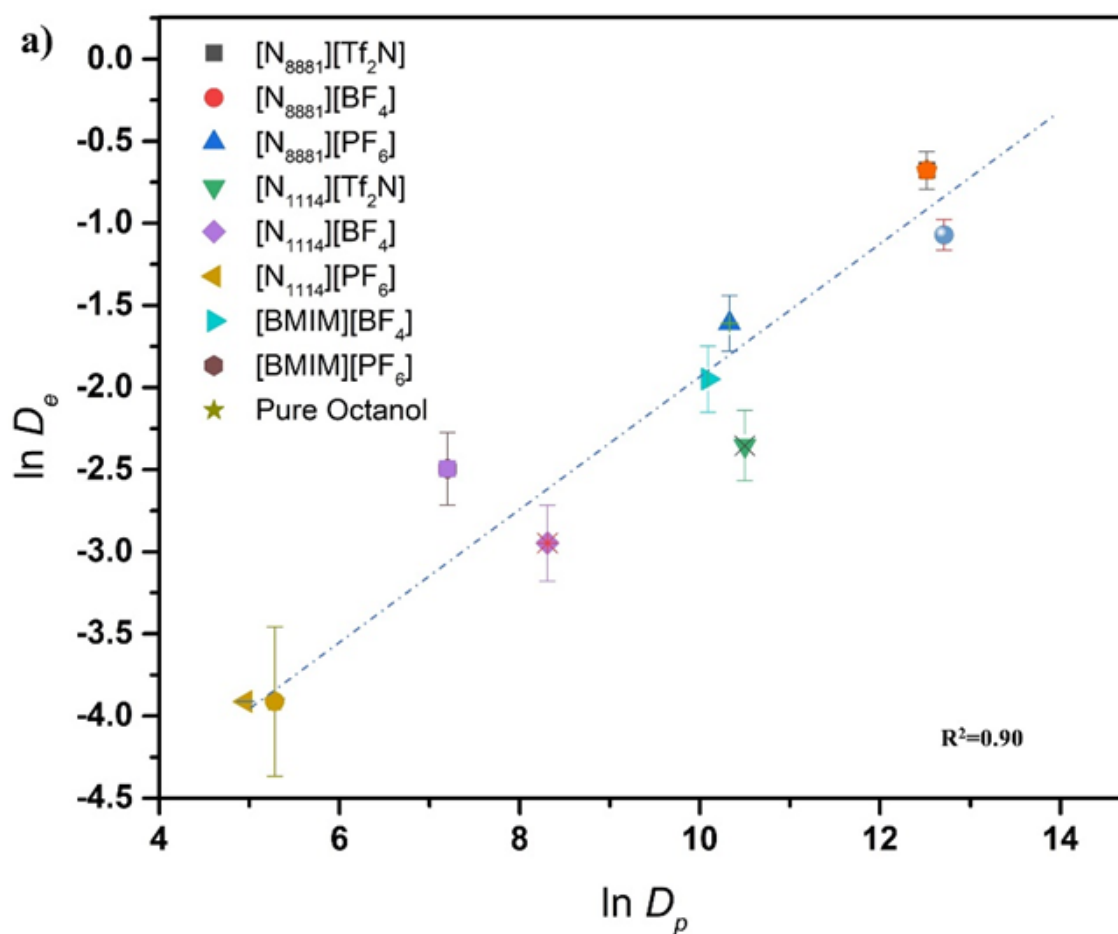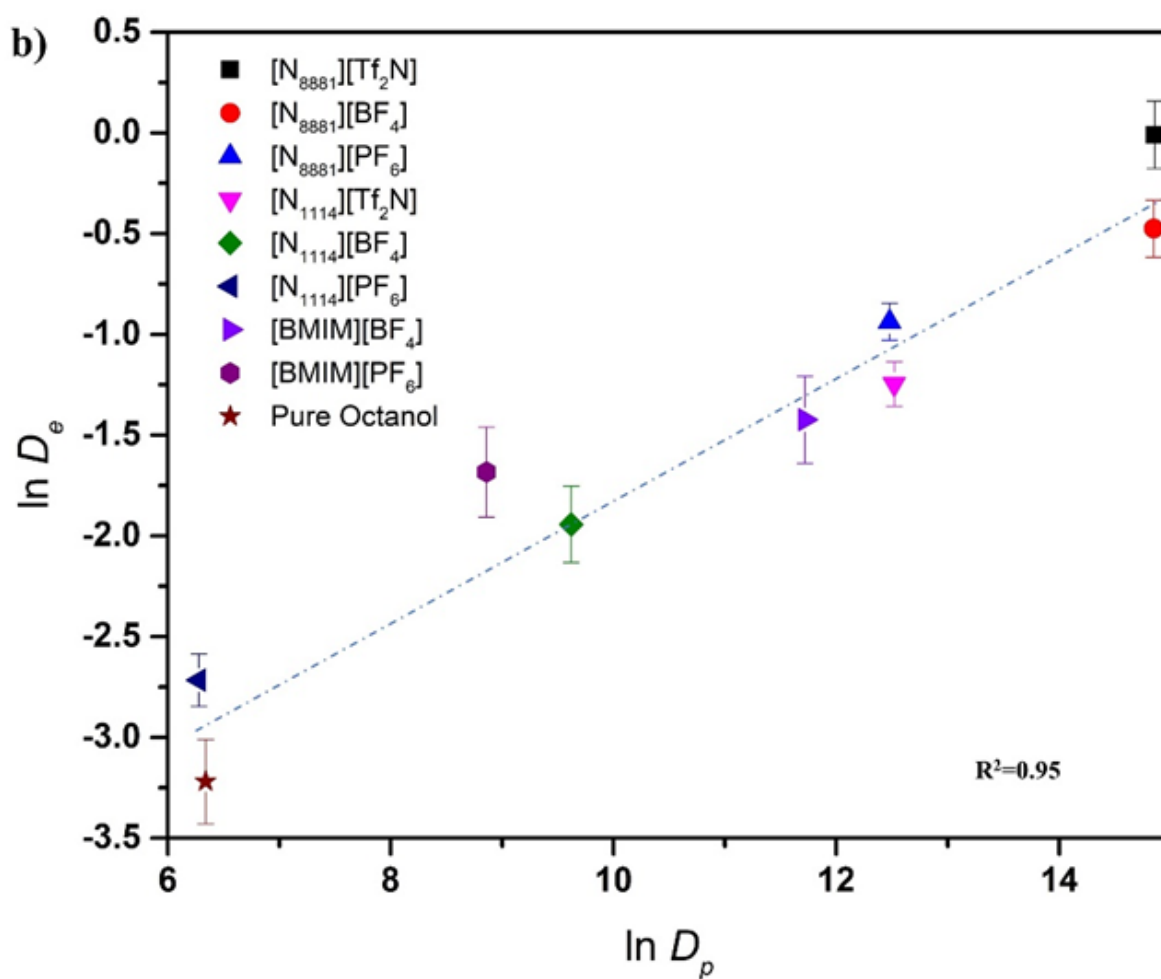
Figure 39 – Comparison of experimental data (lnD_e) with COSMOS-RS model predictions (lnD_p). (a) lnD_p and lnD_e of 8 selected ILs for PFOA extraction; (b) lnD_p and lnD_e for 8 selected ILs for PFOS extraction

To gain a deeper understanding of D_p and D_e, we analyzed the σ-profiles, as shown in Figure 40. a. In the H-bond donor region, PFOA and PFOS generally had very similar σ-profiles, whereas when it came to the non-polar region, it is evident that PFOS was larger than that PFOA. For the polar region, the positive electron distribution of PFOA exceeded 0.0082 e·Å⁻² due to the presence of two equivalent resonance structures in which the negative charge was delocalized over two O atoms. By contrast, for PFOS, the sulfonic acid group lacked stable resonance structures, which made PFOA a stronger H-bond acceptor than PFOS. The σ-profiles can be broken down into misfit (MF) interaction energy, H-bond (HB) interaction energy, and

VdW interaction energy, and the results are shown in Table S7. The dominant interactions for PFOA and PFOS are VdW forces, which are related to the non-polar region. PFOS had a higher VdW interaction energy compared to PFOA, which explained well why D_e and D_p were higher for PFOS than PFOA.

The σ-profile of the cations and anions of ILs were also analyzed. As previously discussed, PFOA and PFOS are strong H-bond acceptors. Accordingly, PFOA and PFOS are stabilized by a positive electron donor, shown on the right side of the σ-profiles. As shown in Figure 40. b, the peaks of $[Tf_2N]^-$ and $[BF_4]^-$ are more positive than those of $[PF_6]^-$. Thus, the extraction efficiency of $[PF_6]^-$ is lower than that of the other two ILs. Notably, as the VdW forces are dominant, cations with σ-profile area in the non-polar region benefit extraction. As a result, the ILs containing $[N_{8881}]^+$ cations showed the highest extraction efficiency among the other three cationic ILs.
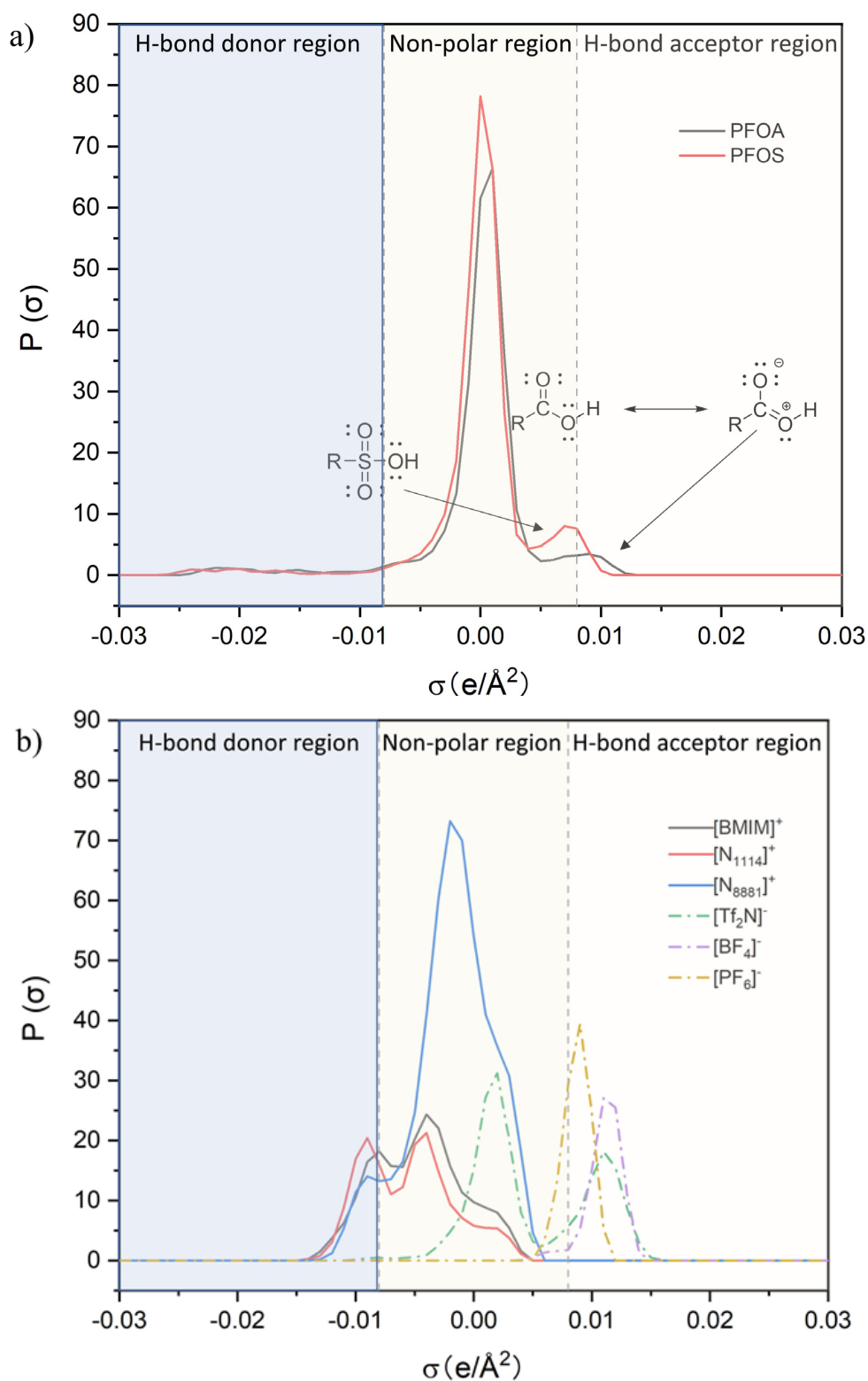
Figure 40 – *σ*-profiles of a) PFOA, PFOS, and b) cations and anions of different ILs. *P(σ)* is the probability distribution of a specific charge density.

7.5   Conclusion

The COSMO-RS method was employed in this work to screen potential ILs to recover PFOA and PFOS from their aqueous solutions. According to the screening results based on the infinite dilution activity coefficient ($\gamma\infty$) calculation, the ILs with H-bond acceptors in both anions and cations are favorable as extractants. 8 ILs with cations of $[N_{8881}]^+$, $[N_{1444}]^+$ and $[BMIM]^+$, and with the anions of $[Tf_2N]^-$, $[BF_4]^-$ and $[PF_6]^-$ were selected for the extraction of PFOA and PFOS. The extraction performance characterized by extraction efficiency, distribution coefficient, and selectivity indicated that the IL with the cation of $[N_{8881}]^+$ given the best separation result in order of $[N_{8881}][Tf_2N] > [Tf_2N][BF_4] > [Tf_2N][PF_6]$, which were consistent with the predicted results using COSMO-RS. Further analysis of the σ-profiles demonstrated that VdW forces play a crucial role in the extraction of PFOS and PFOA, followed by misfit and H-bond interactions. In summary, COSMO-RS is a fast approximation method to screen the suitable ILs for extracting PFACs.

CHAPTER 8. MAJOR CONCLUSIONS AND FUTURE WORKS

8.1 Major conclusions

The key conclusions of this dissertation include:

1. A EAOP-fuel cell energy recovery system can significantly recover the energy by using the hydrogen produced at the cathode chamber, lowering the overall energy consumption. The theatrical energy recovery ratio and the experimental energy recovery ratio are obtained. The optimal operation condition is 3V with BDD as the anode. This result has great significance in guiding future anode electrode design. Improving the conductivity of the electrode at low voltages will be a focus of future work as opposed to excessively increasing the anode's oxygen overpotential.

2. The flow through multiple layer wire mesh anodes fit well with the EAOP-fuel cell energy recovery system. The number of layers of the wire mesh electrodes greatly influences the mass transfer and the overall oxidation efficiency. Three layers of the wire mesh electrode can form a flow-through porous anode structure. The mass transfer has a significant impact on the overall oxidation efficiency. The impact was quantitatively compared with the flow by reactor system.

3. The development of anode materials: Mn_2O_3 as a green and economically friendly compound is chosen for improving the conductivity of the original TiO_2 NTAs. 1) heterojunction structure is successfully formed between the TiO_2 NTAs and deposited Mn_2O_3. 2) The Mn_2O_3 dopant concentration is critical to the overall oxidation

performance. TiO$_2$ NTAs have low conductivity due to their wide bandgap structure. The Mn$_2$O$_3$ is a narrow-band semiconductor that is rich in oxygen vacancies. Therefore, the Mn$_2$O$_3$ TiO$_2$ NTAs heterojunction structure can significantly improve the conductivity. 3) doping the Mn$_2$O$_3$ will narrow down the TiO$_2$ NTAs bandgap leading to poor radical generation.

4. Ti$_4$O$_7$ wire mesh electrode and TiO$_2$ NTAs SnO$_2$/Sb$_2$O$_3$ wire mesh anode are successfully fabricated. Both of the electrodes can successfully oxidize the PFOA. Their defluorination and TOC removal ratios are also obtained and compared with the BDD anode. The results confirm the improved mass transfer effect on the flow through anode configuration.

5. Adding extractants with the quaternary ammonium group can significantly improve the LLE efficiency of PFOA. CTAB or ILs [A336][NTf2] is added in the octanol phase. The optimal pH, extractant concentration, and temperature is obtained. The extraction mechanism is studied by both the density functional theory (DFT) and molecular dynamic (MD) simulation.

6. COSMO-RS screens 1763 ILs for PFOA and PFOS extraction. The infinite dilution activity coefficient (lnγ^{∞}) of PFOA and PFOS in water and ILs are calculated and used for extraction efficiency prediction. The experimental and predicted distribution coefficients are fitted for PFOA and PFOS extraction. The σ-potential profile explains the PFOA and PFOS extraction efficiency difference.

8.2 Future Works

Future research to advance the knowledge of electrochemical oxidation and the development of electrochemical advanced oxidation processes for wastewater treatment may involve the following, based on the existing findings of studies:

1. Improve the anode longevity and reduce the side reaction by PTFE coating. Anode longevity is the key technical indicator for industrial applications that takes up a large portion of the operating cost. Reports show that the electrode coating with PTFE service life lasts longer than the uncoated one. Long-term oxygen evolution on the electrode surface damages the electrode surface due to mechanical stresses. The hydrophobic surface inhibits inner-sphere oxidation to produce O_2, extending the electrode longevity. At the same time, the hydrophobic surface increases efficiency for •OH generation via an outer-sphere process.[191] To be noticed, the effect of PTFE layer thickness on the electrode conductivity and oxidation efficiency needs to be investigated. Moreover, the hydrophobic layer can change the electron transfer mechanism, so the effect on chloride gas generation and bromide gas generation is also of interest. These side effects are undesired during the EAOPs.

2. Further development of advanced anode materials is possible by band gap engineering. Combining machine learning methods and first-principles calculations can accelerate the discovery process for novel heterojunction semiconductors.

3. Surface modification on the Nafion membrane is used in the EAOP-fuel cell energy recovery system. Due to the surface roughness of the anode, the anode does not make good contact with the membrane. Adding the high surface area catalytic graphene is one possible

direction to increase the effectiveness of contact. Modification of surfaces with controlled densities of ligands is also applicable.

4. Using multistage countercurrent extractionto to improve the LLE of PFACs. Select wide electrochemical windows ILs with a high extraction efficiency of PFACs. Conduct the PFACs electrooxidation in ILs. The ILs are an electrolyte additive in the high-energy-density lithium battery field. Therefore, The ILs is stable when the EAOPs is operated in low voltage condition.

APPENDIX A. SUPPORTING INFORMATION FOR CHAPTER 3
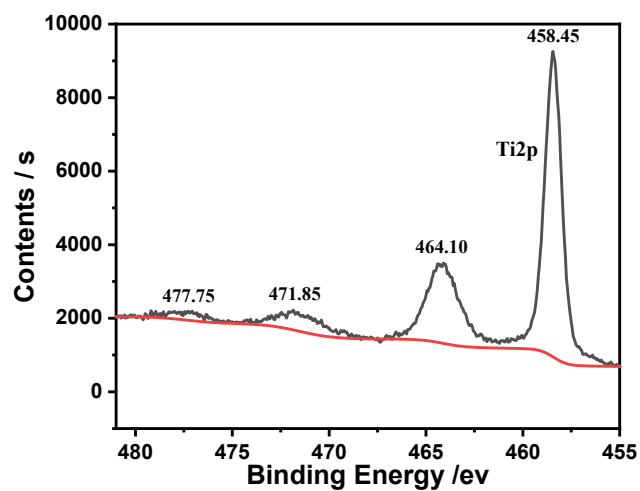
Figure 41 – The XPS of Ti4O7 wire mesh electrode
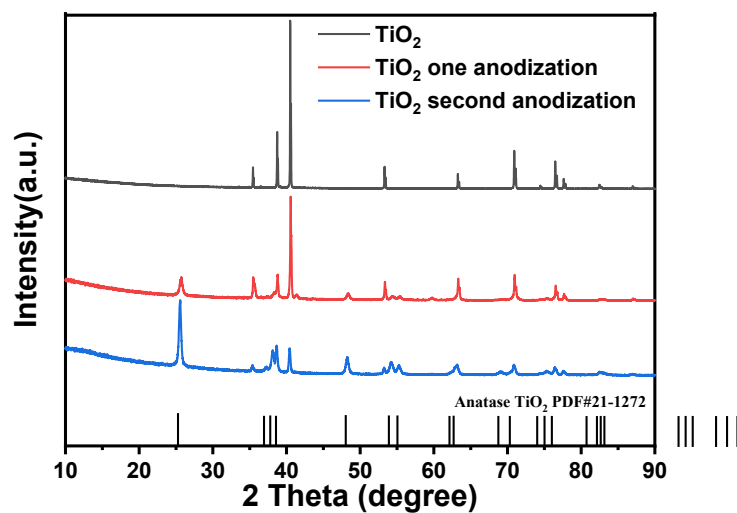
Figure 42 – The XRD of TiO$_2$ NTAs after one and second anodization

Text A.S1.

Wires are assumed to be cylinders with a diameter of dw. As they are woven over and under the other cylinders, the woven wires of the mesh pattern force the cylinders to be curved. As seen in Figure 2, one approximation of this interlaced curvature is a triangle wave. 0.5 dw is deducted from the horizontal length dw + to account for the overlap between mesh wires at the connections. The area of one mesh unit may then be determined and multiplied by the number of units in the mesh nm. The mesh area is then connected to the geometric area, with the resulting ratio being:

$$\frac{A_{mesh}}{A_{flat}} = 0.0031\pi d_w n_m^2 \sqrt{(0.5d_w + d_o)^2 + (2d_w)^2} \tag{1}$$
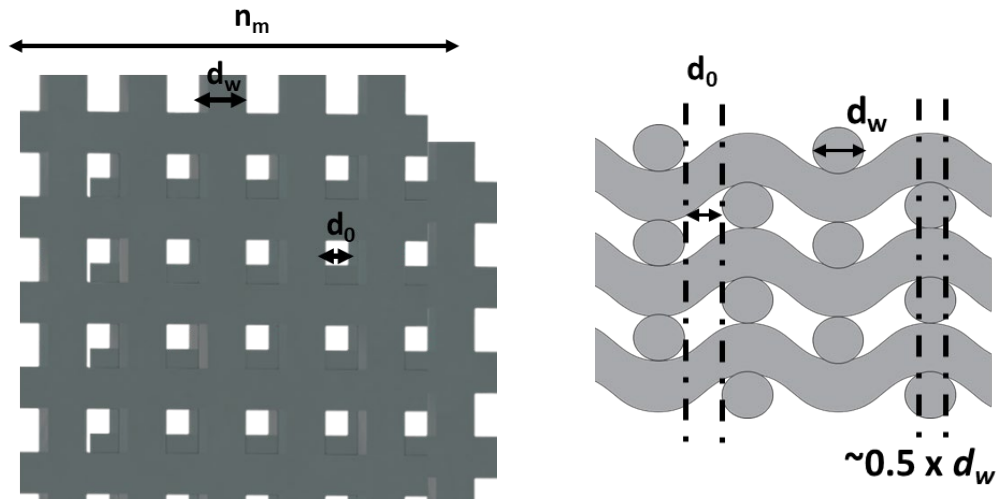
Figure 43 – The sketch of the multiple layer wire mesh electrodes.

Table 10 – The mesh size comparison Chart

Mesh/Inch	do	dw.	Open Area	Thickness
	um	(um)	(%)	(um)
50	300	190	50	190
80	213	100	46	240
100	150	100	43	192
120	128	80	42	150
150	110	60	40	98
183	89	50	38	90
203	75	50	36	93

Figure 44 – The PFOA oxidation profile using the 3 layers Ti_4O_7 wire mesh electrodes and current density time profile (Y axis). The initial PFOA concentration: 50 ppm; Supporting electrolyte: 0.05 M $NaSO_4$.Flow rate: 20 ml/min.
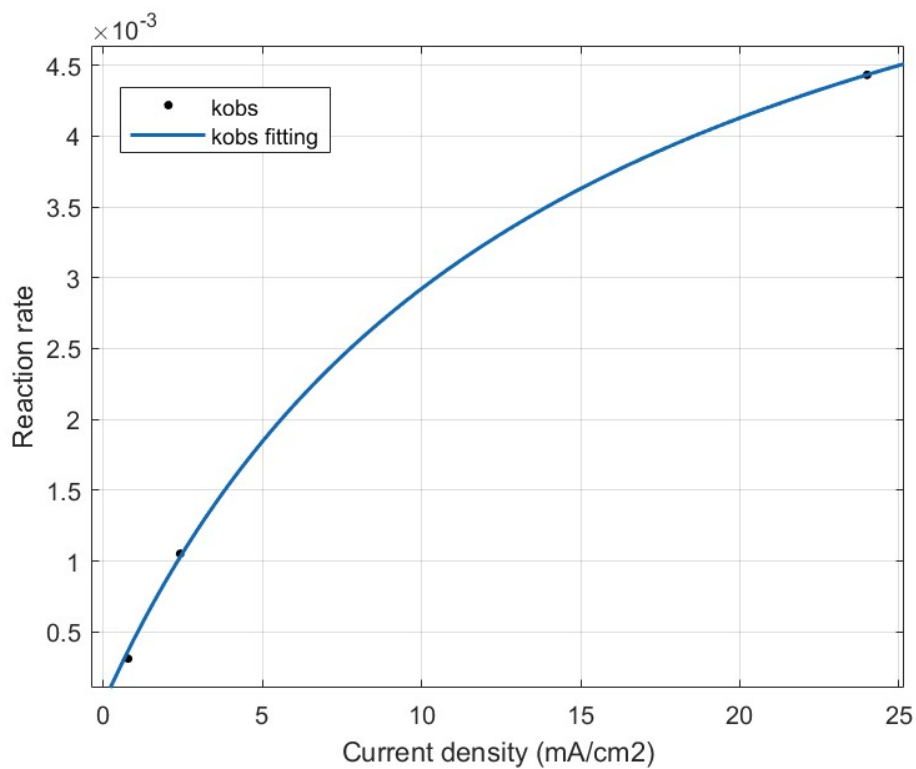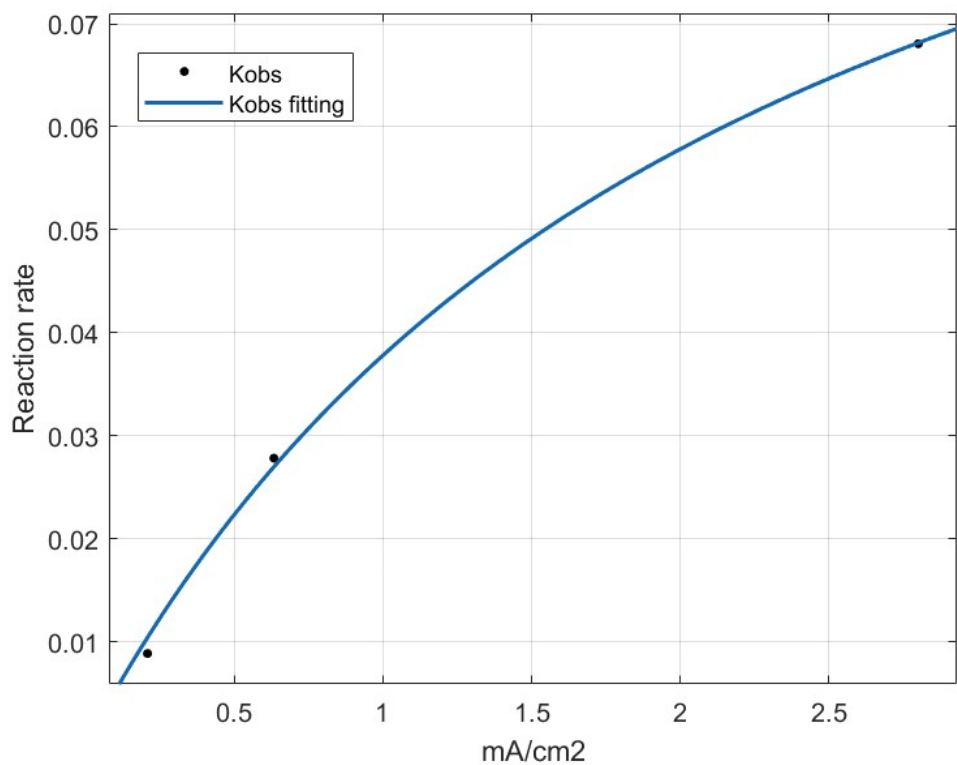
Figure 45 – The fitting of the current and reaction rate based on the mass transfer rate model. a) Ti$_4$O$_7$ b) BDD

APPENDIX B. SUPPORTING INFORMATION FOR CHAPTER 4

Text S1. XANES setup

The radiation was monochromatized by a Si (111) double-crystal monochromator. The intensity of the incident X-rays was monitored by an N_2-filled ion chamber (I_0) in front of the sample. Solid samples were diluted in graphite powder (pelletized as disks of 13 mm diameter with 1mm thickness) and placed in an aluminum sample holder sealed with Kapton tape. The data were collected as fluorescence excitation spectra with a Lytle detector. The reference spectra were recorded in transmission mode using an N_2-filled ionization chamber. All data were collected at room temperature.

Text S2. Details of DFT calculations

All the first principle calculations in this work were performed using the Vienna *Ab initio* Simulation Program (VASP)[1, 2]. The generalized gradient approximation (GGA) in the Perdew-Burke-Ernzerhof (PBE) form was used to treat exchange-correlation effects [3], and the vdW-D3 correction is invoked in all the calculations to account for the dispersion interaction. The kinetic energy cutoff of 500 eV was used for the plane-wave basis sets, and a Monkhorst-Pack k-point mesh with a 7x7×11 and 5x5x5 grid was adopted in the Brillouin Zones for the TiO_2 (space group: C2/m) and Mn_2O_3 (space group: C12/c1), respectively. All the system's atoms were optimized until the total energies converged to below 1×10^{-5} eV and the forces acting on atoms were less than -0.01 eV/Å.

Table 11 – Mn/Ti ratio of MnO$_x$-TiO$_2$ NTAs obtained by ICP-OES

Sample	Mn/Ti (wt %)
0.1_MnO$_x$-TiO$_2$ NTAs	0.039
5_MnO$_x$-TiO$_2$ NTAs	1.380
Bare TiO$_2$ NTAs	/
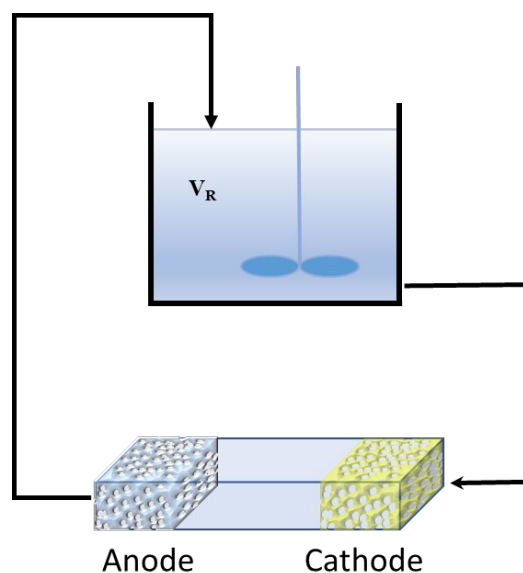
Figure 46 – The schematic diagram of the flow through reactor and the reservoir
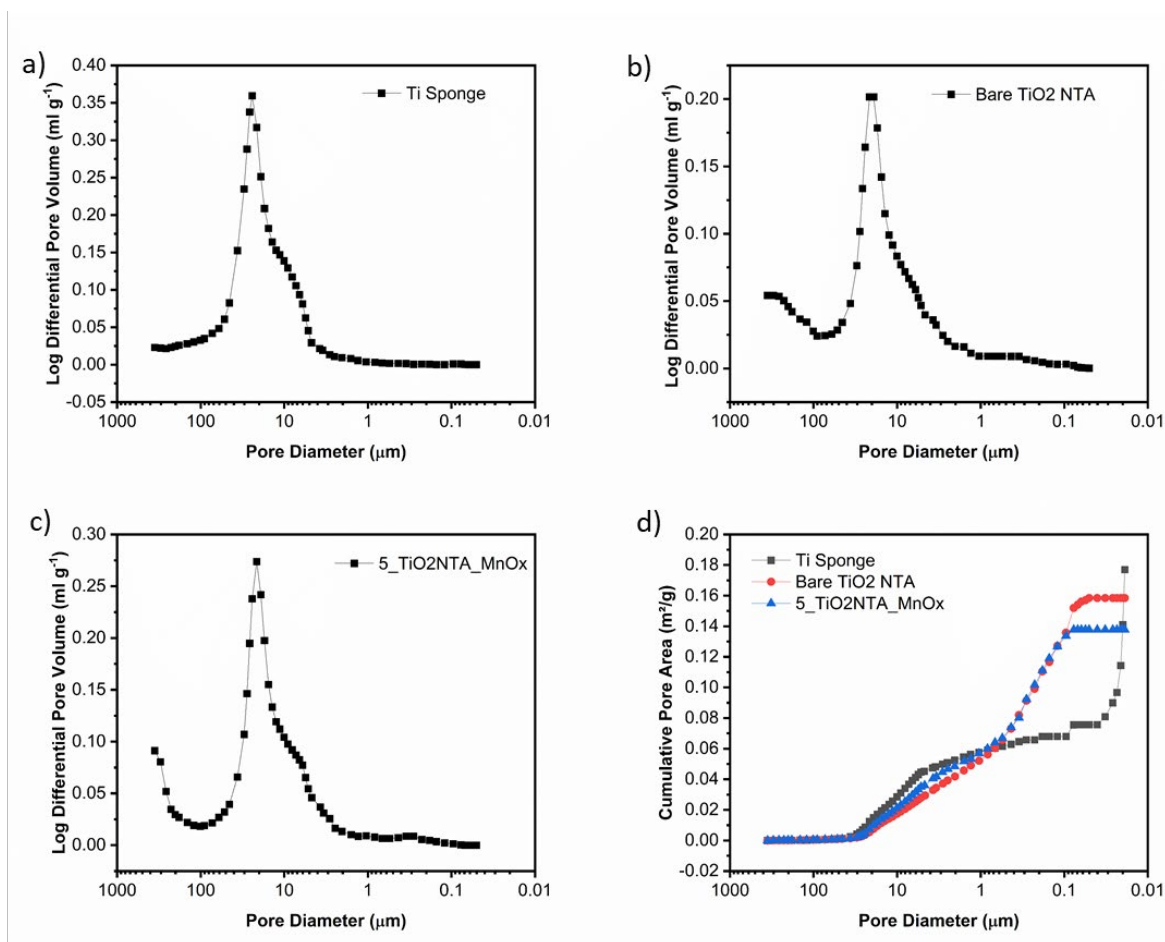
Figure 47 – Hg porosimetry analysis of log differential pore volume of Bare TiO2 NTA 0.1_TiO2NTA_MnOx and 5_TiO2NTA_MnOx (a-c), and cumulative pore area of Bare TiO2 NTA 0.1_TiO2NTA_MnOx and 5_TiO2NTA_MnOx (d).
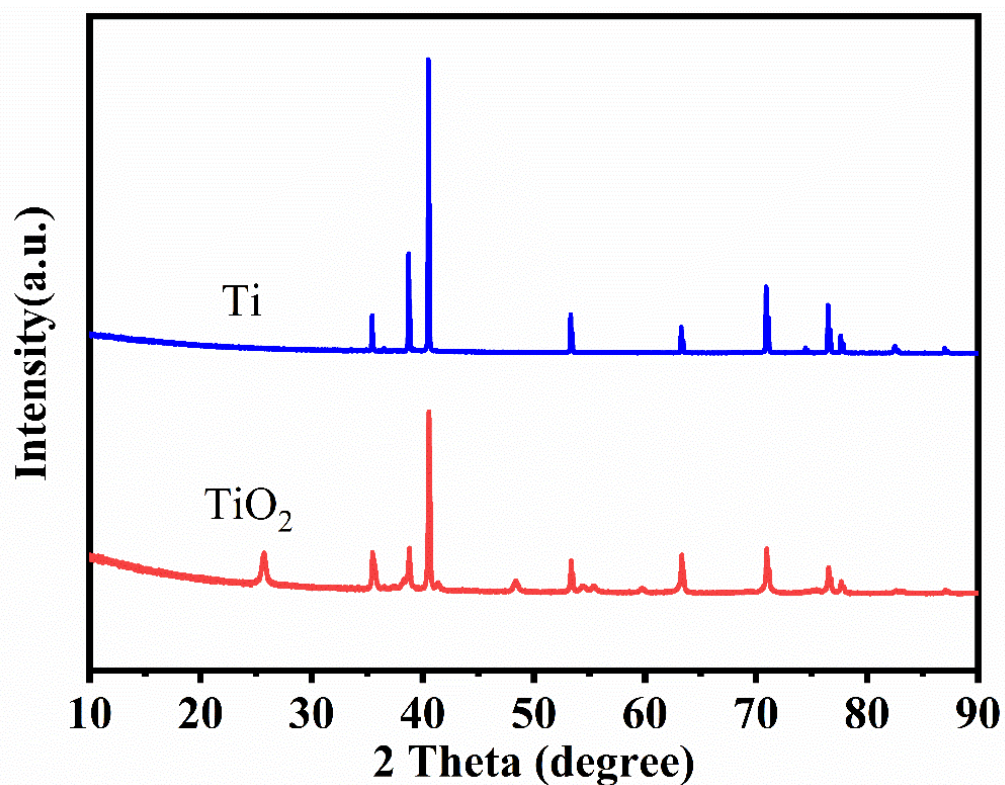
Figure 48 – Mn K-edge X-ray absorption near-edge structure (XANES) spectra of Mn₂O₃-TiO₂ NTAs with Mn foil, MnO, and MnO₂ as references.
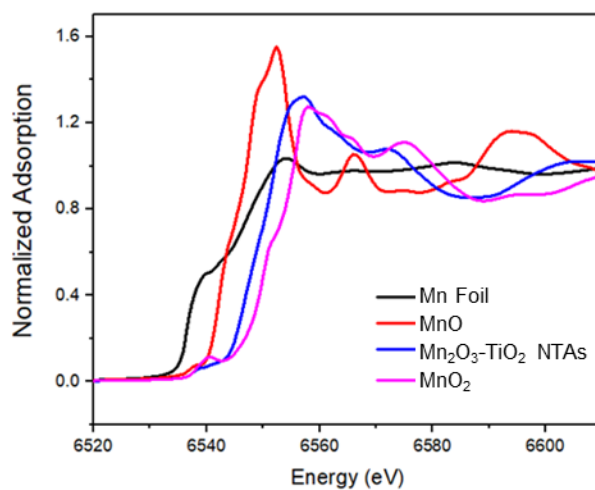
Figure 49 – Mn K-edge X-ray absorption near-edge structure (XANES) spectra of Mn₂O₃-TiO₂ NTAs with Mn foil, MnO, and MnO₂ as references

146
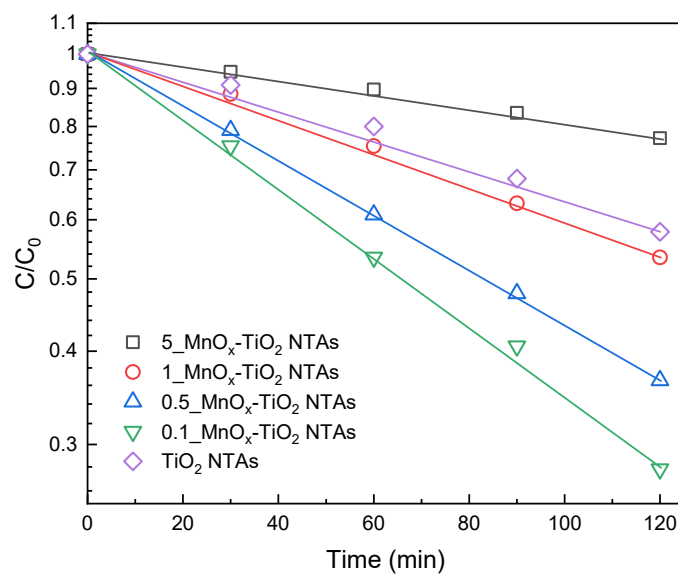
Figure 50 – The solid line represents the pseudo-first-order fitting of the BA degradation in different systems. BA concentration: 20 ppm, flow velocity: 0.08 cm s-1, nominal pore size: 50 um, volume: 100 mL.
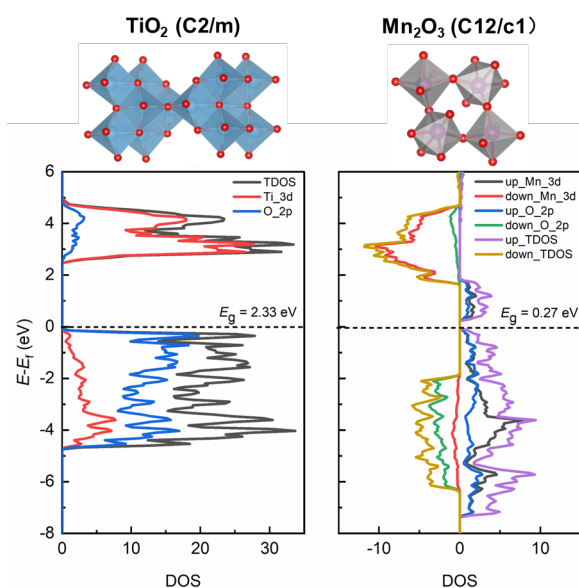
Figure 51 – The DOS of TiO$_2$ and Mn$_2$O$_3$ from the DFT calculations. The band gap for TiO$_2$ and Mn$_2$O$_3$ is 2.33 and 0.27 eV, respectively.

APPENDIX B. SUPPORTING INFORMATION FOR CHAPTER 6

Table 12 – The number of ions (N_{IL}), octanol (N_{oct}), and atoms (N_{MD}) in the system with different concentrations

C_{IL} (mol/L)	N_{IL}	N_{Oct}	N_{MD}
0.001	1	6350	63595
0.0025	2	5080	50990
0.005	3	3810	38385
0.01	6	3810	38670
0.02	12	3810	39240
0.03	18	3810	39810
0.05	30	3810	40950

Table 13 – The extraction percentage of PFOA by extractant + octanol at: extractant = 0.0025 mol·L-1, PFOA = 100 mg·L-1, A/O = 1:1, extraction time = 30 min, and T=298.15 K.

Extractant	Extraction percentage of PFOA (E_{PFOA})		
	First time	**Second time**	**Third time**
[A336] [NTf$_2$]	65.21	53.98	60.37
CTAB	53.81	53.11	54.01

Table 14 – The probability distribution function of the cluster size with the different concentrations of Ils (Ionic liquids).

mol/L Cluster	0.001	0.0025	0.005	0.01	0.02	0.03	0.05
AN	0%	0%	25%	14%	18%	7%	4%
CA	0%	0%	25%	29%	0%	21%	15%
CA+AN	100%	100%	50%	43%	64%	43%	59%
CA+2AN	0%	0%	0%	14%	0%	14%	0%
2CA+AN	0%	0%	0%	0%	9%	0%	11%
2CA+2AN	0%	0%	0%	0%	0%	7%	7%
3CA+2AN	0%	0%	0%	0%	9%	7%	0%
3CA+3AN	0%	0%	0%	0%	0%	0%	4%
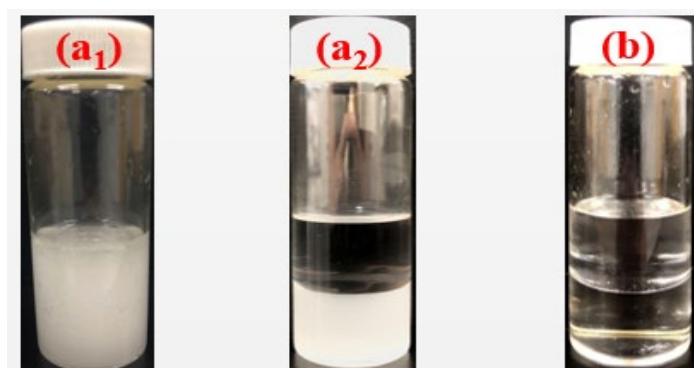
Figure 52 – The liquid-liquid extraction processes with: (a1), the extraction system of CTAB + octanol after the mixture was centrifuged at 4000 rpm for 5 min; (a2), the

extraction system of CTAB + octanol after 24 hours; and (b) the extraction system of [A336][NTf2] + octanol after the mixture was centrifuged at 4000 rpm for 5 min.
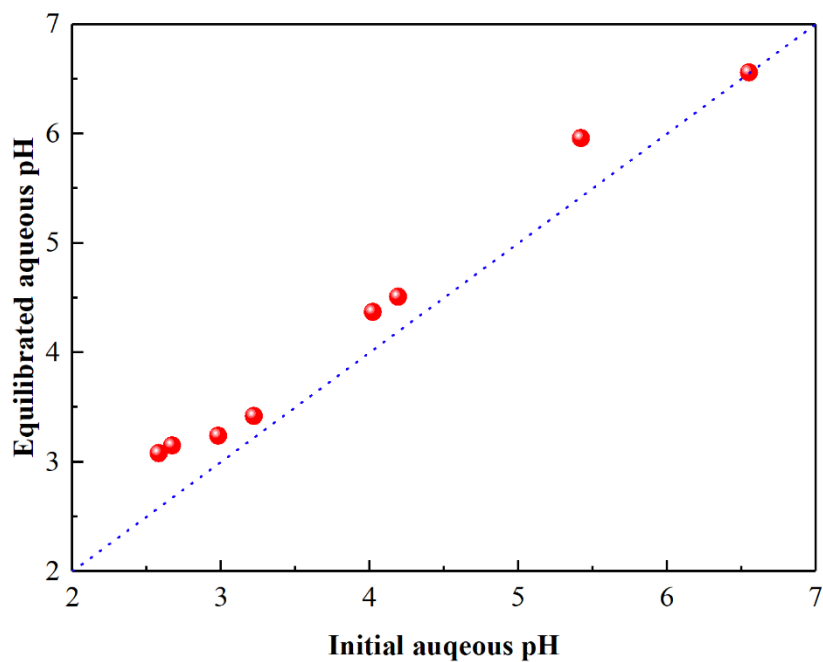
Figure 53 – The initial aqueous pH value vs. the equilibrated aqueous pH.
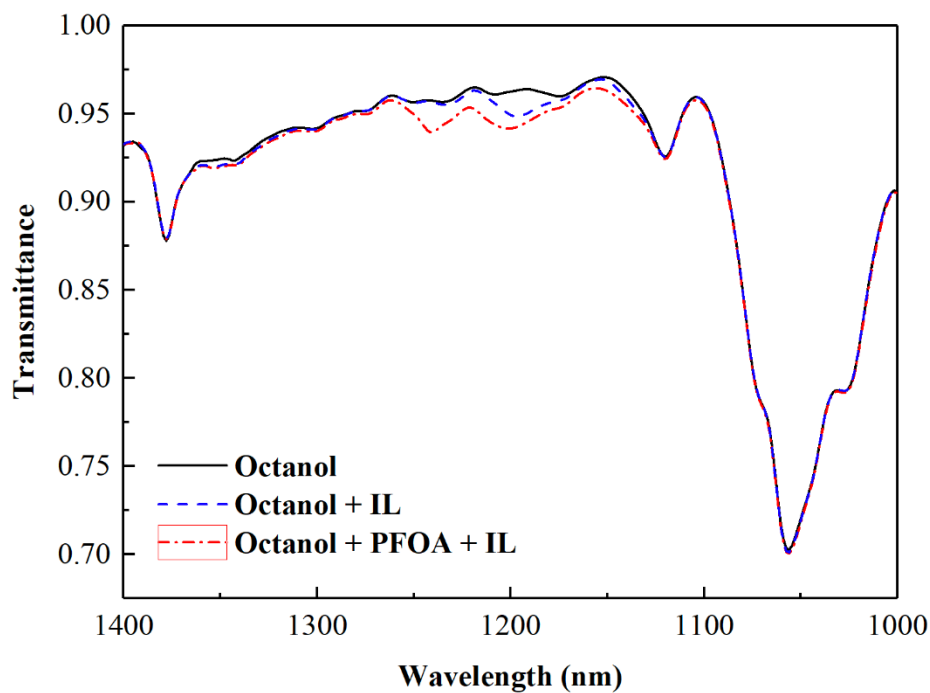
Figure 54 – The FTIR wavelengths of octanol, octanol + PFOA, and octanol + PFOA + IL systems.
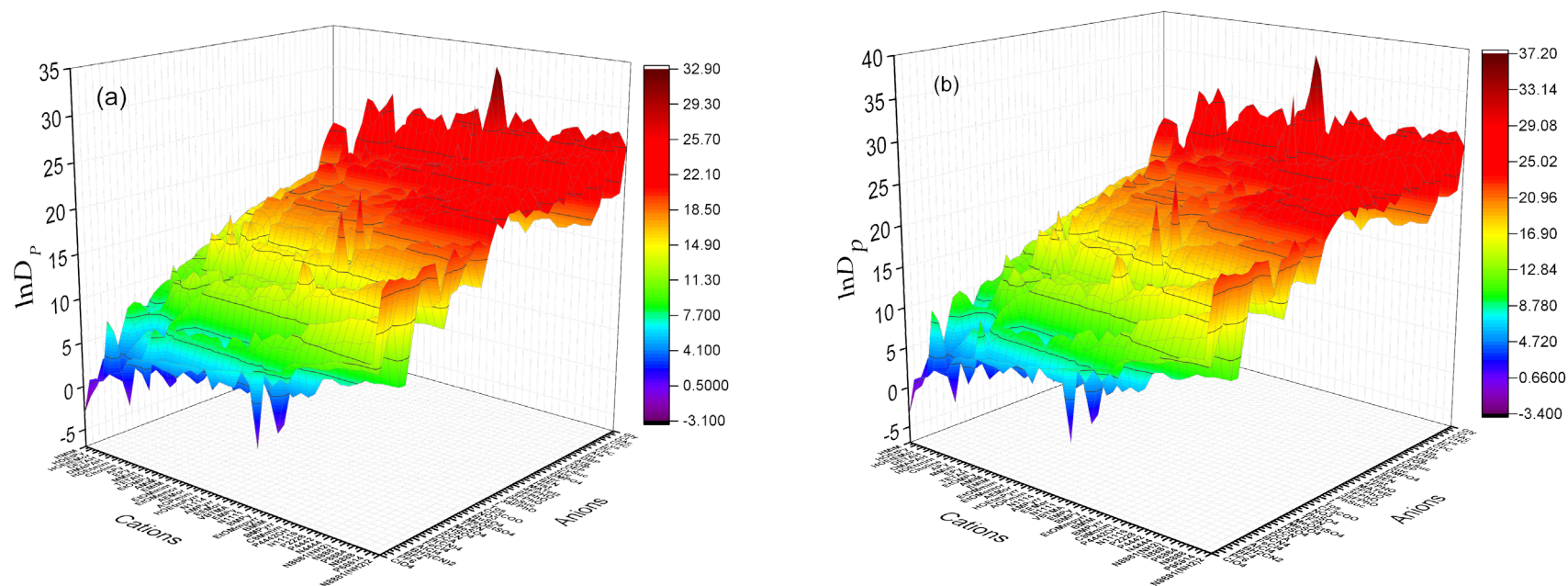
Figure 55 – lnDp of PFOA (a) and PFOS (b) at 298.15 K.
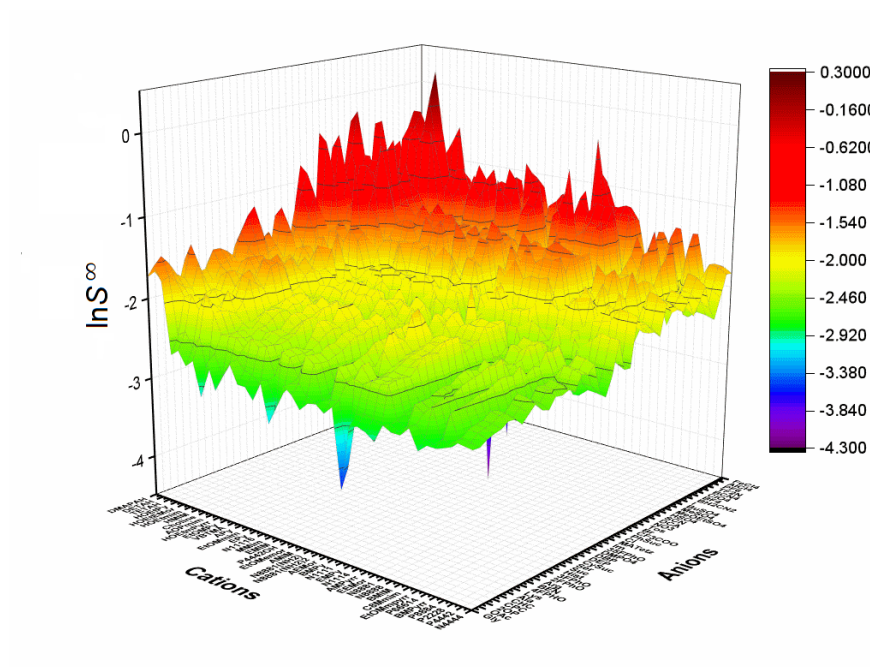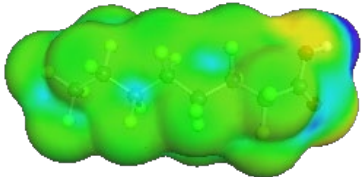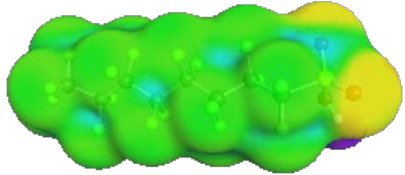
Figure 56 – lnS$^{\infty}$ of PFOA with respect to PFOS at 298.15 K.

Table 15 – Structure of PFOA and PFOS

No.	Full name	Abbreviation	Structure	COSMO σ surface
1	Perfluorooctanoic acid	PFOA		
2	Perfluorooctanesulfonic acid	PFOS		

Surfaces are color-coded: red represents negative partial charge, blue represents positive partial charge, green represents neutral partial charge, and grey represents a missing surface.

Table 16 – Structure of cations
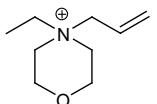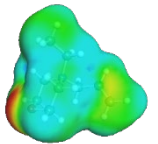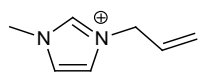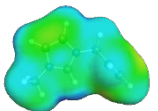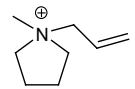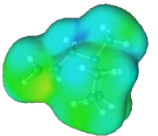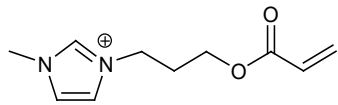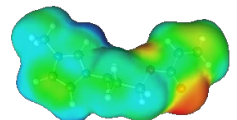
No.	Full name	Abbreviation	Structure	COSMO σ surface
1	4-allyl-4-ethylmorpholinium	AEMor		
2	1-allyl-3-methylimidazolium	AMIM		
3	1-allyl-1-methylpyrrolidinium	AMPyrr		
4	1-acryloyloxypropyl-3-methylimidazolium	AOPmim		

Table 17 continued
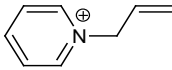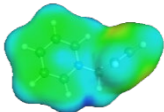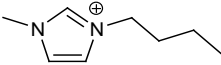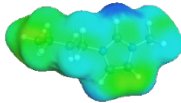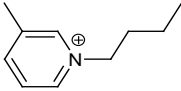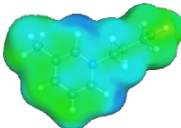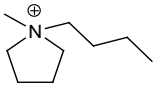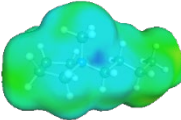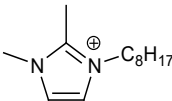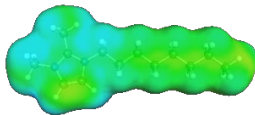
5	N-allyl-pyridinium	APy		
6	1-butyl-3-methylimidazolium	BMIM		
7	1-butyl-3-methypyridinium	BMPy		
8	1-butyl-1-methylpyrrolidinium	BMPyrr		
9	1-octyl-2,3-dimethylimidazolium	C$_8$Mmim		

Table 18 continued
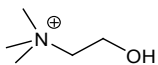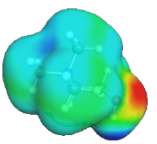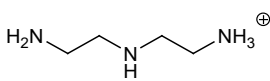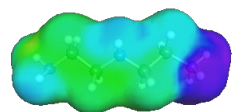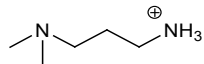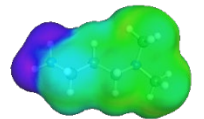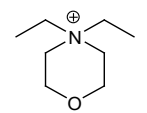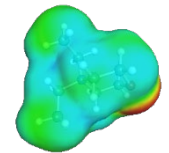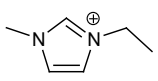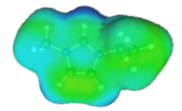
10	Choline	Choline		
11	Diethylenetriamine	DETAH		
12	N,N-dimethyl-1,3-propane diamine	DMAPAH		
13	4,4-diethylmorpholinium	EEMor		
14	1-ethyl-3-methylimidazolium	EMIM		

Table 19 continued
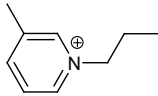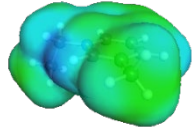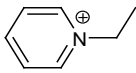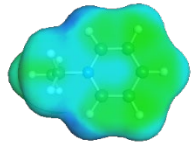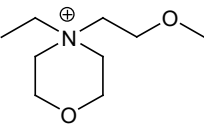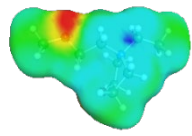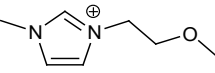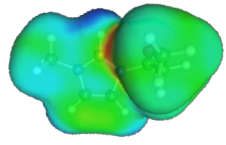
15	1-ethyl-3-methypyridinium	EMPy		
16	N-ethyl-pyridinium	EPy		
17	4-(2-methoxyethyl)-4-ethylmorpholinium	EtOMemor		
18	1-(2-methoxylethyl)-3-methylimidazolium	EtOMmim		

Table 20 continued
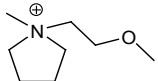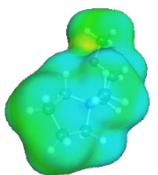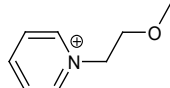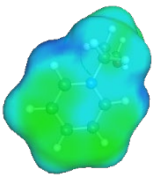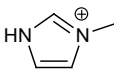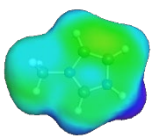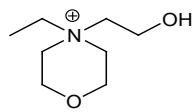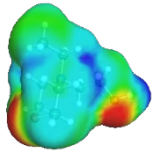
19	1-(2-methoxylethyl)-1-methypyrrolidinium	EtOMmpyrr		
20	N-(2-methoxylethyl)-pyridinium	EtOMpy		
21	3-methylimidazolium	HMIM		
22	4-(2-hydroxylethyl)-4-ethylmorpholinium	HOEtEMor		

Table 21 continued
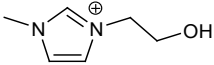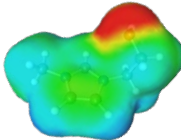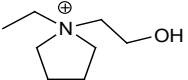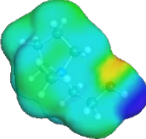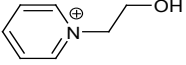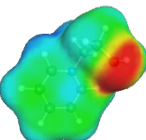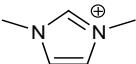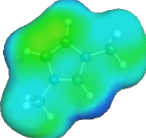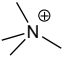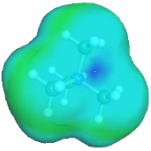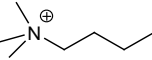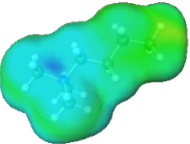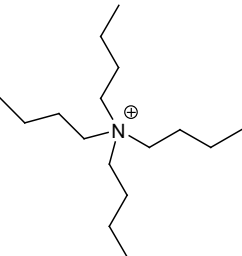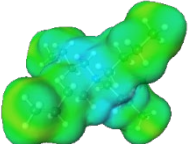
23	1-(2-hydroxylethyl)-3-methylimidazolium	HOEtmim		
24	1-(2-hydroxylethyl)-1-ethypyrrolidinium	HOEtmPyrr		
25	N-(2-hydroxylethyl)-pyridinium	HOEtPy		
26	1,3-dimethylimidazolium	MMim		

Table 22 continued

27	Tetra-methylammonium	N_{1111}		
28	Trimethylbutylammonium	N_{1114}		
29	Tetra-butylammonium	N_{4444}		
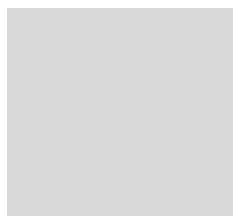
Table 23 continued
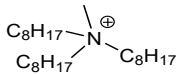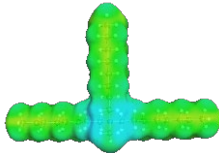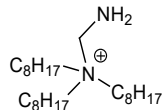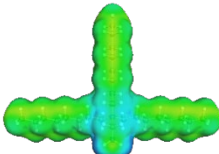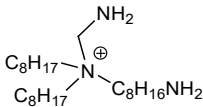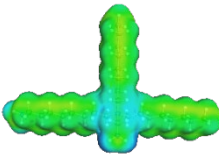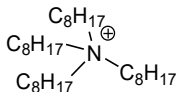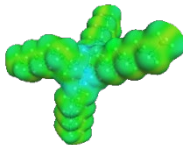
30	Trioctylmethylammonium	N_{8881}	
31	Trioctyl(aminomethane)ammonium	$N_{8881}(NH_2)$	
32	Dioctyl(aminooctane)(aminomethane)ammonium	$N_{8881}(NH_2)_2$	
33	Tetra-octylammonium	N_{8888}	

Table 24 continued
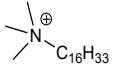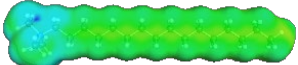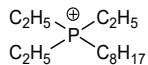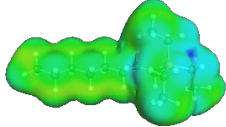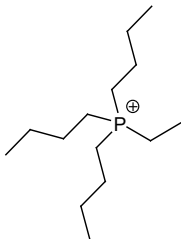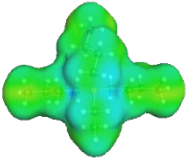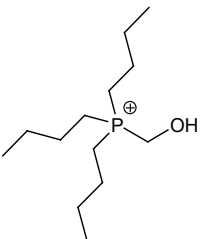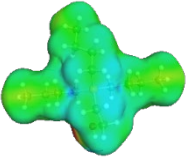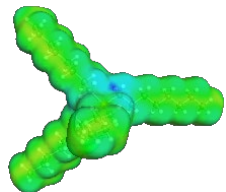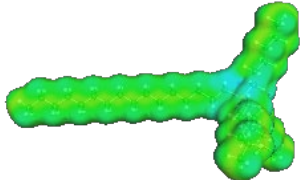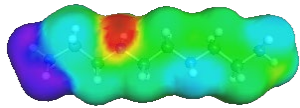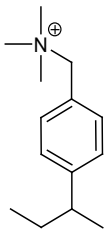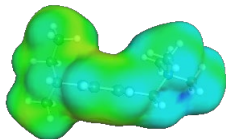
34	Cetyltrimethylammonium	N$_{11116}$		
35	Triethyl(octyl)phosphonium	P$_{2228}$		
36	Tributylethylphosphonium	P$_{4442}$		
37	Tributyl-(2-hydroxylethyl)phosphonium	P$_{4442}$OH		

Table 25 continued

38	Trioctylethylphosphonium	P$_{8884}$		
39	Trihexyl(tetradecyl)phosphonium	P$_{66614}$		
40	Triethylenetetramine	TETAH		

No.	Full name	Abbreviation	Structure	COSMO σ surface
41	Vinylbenzyltrimethylammonium	VBTMA		

Table 26 – Structure of anions
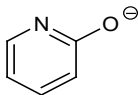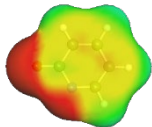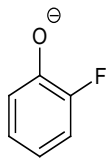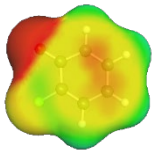
No.	Full name	Abbreviation	Structure	COSMO σ surface
1	2-hydroxylpyridium	2-OP		
2	2-fluorophenolate	2F-PhO		

Table 27 continued

3	3-fluorophenolate	3F-PhO		
4	4-fluorophenolate	4F-PhO		
5	3,5-difluorophenolate	3,5F-PhO		
6	L-alaninate	Ala		
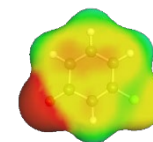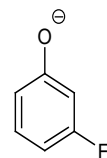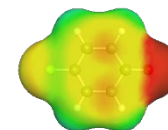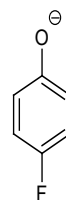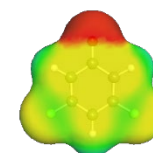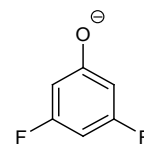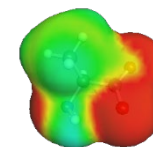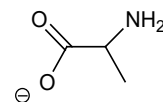
Table 28 continued
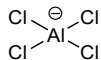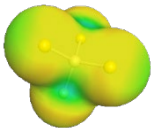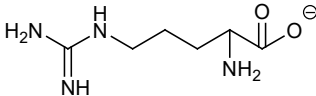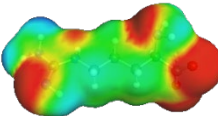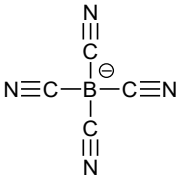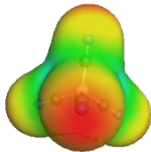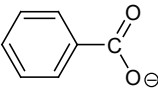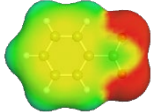
7	Tetrachloroaluminate	AlCl$_4$		
8	L-arginate	Arg		
9	Tetracyanoborate	B(CN)$_4$		
10	Benzoate	BEN		

Table 29 continued
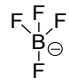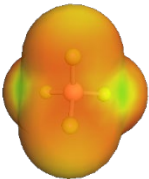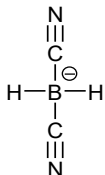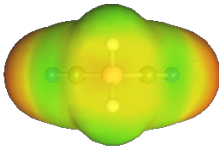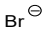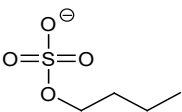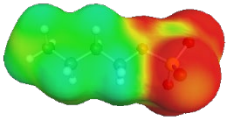
11	Tetrafluoroborate	BF_4		
12	Dihydroboronium	$BH_2(CN)_2$		
13	Bromide	Br		
14	Butylsulfate	$BuSO_4$		

Table 30 continued
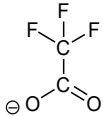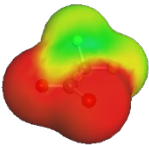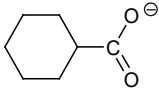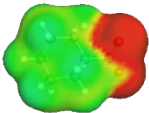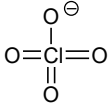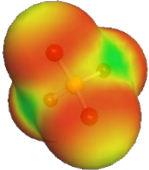
15	Trifluoroacetate	CF₃COO		
16	Cyclohexanecarboxylate	CHC		
17	Cloride	Cl		
18	Perchlorate	ClO₄		

Table 31 continued
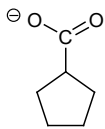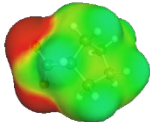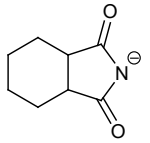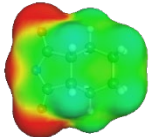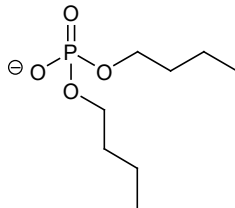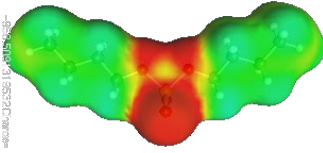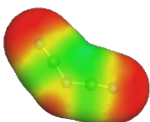
19	Cyclopentanecarboxylate	CPC		
20	1,2-cyclohexanedicarboximide	Cy-suc		
21	Dibutylphosphate	DBP		
22	Dicyanamide	DCA	$N\equiv C-\overset{\ominus}{N}-C\equiv N$	

Table 32 continued

23	Diethylphosphate	DEP		
24	Dimethylphosphate	DMPO$_4$		
25	Tetrachloroferrate	FeCl$_4$		
26	L-glycinate	Gly		

Table 33 continued
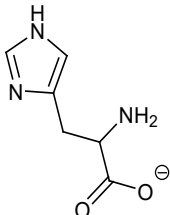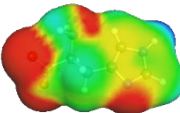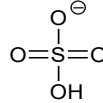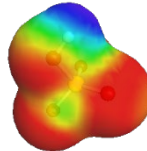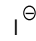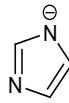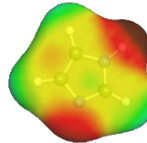
27	L-histidinate	Hist		
28	Hydrogensulfate	HSO$_4$		
29	Iodide	I		
30	Imidazole	Im		

Table 34 continued
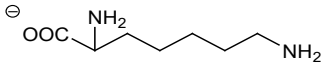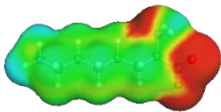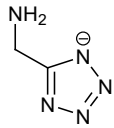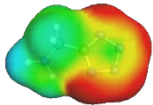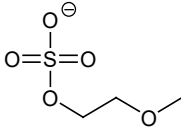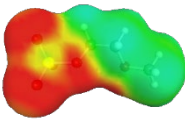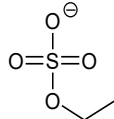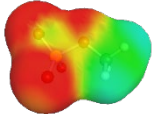
31	L-lysinate	Lys		
32	5-(aminomethyl)-2H-tetrazole	MA-Tetz		
33	Methoxyethylsulfate	MeOEtSO$_4$		
34	Methylsulfate	MeSO$_4$		

Table 35 continued
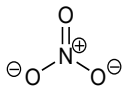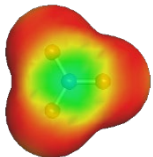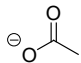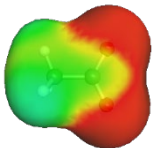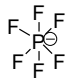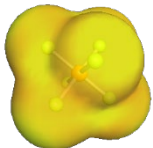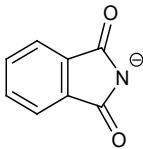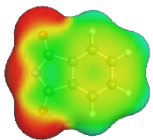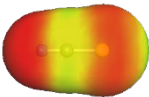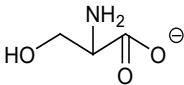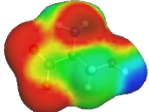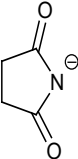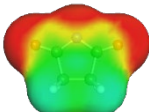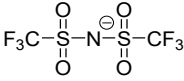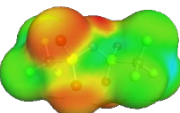
35	Nitrate	NO_3		
36	Acetate	OAc		
37	Hexafluorophosphate	PF_6		
38	O-phthalimide	Ph-suc		

Table 36 continued

39	Thiocyanate	SCN		
40	L-serinate	Ser		
41	Succinimido	Suc		
42	Bis(trifluoromethylsulfonyl)amide	Tf$_2$N		

| 43 | Toluene-4-sulfonate | Tos | | |
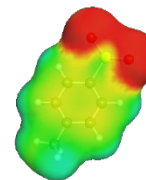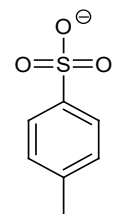
Table 37 – The detailed information of chemicals used in this work

No.	Chemicals	Purity (%)	Water content (%)	Supplier
1	$[N_{8881}][Tf_2N]$	98.50	0.04	Lanzhou Institute of Chemical Physics
2	$[N_{8881}][BF_4]$	98.50	0.12	
3	$[N_{8881}][PF_6]$	99.00	0.19	
4	$[N_{1114}][Tf_2N]$	99.00	0.05	Shanghai Aladdin Biochemical Technology Co., Ltd.
5	$[N_{1114}][BF_4]$	99.00	0.12	
6	$[N_{1114}][PF_6]$	99.00	0.08	
7	$[BMIM][BF_4]$	99.00	0.07	
8	$[BMIM][PF_6]$	99.00	0.05	
9	Pure Octanol	99.99	0.04	Sinopharm Chemical Reagent Co., Ltd.
10	PFOA	98.50	-	Shanghai Aladdin Biochemical Technology Co., Ltd.
11	PFOS	98.50	-	

REFERENCES

1. Torres, N.H., et al., *Environmental aspects of hormones estriol, 17β-estradiol and 17α-ethinylestradiol: Electrochemical processes as next-generation technologies for their removal in water matrices.* Chemosphere, 2021. **267**: p. 128888.

2. Chaplin, B.P., *Critical review of electrochemical advanced oxidation processes for water treatment applications.* Environmental Science: Processes & Impacts, 2014. **16**(6): p. 1182-1203.

3. Moreira, F.C., et al., *Electrochemical advanced oxidation processes: A review on their application to synthetic and real wastewaters.* Applied Catalysis B: Environmental, 2017. **202**: p. 217-261.

4. Suty, H., C. De Traversay, and M. Cost, *Applications of advanced oxidation processes: Present and future*, in *Water Science and Technology*. 2004. p. 227-233.

5. Chong, M.N., et al., *Feasibility study on the application of advanced oxidation technologies for decentralised wastewater treatment.* Journal of Cleaner Production, 2012. **35**: p. 230-238.

6. Kaufman, G.B., *Inorganic chemistry: principles of structure and reactivity, (huheey, james e.; keiter, ellen a.; keiter, richard l.).* 1993, ACS Publications.

7. *COIL-8: Ionic liquids for tomorrow.* Green Energy & Environment, 2020. **5**(2): p. 121.

8. Dong, K., F. Huo, and S. Zhang, *Thermodynamics at microscales： 3D→2D, 1D and 0D.* Green Energy & Environment, 2020. **5**(3): p. 251-258.

9. Dong, K., et al., *Multiscale Studies on Ionic Liquids.* Chemical Reviews, 2017. **117**(10): p. 6636-6695.

10. Sun, W., et al., *Protic vs aprotic ionic liquid for CO2 fixation: A simulation study.* Green Energy & Environment, 2020. **5**(2): p. 183-194.

11. Buxton, G.V., et al., *Critical Review of rate constants for reactions of hydrated electrons, hydrogen atoms and hydroxyl radicals (·OH/·O− in Aqueous Solution.* Journal of Physical and Chemical Reference Data, 1988. **17**(2): p. 513-886.

12. Bachman, B.F., et al., *Detection of Aqueous Solvated Electrons Produced by Photoemission from Solids Using Transient Absorption Measurements.* ACS Measurement Science Au, 2022. **2**(1): p. 46-56.

13. Daily, R. and D. Minakata, *Reactivities of hydrated electrons with organic compounds in aqueous-phase advanced reduction processes.* Environmental Science: Water Research & Technology, 2022. **8**(3): p. 543-574.

14. Garcia-Rodriguez, O., et al., *Electrochemical treatment of highly concentrated wastewater: A review of experimental and modeling approaches from lab- to full-scale.* Critical Reviews in Environmental Science and Technology, 2022. **52**(2): p. 240-309.

15. Shao, M., et al., *Recent Advances in Electrocatalysts for Oxygen Reduction Reaction.* Chemical Reviews, 2016. **116**(6): p. 3594-3657.

16. Bard, A., *Standard potentials in aqueous solution*. 2017: Routledge.

17. Meng, X., et al., *Development of a Three-Dimensional Electrochemical System Using a Blue TiO2/SnO2-Sb2O3 Anode for Treating Low-Ionic-Strength Wastewater.* Environmental Science and Technology, 2019. **53**(23): p. 13784-13793.

18. Carper, J., *The CRC Handbook of Chemistry and Physics.* Library Journal, 1999. **124**(10): p. 192-+.

19. Scheepers, F., et al., *Temperature optimization for improving polymer electrolyte membrane-water electrolysis system efficiency.* Applied Energy, 2021. **283**: p. 116270.

20. Barbir, F., *PEM Fuel Cells: Theory and Practice.* Pem Fuel Cells: Theory and Practice. 2005. 1-433.

21. Srikanth, V.V.S.S., P. Sampath Kumar, and V.B. Kumar, *A Brief Review on the <i>In Situ</i> Synthesis of Boron-Doped Diamond Thin Films.* International Journal of Electrochemistry, 2012. **2012**: p. 218393.

22. Espinoza, L.C., et al., *Effect of the sp3/sp2 Ratio in Boron‐Doped Diamond Electrodes on the Degradation Pathway of Aniline by Anodic Oxidation.* ChemElectroChem, 2019. **6**(18): p. 4801-4810.

23. Ristein, J., *Physics. Surface transfer doping of semiconductors.* Science, 2006. **313**(5790): p. 1057-8.

24. Kavan, L., et al., *Boron-doped diamond electrodes: electrochemical, atomic force microscopy and Raman study towards corrosion-modifications at nanoscale.* Electrochimica Acta, 2015. **179**: p. 626-636.

25. Li, X., H. Xu, and W. Yan, *Fabrication and characterization of PbO2 electrode modified with polyvinylidene fluoride (PVDF).* Applied Surface Science, 2016. **389**: p. 278-286.

26. Zhou, Q., et al., *Application of lead oxide electrodes in wastewater treatment: A review.* Science of The Total Environment, 2022. **806**: p. 150088.

27. Elaissaoui, I., et al., *Effect of coating method on the structure and properties of a novel PbO2 anode for electrochemical oxidation of Amaranth dye.* Chemosphere, 2019. **217**: p. 26-34.

28. Guo, D., C. Robinson, and J.E. Herrera, *Role of Pb (II) defects in the mechanism of dissolution of plattnerite (β-PbO2) in water under depleting chlorine conditions.* Environmental science & technology, 2014. **48**(21): p. 12525-12532.

29. Watts, R.J., et al., *Performance comparison of tin oxide anodes to commercially available dimensionally stable anodes.* Water environment research, 2008. **80**(6): p. 490-496.

30. Ping, Y., G. Galli, and W.A. Goddard III, *Electronic structure of IrO2: the role of the metal d orbitals.* The Journal of Physical Chemistry C, 2015. **119**(21): p. 11570-11577.

31. Gong, H., et al., *The synergetic effect of dual co-catalysts on the photocatalytic activity of square-like WO3 with different exposed facets.* RSC Advances, 2017. **7**(31): p. 19019-19025.

32. Ganose, A.M. and D.O. Scanlon, *Band gap and work function tailoring of SnO2 for improved transparent conducting ability in photovoltaics.* Journal of Materials Chemistry C, 2016. **4**(7): p. 1467-1475.

33. He, T., et al., *Surface Effect and Band-Gap Oscillation of TiO2 Nanowires and Nanotubes.* The Journal of Physical Chemistry C, 2011. **115**(28): p. 13837-13843.

34. Chen, M., et al., *Development of a highly efficient electrochemical flow -through anode based on inner in -site enhanced TiO2-nanotubes array.* Environment International, 2020. **140**.

35. Zaky, A.M. and B.P. Chaplin, *Porous substoichiometric TiO2 anodes as reactive electrochemical membranes for water treatment.* Environ Sci Technol, 2013. **47**(12): p. 6554-63.

36. Le, T.X.H., et al., *Energy-Efficient Electrochemical Oxidation of Perfluoroalkyl Substances Using a Ti4O7 Reactive Electrochemical Membrane Anode.* Environmental Science & Technology Letters, 2019. **6**(8): p. 504-510.

37. Lin, H., et al., *Defect Engineering on a Ti4O7 Electrode by Ce(3+) Doping for the Efficient Electrooxidation of Perfluorooctanesulfonate.* Environ Sci Technol, 2021. **55**(4): p. 2597-2607.

38.   Ma, Q., et al., *Zeolitic imidazolate framework-8 film coated stainless steel meshes for highly efficient oil/water separation.* Chemical Communications, 2018. **54**(44): p. 5530-5533.

39.   Al-Mamun, M.R., S. Kader, and M.S. Islam, *Solar-TiO2 immobilized photocatalytic reactors performance assessment in the degradation of methyl orange dye in aqueous solution.* Environmental Nanotechnology, Monitoring & Management, 2021. **16**: p. 100514.

40.   Xu, L., et al., *Effective degradation of aqueous carbamazepine on a novel blue-colored TiO2 nanotube arrays membrane filter anode.* Journal of Hazardous Materials, 2021. **402**: p. 123530.

41.   Liu, Y., et al., *Recent advances on electroactive CNT-based membranes for environmental applications: The perfect match of electrochemistry and membrane separation.* Chinese Chemical Letters, 2020. **31**(10): p. 2539-2548.

42.   Li, H., et al., *Periodic porous 3D boron-doped diamond electrode for enhanced perfluorooctanoic acid degradation.* Separation and Purification Technology, 2022. **297**: p. 121556.

43.   Wang, C., et al., *Enhanced perfluorooctane acid mineralization by electrochemical oxidation using Ti3+ self-doping TiO2 nanotube arrays anode.* Chemosphere, 2022. **286**: p. 131804.

44.   Qian, Y., et al., *Perfluorooctanoic Acid Degradation Using UV-Persulfate Process: Modeling of the Degradation and Chlorate Formation.* Environmental Science and Technology, 2016. **50**(2): p. 772-781.

45.   Bentel, M.J., et al., *Enhanced Degradation of Perfluorocarboxylic Acids (PFCAs) by UV/Sulfite Treatment: Reaction Mechanisms and System Efficiencies at pH 12.* Environmental Science and Technology Letters, 2020. **7**(5): p. 351-357.

46.   Arias, E.V., M. Mallavarapu, and R. Naidu, *Identification of the source of PFOS and PFOA contamination at a military air base site.* Environ Monit Assess, 2015. **187**(1): p. 4111.

47.   Javed, H., et al., *Discerning the inefficacy of hydroxyl radicals during perfluorooctanoic acid degradation.* Chemosphere, 2020. **247**: p. 125883.

48.   Fang, C., M. Megharaj, and R. Naidu, *Electrochemical Advanced Oxidation Processes (EAOP) to degrade per-and polyfluoroalkyl substances (PFASs).* Journal of Advanced Oxidation Technologies, 2017. **20**(2).

49.   Uwayezu, J.N., et al., *Electrochemical degradation of per- and poly-fluoroalkyl substances using boron-doped diamond electrodes.* Journal of Environmental Management, 2021. **290**: p. 112573.

50. Wang, G., et al., *Synthesis, microstructural characterization, and electrochemical performance of novel rod-like Ti4O7 powders.* Journal of Alloys and Compounds, 2017. **704**: p. 18-25.

51. Bursill, L. and B. Hyde, *Crystallographic shear in the higher titanium oxides: Structure, texture, mechanisms and thermodynamics.* Progress in solid state chemistry, 1972. **7**: p. 177-253.

52. Ioroi, T., et al., *Stability of Corrosion-Resistant Magnéli-Phase Ti[sub 4]O[sub 7]-Supported PEMFC Catalysts at High Potentials.* Journal of The Electrochemical Society, 2008. **155**(4): p. B321.

53. Lin, H., et al., *Development of macroporous Magnéli phase Ti4O7 ceramic materials: As an efficient anode for mineralization of poly- and perfluoroalkyl substances.* Chemical Engineering Journal, 2018. **354**: p. 1058-1067.

54. Macpherson, J.V., *A practical guide to using boron doped diamond in electrochemical research.* Phys Chem Chem Phys, 2015. **17**(5): p. 2935-49.

55. Huo, K.F., et al., *Fabrication, modification, and biomedical applications of anodized TiO2 nanotube arrays.* Rsc Advances, 2014. **4**(33): p. 17300-17324.

56. Chen, M., et al., *Electrochemical oxidation of reverse osmosis concentrates using enhanced TiO2-NTA/SnO2-Sb anodes with/without PbO2 layer.* Chemical Engineering Journal, 2020. **399**: p. 10.

57. Chen, M., et al., *Electrochemical oxidation of reverse osmosis concentrates using enhanced TiO2-NTA/SnO2-Sb anodes with/without PbO2 layer.* Chemical Engineering Journal, 2020. **399**.

58. Guan, D.X., et al., *In situ measurement of perfluoroalkyl substances in aquatic systems using diffusive gradients in thin-films technique.* Water Res, 2018. **144**: p. 162-171.

59. O'Hern, T. and J. Torczynski, *Reynolds number dependence of the drag coefficient for laminar flow through fine-scale photoetched screens.* Experiments in fluids, 1993. **15**(1): p. 75-81.

60. Wakeland, R.S. and R.M. Keolian, *Measurements of Resistance of Individual Square-Mesh Screens to Oscillating Flow at Low and Intermediate Reynolds Numbers.* Journal of Fluids Engineering, 2003. **125**(5): p. 851-862.

61. Huang, D., et al., *Amorphous Pd-loaded Ti4O7 electrode for direct anodic destruction of perfluorooctanoic acid.* Environmental Science & Technology, 2020. **54**(17): p. 10954-10963.

62.   English, J.T. and D.P. Wilkinson, *The Superior Electrical Conductivity and Anodic Stability of Vanadium-Doped Ti$_4$O$_7$*. Journal of The Electrochemical Society, 2021. **168**(10): p. 103509.

63.   Gu, Z., et al., *Exploring the Nanotoxicology of MoS2: A Study on the Interaction of MoS2 Nanoflakes and K+ Channels*. ACS Nano, 2018. **12**(1): p. 705-717.

64.   Sirés, I., et al., *Electrochemical advanced oxidation processes: today and tomorrow. A review*. Environmental Science and Pollution Research, 2014. **21**(14): p. 8336-8367.

65.   Xie, R.Z., et al., *Electrochemical oxidation of ofloxacin using a TiO2-based SnO2-Sb/polytetrafluoroethylene resin-PbO2 electrode: Reaction kinetics and mass transfer impact*. Applied Catalysis B-Environmental, 2017. **203**: p. 515-525.

66.   He, Y.P., et al., *Recent developments and advances in boron-doped diamond electrodes for electrochemical oxidation of organic pollutants*. Separation and Purification Technology, 2019. **212**: p. 802-821.

67.   Zhou, F.Q., et al., *BiVO4 nanowires decorated with CdS nanoparticles as Z-scheme photocatalyst with enhanced H2 generation*. Applied Catalysis B: Environmental, 2017. **201**: p. 77-83.

68.   Ghosh, U. and A. Pal, *Graphitic carbon nitride based Z scheme photocatalysts: Design considerations, synthesis, characterization and applications*. Journal of Industrial and Engineering Chemistry, 2019. **79**: p. 383-408.

69.   Wu, X., et al., *Inverse-opal structured TiO2 regulating electrodeposition behavior to enable stable lithium metal electrodes*. Green Energy & Environment, 2022.

70.   Yang, Y. and M.R. Hoffmann, *Synthesis and Stabilization of Blue-Black TiO2 Nanotube Arrays for Electrochemical Oxidant Generation and Wastewater Treatment*. Environmental Science & Technology, 2016. **50**(21): p. 11888-11894.

71.   Yang, Y., et al., *Cobalt-Doped Black TiO2 Nanotube Array as a Stable Anode for Oxygen Evolution and Electrochemical Wastewater Treatment*. ACS Catal, 2018. **8**(5): p. 4278-4287.

72.   Ko, J.S., et al., *Novel niobium-doped titanium oxide towards electrochemical destruction of forever chemicals*. Scientific Reports, 2021. **11**(1): p. 18020.

73.   Kesselman, J.M., et al., *Electrochemical production of hydroxyl radical at polycrystalline Nb-doped TiO2 electrodes and estimation of the partitioning between hydroxyl radical and direct hole oxidation pathways*. The Journal of Physical Chemistry B, 1997. **101**(14): p. 2637-2643.

74.   Zhang, C., et al., *Design and in-situ construct BiOI/Bi/TiO2 photocatalysts with metal-mediated heterostructures employing oxygen vacancies in TiO2 nanosheets.* Green Energy & Environment, 2022. **7**(4): p. 680-690.

75.   Nevárez-Martínez, M.C., et al., *Self-Organized TiO2–MnO2 Nanotube Arrays for Efficient Photocatalytic Degradation of Toluene.* Molecules, 2017. **22**(4): p. 564.

76.   Ma, Q., et al., *Fabrication of MnO2/TiO2 nano-tube arrays photoelectrode and its enhanced visible light photoelectrocatalytic performance and mechanism.* Separation and Purification Technology, 2017. **189**: p. 193-203.

77.   Wang, G., et al., *Construction of TiO2–MnO2 0D–2D nanostructured heterojunction for enhanced photocatalytic hydrogen production.* Dalton Transactions, 2021. **50**(25): p. 8711-8717.

78.   Li, S., et al., *Influence of MnO2 on the photocatalytic activity of P-25 TiO2 in the degradation of methyl orange.* Science in China Series B: Chemistry, 2008. **51**(2): p. 179-185.

79.   Chiam, S.-L., S.-Y. Pung, and F.-Y. Yeoh, *Recent developments in MnO2-based photocatalysts for organic dye removal: a review.* Environmental Science and Pollution Research, 2020. **27**(6): p. 5759-5778.

80.   Park, E., et al., *Synthesis and enhanced photocatalytic activity of Mn/TiO2 mesoporous materials using the impregnation method through CVC process.* Journal of Porous Materials, 2012. **19**(5): p. 877-881.

81.   Xu, X., et al., *Effect of multi-walled carbon nanotubes addition on MnOx/Ti electrode prepared by spraying–calcination method for electro-catalytic oxidation of Acid Red B.* Journal of Materials Science, 2019. **54**(19): p. 12509-12521.

82.   Massa, A., et al., *Electro-oxidation of phenol over electrodeposited MnOx nanostructures and the role of a TiO2 nanotubes interlayer.* Applied Catalysis B: Environmental, 2017. **203**: p. 270-281.

83.   Chen, M., et al., *Development of a highly efficient electrochemical flow-through anode based on inner in-site enhanced TiO2-nanotubes array.* Environment International, 2020. **140**: p. 105813.

84.   Klein, G.W., et al., *Reaction of hydroxyl radicals with benzoic acid. Isomer distribution in the radical intermediates.* The Journal of Physical Chemistry, 1975. **79**(17): p. 1767-1774.

85.   Cerrato, J.M., et al., *Application of XPS and Solution Chemistry Analyses to Investigate Soluble Manganese Removal by MnOx(s)-Coated Media.* Environmental Science & Technology, 2011. **45**(23): p. 10068-10074.

86.   Stranick, M.A., *Mn2O3 by XPS.* Surface Science Spectra, 1999. **6**(1): p. 39-46.

87.   Nesbitt, H. and D. Banerjee, *Interpretation of XPS Mn (2p) spectra of Mn oxyhydroxides and constraints on the mechanism of MnO2 precipitation.* American Mineralogist, 1998. **83**(3-4): p. 305-315.

88.   Jildeh, Z.B., et al., *Thermocatalytic Behavior of Manganese (IV) Oxide as Nanoporous Material on the Dissociation of a Gas Mixture Containing Hydrogen Peroxide.* Nanomaterials (Basel), 2018. **8**(4).

89.   Allen J. Bard, L.R.F., *Electrochemical Methods: Fundamentals and Applications, New York: Wiley, 2001, 2nd ed.* Russian Journal of Electrochemistry, 2002. **38**(12): p. 1364-1365.

90.   Wang, Y., et al., *Highly Promoted Carrier Mobility and Intrinsic Stability by Rolling Up Monolayer Black Phosphorus into Nanoscrolls.* The Journal of Physical Chemistry Letters, 2018. **9**(23): p. 6847-6852.

91.   Sun, B., et al., *Controlled fabrication of Sn/TiO2 nanorods for photoelectrochemical water splitting.* Nanoscale Research Letters, 2013. **8**(1): p. 462.

92.   Jana, S.K., et al., *Structural and electrochemical analysis of a novel co-electrodeposited Mn2O3–Au nanocomposite thin film.* Dalton Transactions, 2015. **44**(19): p. 9158-9169.

93.   Crittenden, J.C., et al., *MWH's water treatment: principles and design.* 2012: John Wiley & Sons.

94.   Deng, D., et al., *Overlimiting Current and Shock Electrodialysis in Porous Media.* Langmuir, 2013. **29**(52): p. 16167-16177 %U https://doi.org/10.1021/la4040547.

95.   Kim, J.-H., et al., *Electrical Double Layer Mechanism Analysis of PEM Water Electrolysis for Frequency Limitation of Pulsed Currents.* Energies, 2021. **14**(22): p. 7822.

96.   Burton, N.A., et al., *Increasing the efficiency of hydrogen production from solar powered water electrolysis.* Renewable and Sustainable Energy Reviews, 2021. **135**: p. 110255.

97.   Lin, M.-Y. and L.-W. Hourng, *Effects of magnetic field and pulse potential on hydrogen production via water electrolysis.* International Journal of Energy Research, 2014. **38**(1): p. 106-116.

98.   Dobó, Z. and Á.B. Palotás, *Impact of the current fluctuation on the efficiency of alkaline water electrolysis.* International Journal of Hydrogen Energy, 2017. **42**(9): p. 5649-5656.

99. Marks, R.G.H., et al., *Electrochemical degradation of perfluorooctanoic acid in aqueous solution by boron-doped diamond electrodes under pulsed voltage conditions.* Journal of Electroanalytical Chemistry, 2021. **895**: p. 115415.

100. Ji, H., et al., *Capacitance of carbon-based electrical double-layer capacitors.* Nature Communications, 2014. **5**(1): p. 3317.

101. Shervedani, R.K., A.H. Alinoori, and A.R. Madram, *Electrocatalytic activities of nickel-phosphorous composite coating reinforced with codeposited graphite carbon for hydrogen evolution reaction in alkaline solution.* J New Mater Electrochem Syst, 2008. **11**(4): p. 259-265.

102. Lehmler, H.-J., *Synthesis of environmentally relevant fluorinated surfactants—a review.* Chemosphere, 2005. **58**(11): p. 1471-1496.

103. Xu, J., et al., *Bioaccumulation and trophic transfer of perfluorinated compounds in a eutrophic freshwater food web.* 2014. **184**: p. 254-261.

104. Song, Z., et al., *Reductive defluorination of perfluorooctanoic acid by hydrated electrons in a sulfite-mediated UV photochemical system.* J Hazard Mater, 2013. **262**: p. 332-8.

105. Sun, M., et al., *Distribution of perfluorinated compounds in drinking water treatment plant and reductive degradation by UV/SO3(2-) process.* Environ Sci Pollut Res Int, 2018. **25**(8): p. 7443-7453.

106. Martin, J.W., et al., *Perfluoroalkyl contaminants in a food web from Lake Ontario.* Environ Sci Technol, 2004. **38**(20): p. 5379-85.

107. Guo, J., et al., *Alternative Fluoropolymers to Avoid the Challenges Associated with Perfluorooctanoic Acid.* Industrial & Engineering Chemistry Research, 2008. **47**(3): p. 502-508.

108. Yin, P., et al., *Activated Persulfate Oxidation of Perfluorooctanoic Acid (PFOA) in Groundwater under Acidic Conditions.* International Journal of Environmental Research and Public Health, 2016. **13**(6): p. 602.

109. Liang, S., et al., *Electrochemical oxidation of PFOA and PFOS in concentrated waste streams.* Remediation Journal, 2018. **28**(2): p. 127-134.

110. Trojanowicz, M., et al., *Advanced Oxidation/Reduction Processes treatment for aqueous perfluorooctanoate (PFOA) and perfluorooctanesulfonate (PFOS) – A review of recent advances.* Chemical Engineering Journal, 2018. **336**: p. 170-199.

111. Chiavola, A., et al., *PFOA and PFOS Removal Processes in Activated Sludge Reactor at Laboratory Scale*, in *Frontiers in Water-Energy-Nexus—Nature-Based Solutions, Advanced Technologies and Best Practices for Environmental Sustainability*. 2020, Springer: Cham. p. 375-377.

112. Xiao, F., M.F. Simcik, and J.S. Gulliver, *Mechanisms for removal of perfluorooctane sulfonate (PFOS) and perfluorooctanoate (PFOA) from drinking water by conventional and enhanced coagulation.* Water Research, 2013. **47**(1): p. 49-56.

113. Lin, H., et al., *Efficient Sorption and Removal of Perfluoroalkyl Acids (PFAAs) from Aqueous Solution by Metal Hydroxides Generated in Situ by Electrocoagulation.* Environmental Science & Technology, 2015. **49**(17): p. 10562-10569.

114. Bartell, S.M., et al., *Rate of Decline in Serum PFOA Concentrations after Granular Activated Carbon Filtration at Two Public Water Systems in Ohio and West Virginia.* Environmental Health Perspectives, 2010. **118**(2): p. 222-228.

115. Bao, Y., et al., *Removal of perfluorooctane sulfonate (PFOS) and perfluorooctanoate (PFOA) from water by coagulation: Mechanisms and influencing factors.* Journal of Colloid and Interface Science, 2014. **434**: p. 59-64.

116. Lath, S., et al., *Sorption of PFOA onto different laboratory materials: Filter membranes and centrifuge tubes.* Chemosphere, 2019. **222**: p. 671-678.

117. Lee, Y.-C., et al., *Efficient decomposition of perfluorocarboxylic acids in aqueous solution using microwave-induced persulfate.* Water Research, 2009. **43**(11): p. 2811-2816.

118. Watanabe, N., et al., *Thermal mineralization behavior of PFOA, PFHxA, and PFOS during reactivation of granular activated carbon (GAC) in nitrogen atmosphere.* Environmental Science and Pollution Research, 2018. **25**(8): p. 7200-7205.

119. Lin, J.-C., C.-Y. Hu, and S.-L. Lo, *Effect of surfactants on the degradation of perfluorooctanoic acid (PFOA) by ultrasonic (US) treatment.* Ultrasonics Sonochemistry, 2016. **28**: p. 130-135.

120. Prevedouros, K., et al., *Sources, Fate and Transport of Perfluorocarboxylates.* Environmental Science & Technology, 2006. **40**(1): p. 32-44.

121. Guideline, P.-B.T., *OECD guideline for the testing of chemicals.* The Hershberger, 2001. **601**: p. 858.

122. Zhou, Y., et al., *Special Effect of Ionic Liquids on the Extraction of Flavonoid Glycosides from Chrysanthemum morifolium Ramat by Microwave Assistance.* Molecules, 2015. **20**(5): p. 7683-99.

123. Ji, S., et al., *Ionic liquids-ultrasound based efficient extraction of flavonoid glycosides and triterpenoid saponins from licorice.* RSC Advances, 2018. **8**(25): p. 13989-13996.

124. Germani, R., et al., *Mercury extraction by ionic liquids: temperature and alkyl chain length effect.* Tetrahedron Letters, 2007. **48**(10): p. 1767-1769.

125. Yao, Y., et al., *Remedial options for PFC contaminated sites: A review.* Proceedings of the 36th AMOP Technical Seminar on Environmental Contamination and Response, 2013: p. 654-672.

126. Zhang, D.Q., W.L. Zhang, and Y.N. Liang, *Adsorption of perfluoroalkyl and polyfluoroalkyl substances (PFASs) from aqueous solution - A review.* Sci Total Environ, 2019. **694**: p. 133606.

127. Kishimoto, N. and M. Kobayashi, *Effects of three additives on the removal of perfluorooctane sulfonate (PFOS) by coagulation using ferric chloride or aluminum sulfate.* Water Science and Technology, 2016. **73**(12): p. 2971-2977.

128. Kishimoto, N. and H. Kimura, *Fouling behaviour of a reverse osmosis membrane by three types of surfactants.* Journal of Water Reuse and Desalination, 2012. **2**(1): p. 40-46.

129. Sun, X., H. Luo, and S. Dai, *Ionic liquids-based extraction: a promising strategy for the advanced nuclear fuel cycle.* Chem Rev, 2012. **112**(4): p. 2100-28.

130. Li, Z.Y., et al., *Anionic structural effect in liquid-liquid separation of phenol from model oil by choline carboxylate ionic liquids.* Green Energy & Environment, 2019. **4**(2): p. 131-138.

131. Zhang, S.J., et al., *A new era of precise liquid regulation: Quasi-liquid.* Green Energy & Environment, 2017. **2**(4): p. 329-330.

132. Nakashima, K., et al., *Feasibility of Ionic Liquids as Alternative Separation Media for Industrial Solvent Extraction Processes.* Industrial & Engineering Chemistry Research, 2005. **44**(12): p. 4368-4372.

133. Huddleston, J.G., et al., *Characterization and comparison of hydrophilic and hydrophobic room temperature ionic liquids incorporating the imidazolium cation.* Green Chemistry, 2001. **3**(4): p. 156-164.

134. Omorodion, H., et al., *A rationally designed perfluorinated host for the extraction of PFOA from water utilising non-covalent interactions.* New Journal of Chemistry, 2018. **42**(10): p. 7956-7968.

135. Li, Z., et al., *Enhancing Metal Separations Using Hydrophilic Ionic Liquids and Analogues as Complexing Agents in the More Polar Phase of Liquid–Liquid Extraction Systems.* Industrial & Engineering Chemistry Research, 2019. **58**(34): p. 15628-15636.

136. Hidayah, N.N. and S.Z. Abidin, *Extraction of light, medium and heavy rare-earth elements using synergist extractants developed from ionic liquid and conventional extractants.* Comptes Rendus Chimie, 2019. **22**(11): p. 728-744.

137. Bai, Y.G., et al., *Recovery of methacrylic acid from dilute aqueous solutions by ionic liquids though hydrogen bonding interaction.* Separation and Purification Technology, 2017. **184**: p. 354-364.

138. Frisch, M., et al., *Gaussian 09 (Revision D.01).* 2009.

139. Plimpton, S., *Fast Parallel Algorithms for Short-Range Molecular-Dynamics.* Journal of Computational Physics, 1995. **117**(1): p. 1-19.

140. Wu, X., et al., *Molecular dynamics simulation of room-temperature ionic liquid mixture of [bmim][BF4] and acetonitrile by a refined force field.* Phys Chem Chem Phys, 2005. **7**(14): p. 2771-9.

141. Hockney, R.W. and J.W. Eastwood, *Computer simulation using particles.* 1988: Taylor & Francis, Inc. 564.

142. Bai, J., J.S. Francisco, and X.C. Zeng, *Two-dimensional dry ices with rich polymorphic and polyamorphic phase behavior.* Proc Natl Acad Sci U S A, 2018. **115**(41): p. 10263-10268.

143. Berendsen, H.J.C., et al., *Molecular-Dynamics with Coupling to an External Bath.* Journal of Chemical Physics, 1984. **81**(8): p. 3684-3690.

144. Chowhan, Z.T., *pH-solubility profiles or organic carboxylic acids and their salts.* J Pharm Sci, 1978. **67**(9): p. 1257-60.

145. Burns, D.C., et al., *Experimental pKa determination for perfluorooctanoic acid (PFOA) and the potential impact of pKa concentration dependence on laboratory-measured partitioning phenomena and environmental modeling.* Environ Sci Technol, 2008. **42**(24): p. 9283-8.

146. Goss, K.U., *The pKa values of PFOA and other highly fluorinated carboxylic acids.* Environ Sci Technol, 2008. **42**(2): p. 456-8.

147. Wang, F., C. Liu, and K. Shih, *Adsorption behavior of perfluorooctanesulfonate (PFOS) and perfluorooctanoate (PFOA) on boehmite.* Chemosphere, 2012. **89**(8): p. 1009-14.

148. Jeon, J., et al., *Effects of salinity and organic matter on the partitioning of perfluoroalkyl acid (PFAs) to clay particles.* J Environ Monit, 2011. **13**(6): p. 1803-10.

149. Gao, X.D. and J. Chorover, *Adsorption of perfluorooctanoic acid and perfluorooctanesulfonic acid to iron oxide surfaces as studied by flow-through ATR-FTIR spectroscopy.* Environmental Chemistry, 2012. **9**(2): p. 148-157.

150. Wang, T., et al., *Perspectives on the Inclusion of Perfluorooctane Sulfonate into the Stockholm Convention on Persistent Organic Pollutants.* Environmental Science & Technology, 2009. **43**(14): p. 5171-5175.

151. Zhou, Z., et al., *Occurrence and transport of perfluoroalkyl acids (PFAAs), including short-chain PFAAs in Tangxun Lake, China.* Environmental Science and Technology, 2013. **47**(16): p. 9249-9257.

152. Chen, W., et al., *Sorption of perfluorooctane sulfonate and perfluorooctanoate on polyacrylonitrile fiber-derived activated carbon fibers: in comparison with activated carbon.* RSC Advances, 2017. **7**(2): p. 927-938.

153. Chiavola, A., et al., *Experimental investigation on the perfluorooctanoic and perfluorooctane sulfonic acids fate and behaviour in the activated sludge reactor.* Process Safety and Environmental Protection, 2020. **134**: p. 406-415.

154. Senevirathna, S.T.M.L.D., et al., *Adsorption of perfluorooctane sulfonate (n-PFOS) onto non ion-exchange polymers and granular activated carbon: Batch and column test.* Desalination, 2010. **260**(1): p. 29-33.

155. Bao, Y., et al., *Degradation of PFOA Substitute: GenX (HFPO–DA Ammonium Salt): Oxidation with UV/Persulfate or Reduction with UV/Sulfite?* Environmental Science & Technology, 2018. **52**(20): p. 11728-11734.

156. Niu, J., et al., *Electrochemical oxidation of perfluorinated compounds in water.* Chemosphere, 2016. **146**: p. 526-538.

157. Zhang, K., et al., *Extraction of PFOA from dilute wastewater using ionic liquids that are dissolved in N-octanol.* Journal of Hazardous Materials, 2021. **404**: p. 124091.

158. Zhang, S., *COIL-8: Ionic liquids for tomorrow.* Green Energy & Environment, 2020. **5**(2): p. 121.

159. Li, B., et al., *High CO2 absorption capacity of metal-based ionic liquids: A molecular dynamics study.* Green Energy & Environment, 2021. **6**(2): p. 253-260.

160. Yokozeki, A. and M.B. Shiflett, *Water Solubility in Ionic Liquids and Application to Absorption Cycles.* Industrial & Engineering Chemistry Research, 2010. **49**(19): p. 9496-9503.

161. Li, Z., et al., *Anionic structural effect in liquid–liquid separation of phenol from model oil by choline carboxylate ionic liquids.* Green Energy & Environment, 2019. **4**(2): p. 131-138.

162. Chen, Z., et al., *Separation of n-heptane and tert-butanol by ionic liquids based on COSMO-SAC model.* Green Energy & Environment, 2021. **6**(3): p. 380-391.

163. E. Skoronski, M.F., F.J. Malaret, J.P. Hallett, *Use of phosphonium ionic liquids for highly efficient extraction of phenolic compounds from water.* Separation and Purification Technology, 2020. **248**: p. 117069.

164. Costanza, J., et al., *Accumulation of PFOA and PFOS at the Air–Water Interface.* Environmental Science & Technology Letters, 2019. **6**(8): p. 487-491.

165. Badruddoza, A.Z.M., B. Bhattarai, and R.P.S. Suri, *Environmentally Friendly β-Cyclodextrin–Ionic Liquid Polyurethane-Modified Magnetic Sorbent for the Removal of PFOA, PFOS, and Cr(VI) from Water.* ACS Sustainable Chemistry & Engineering, 2017. **5**(10): p. 9223-9232.

166. Pye, C.C., et al., *An implementation of the conductor-like screening model of solvation within the Amsterdam density functional package - Part II. COSMO for real solvents(1).* Canadian Journal of Chemistry-Revue Canadienne De Chimie, 2009. **87**(7): p. 790-797.

167. J.N. Louwen, C.C.P., E. van Lenthe, N.D. Austin, E.S. McGarrity, R. Xiong, S.I. Sandler, R.I. Burnett, *AMS 2020 COSMO-RS, SCM,Theoretical Chemistry.*

168. Xiong, R.C., S.I. Sandler, and R.I. Burnett, *An Improvement to COSMO-SAC for Predicting Thermodynamic Properties.* Industrial & Engineering Chemistry Research, 2014. **53**(19): p. 8265-8278.

169. Austin, N.D., et al., *COSMO-based computer-aided molecular/mixture design: A focus on reaction solvents.* Aiche Journal, 2018. **64**(1): p. 104-122.

170. Song, M., et al., *The preparation and performance of lignin-based activated carbon fiber adsorbents for treating gaseous streams.* Frontiers of Chemical Science and Engineering, 2017. **11**(3): p. 328-337.

171. Dai, C., et al., *COSMO-based models.* Green Energy & Environment, 2021. **6**(3): p. 309-310.

172. F. Olea, G.M., C. Araya-Lopez, R. Cabezas, E. Villarroel, E. Quijada-Maldonado, J. Romero, *Separation of vanillin by perstraction using hydrophobic ionic liquids as extractant phase: Analysis of mass transfer and screening of ILs via COSMO-RS.* Separation and Purification Technology, 2021. **274**: p. 119008.

173. P. Arenas, I.S., B. Coto, *Combination of molecular dynamics simulation, COSMO-RS, and experimental study to understand extraction of naphthenic acid.* Separation and Purification Technology, 2022. **280**: p. 119810.

174. B. Coto, I.S., M. Jose Tenorio, S. Nieto, N. Alvarez, J. Luis Pena, *Oil acidity reduction by extraction with imidazolium ionic liquids: Experimental, COSMO*

description and reutilization study. Separation and Purification Technology, 2021. **254**: p. 117529.

175. D. Zhao, C.L., Y. Wang, H. Zhang, *Ionic liquids design for efficient separation of anthracene and carbazole.* Separation and Purification Technology, 2022. **281**: p. 119892.

176. Z. Wu, S.S., G. Zhan, F. Chang, Y. Bai, X. Zhang, J.C.S. Wu, S. Zeng, *Ionic liquid screening for dichloromethane absorption by multi-scale simulations.* Separation and Purification Technology, 2021. **275**: p. 119187.

177. Brouwer, T. and B. Schuur, *Model Performances Evaluated for Infinite Dilution Activity Coefficients Prediction at 298.15 K.* Industrial & Engineering Chemistry Research, 2019. **58**(20): p. 8903-8914.

178. Y. Liu, Z.D., Z. Zhang, S. Zeng, F. Li, X. Zhang, Y. Nie, L. Zhang, S. Zhang, X. Ji, *Ionic liquids/deep eutectic solvents for CO2 capture: Reviewing and evaluating.* Green Energy & Environment, 2021. **6**: p. 314-328.

179. Mullins, E., et al., *Sigma-Profile Database for Using COSMO-Based Thermodynamic Methods.* Industrial & Engineering Chemistry Research, 2006. **45**(12): p. 4389-4415.

180. Klamt, A., F. Eckert, and W. Arlt, *COSMO-RS: an alternative to simulation for calculating thermodynamic properties of liquid mixtures.* Annu Rev Chem Biomol Eng, 2010. **1**: p. 101-22.

181. Droge, S.T.J., *Membrane–Water Partition Coefficients to Aid Risk Assessment of Perfluoroalkyl Anions and Alkyl Sulfates.* Environmental Science & Technology, 2019. **53**(2): p. 760-770.

182. Goss, K.-U., *The pKa Values of PFOA and Other Highly Fluorinated Carboxylic Acids.* Environmental Science & Technology, 2008. **42**(2): p. 456-458.

183. Wang, Z., et al., *Using COSMOtherm to predict physicochemical properties of poly- and perfluorinated alkyl substances (PFASs).* Environmental Chemistry, 2011. **8**(4): p. 389-398.

184. Schwarzenbach, R.P., P.M. Gschwend, and D.M. Imboden, *Environmental organic chemistry.* 2016: John Wiley & Sons.

185. Liu, Y., et al., *Screening Deep Eutectic Solvents for CO2 Capture With COSMO-RS.* Frontiers in Chemistry, 2020. **8**: p. 82.

186. Eckert, F. and A. Klamt, *Fast solvent screening via quantum chemistry: COSMO-RS approach.* Aiche Journal, 2002. **48**(2): p. 369-385.

187. Kurnia, K.A., et al., *Mutual solubilities between water and non-aromatic sulfonium-, ammonium- and phosphonium-hydrophobic ionic liquids.* Phys Chem Chem Phys, 2015. **17**(6): p. 4569-77.

188. Rezaei Motlagh, S., et al., *Prediction of Potential Ionic Liquids (ILs) for the Solid-Liquid Extraction of Docosahexaenoic Acid (DHA) from Microalgae Using COSMO-RS Screening Model.* Biomolecules, 2020. **10**(8).

189. Rezaei Motlagh, S., et al., *Screening of Suitable Ionic Liquids as Green Solvents for Extraction of Eicosapentaenoic Acid (EPA) from Microalgae Biomass Using COSMO-RS Model.* Molecules, 2019. **24**(4): p. 713.

190. Khan, I., et al., *Probing the Interactions between Ionic Liquids and Water: Experimental and Quantum Chemical Approach.* The Journal of Physical Chemistry B, 2014. **118**(7): p. 1848-1860.

191. Henke, A.H., et al., *Enhancing Electrochemical Efficiency of Hydroxyl Radical Formation on Diamond Electrodes by Functionalization with Hydrophobic Monolayers.* Langmuir, 2019. **35**(6): p. 2153-2163.